CHALMERS

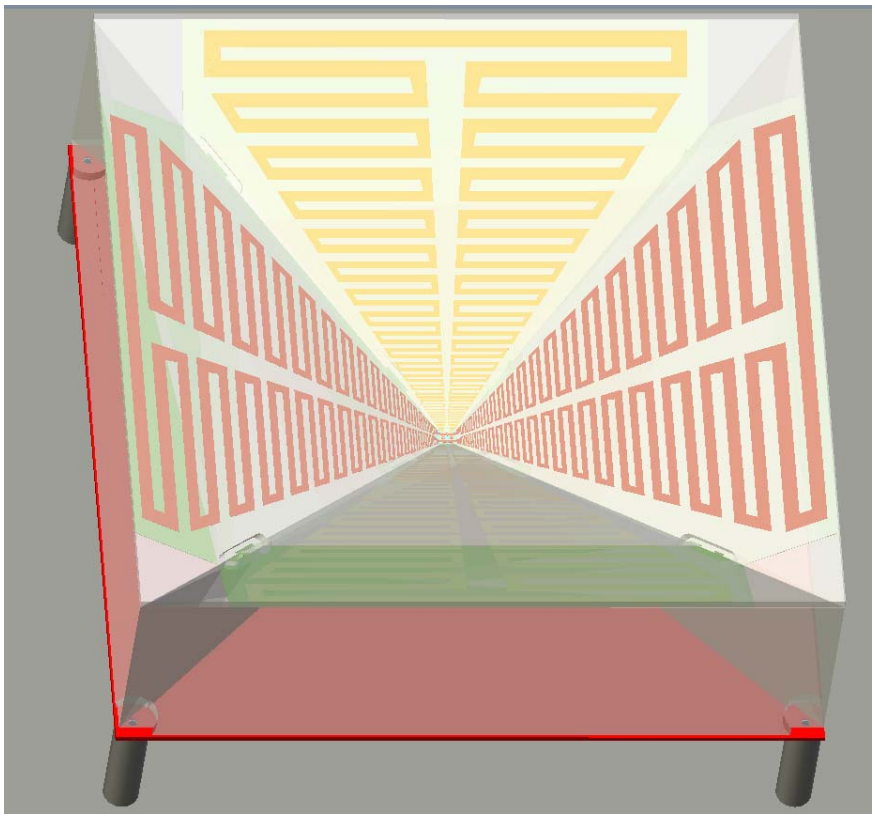

Study of System Noise Temperature from 50 MHz to 15 GHz with Application to ELEVEN Antenna

Chen Xiaoming

Antenna Group
Department of Signals and Systems
Chalmers University of Technology
Gothenburg, Sweden 2007

Study of System Noise Temperature from 50 MHz to 15 GHz with Application to ELEVEN Antenna

By Chen Xiaoming

Master Thesis at Chalmers University of Technology, Sweden

Supervisor: Dr. Jian Yang

Prof. Per-Simon Kildal and Prof. Jan Carlsson

Examiner: Prof. Per-Simon Kildal

Antenna Group
Department of Signals and Systems
Chalmers University of Technology

Gothenburg, Sweden, December 2007

Abstract

The ELEVEN antenna developed at Antenna group, Chalmers is an ultra wide band feed for reflector antennas covering over decade bandwidth. An ultra wide band LNA Chalmers is designed at MC2, Chalmers, to integrate with the ELEVEN antenna to achieve flat gain around 30 dB over the whole bandwidth and minimum system noise temperature. This thesis estimates the system noise temperature theoretically. In addition, this thesis also tries to estimate the system noise temperature of a transceiver in wireless communication environments. A study of mobile antennas in wireless communications is presented as well. Due to the large size of the ELEVEN antenna, its center puck is neglected during computer aided design. This thesis also models the center puck in detail trying to minimize return loss of the ELEVEN antenna. In the end, a new method to efficiently simulate the return losses of ELEVEN antenna is presented.

Acknowledgments

First I want to express my deepest gratitude to Prof. Per-Simon Kildal, my supervisor and examiner. I feel very lucky and happy to work under his guidance. I am impressed by his knowledge in various antenna fields, and his patience with us Master students. In a word, it is a pleasure of mine to work in his group.

I also want to thank Dr. Jian Yang, my main supervisor, who is always willing to offer help to me. I learnt a lot from him during my Master thesis. I also owe thanks to Prof. Jan Carlsson, for his financial support from SP, and his invitations to seminar about MIMO.

My special thanks also go to Prof. Germán Cortés-Medellín at Cornell University. Without his help, I cannot build the brightness noise temperature model. I also need to thank Niklas Wadefalk from MC2 for his work on the LNA and insight into the center puck model. Thanks also go to Yogesh B. Karandikar and Daniel Nyberg, PhD students at Chalmers, and Dr. Ulf, Carlberg, for their help in my daily work at antenna group.

Finally, I am grateful for my parents' love and support. Without their support, I would not finish my study at Chalmers.

Preface

This report is a Master thesis at Chalmers University of Technology. The work was done from June to December 2007 under the supervision of Dr. Jian Yang and Prof. Per-Simon Kildal at antenna group, Chalmers. Prof. Kildal is also the examiner.

As a Master student majoring in microwave, the project of co-design of antenna and LNA was very interesting to me. During my thesis, I had the chance to take one PhD course on EM field theory, which gives me more insight into EM problems in real world. Besides designing the feeding part (center puck) of the ELEVEN antenna and system noise analysis, I also had the chance of studying about small antennas in wireless communications, for which I also have lots of fun.

Content

1. Introduction

Ultra Wide Band (UWB) technologies are of increasing interest in not only wireless communications, but also Satellite Communications (SatCom) and radio astronomy, i.e. Square Kilometer Array (SKA) and Very Long Baseline Interferometry (VLBI). The frequency specifications of SKA, for example, call for antennas operating from 100 MHz to 25 GHz, with an upper goal of 35 GHz [1]. Lots of proposals have been made to meet the UWB requirement. One method of achieving UWB feed is log-periodic antennas.

1.1 Log-periodic Antennas

Log-periodic antennas are basically an array of similar elements spaced in a certain fashion in order to work at different frequencies. A log periodic antenna is characterized by its scaling factor τ , which determines the antenna's operating frequencies, according to

$$f_{n+1} = \tau f_n \qquad n = 1, 2, 3, \ldots \tag{1.1}$$

where n is the number of element. After rearranging and taking logarithm on both sides,

$$\ln \frac{f_{n+1}}{f_1} = n \ln \tau \tag{1.2}$$

That is why this kind of antenna is called log-periodic antenna.

Ordinary dipole arrays have for a long time been used as reflector feed. It is actually quite often to design a dipole-array that provides a good radiation pattern and real input impedance at an appropriate level. The problem is that they usually only work for a narrow frequency band. For UWB application, constant properties over a large bandwidth are required. And log-periodic antennas are one effective solution to this problem. Two of the applicable UWB feeds are ATA feed and ELEVEN feed (or Chalmers feed).

1.1.1 ATA Feed

In Allen Telescope Array (ATA), similar to SKA yet in smaller scale, ATA feed (see Fig.1.1) is used. ATA feed has the advantages of wide bandwidth, good input match, low cross-polarization, etc. However, it is bulky, difficult to connect with LNA, with

high side lobes, and most of all, its center phase is frequency dependent, which results in low aperture efficiency.

Figure 1.1: Photographs of two ATA feeds.

1.1.2 ELEVEN Feed

An alternative to ATA feed is ELEVEN feed (see Fig.1.2), developed at antenna group, Chalmers. The idea is to use the fact that the phase center of a dipole above a ground plane is locked to that ground plane. It is also a known fact that two adjacent dipoles above a ground plane generate a nice bore-sight radiation pattern.

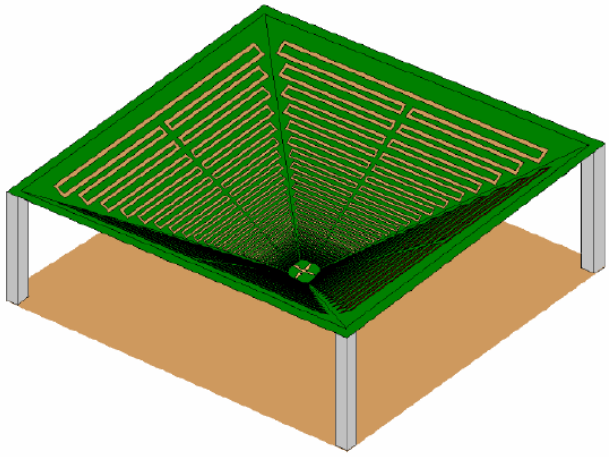

Figure 1.2: ELEVEN antenna drawing.

Compared with ATA feed, ELEVEN feed has the advantages of smaller volume, frequency independent phase center. The ELEVEN antenna [2]-[7] developed at antenna group can work from 1 GHz to 13 GHz. And it is believed that it can also work up to 18 GHz through further development.

1.2 LNA

The low noise amplifier (LNA) design is one of the biggest challenges in a UWB system. The UWB LNA [8] [9] should have lowest noise figure possible to reduce the system noise temperature, and provide sufficient flat gain to suppress noise temperature contributed from the following stages and prevent intermediations.

A standard MMIC LNA design procedure are: first, Get equivalent circuit model of transistor by manufacturer's data or by S parameter measurements followed by fitting or solving for circuit element values; second, Obtain noise parameters of transistor by manufacturer's data, by measurement, or by equivalent circuit plus physics; third, design of the input circuit to transform the generator impedance to optimal source impedance; last, design following stages for maximum gain and stability especially at lower frequencies. Terminate the transistor with resistive loads at lower frequencies.

The LNA designed by Niklas at MC2 is shown in Fig.1.3.

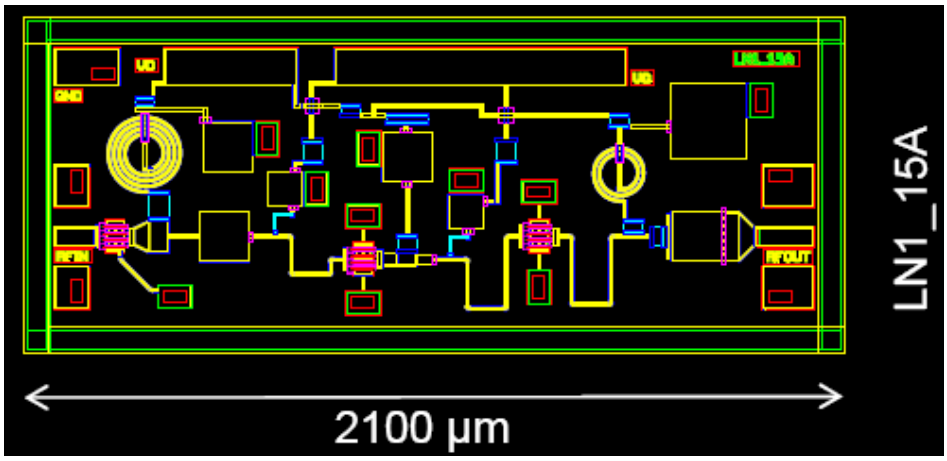

Figure 1.3: Single-ended MMIC LNA (Courtesy of Niklas Wadefalk).

1.3 Antenna/LNA Co-design

The most promising strategies for hardware technology breakthrough nowadays are, perhaps, co-design of design of two or more components. For example, co-design of antennas and front-end transceivers, or antenna integrated with microwave circuits [10]-[12]. The antenna and front-end electronics co-design can be divided into three classes: first, antenna-receiver (LNA) co-design for low noise application; second, antenna-transmitter (PA) co-design for high efficiency power application; third, integrated antennas on chips when operating frequencies are above 60 GHz.

However, antennas and transceiver front-end electronics are usually developed by different experts at different departments. Most electronic engineers use circuit theory models to analyze passive and active circuits. Such models are straightforward to implement, and do not require solid electromagnetic background. Yet they fail to analyze radiation phenomena when antennas are involved. Antenna engineers, on the other hand, pay lots of efforts to optimize radiation pattern and efficiency of the antennas. When referring to antenna input reflection (or return loss), they usually assume common constant characteristic impedance (50 or 75 ohms). But the optimal source impedance for a LNA is seldom 50 or 75 ohms, especially for UWB applications. In this way, a matching network may need to be made by the antenna designer to transform the antenna impedance to a certain value; and the microwave electronic designer may have to use another matching network to transform the source impedance to another value. This makes the whole receiver bulky, more expensive, and most of all, imperfect in terms of noise figure or power efficiency.

Since the foremost component of a receiver is LNA, the antenna and receiver co-design will focus on integrated antenna with LNA. To the LNA in this case, the antenna input impedance is the source impedance that needs to be optimized to achieve a minimum noise figure and maximum transducer gain [13]-[15].

By means of antenna-LNA co-design, antenna and LNA can be integrated seamlessly, and the cables between antenna and LNA can be removed, which means that the antenna input impedance can be made more favorably for a optimal LNA performance, as long as the antenna characteristics do not degrade. This will simplify the system design; no expensive contact is needed between the antenna and the circuits. System noise temperature can be further reduced. In case that a trade-off has to be made, G/T (where G is the antenna gain, and T is the system noise temperature) can be deployed as a figure of merit to tweak the parameters of either the antenna or the LNA, so that the receiver front-end has the highest G/T.

This thesis will focus on the system noise temperature of the ELEVEN antenna integrated with LNA from a system overview. A noise temperature estimation of a transceiver in wireless communication environments follows as supplement. A study of mobile antennas in wireless communications will also be mentioned. Finally, a model of the center puck of the ELEVEN antenna will be presented; together with ELEVEN antenna petals, the return losses of ELEVEN antenna can be simulated efficiently.

2. Study of Brightness Temperature

In order to calculate system noise temperature of a radio telescope, a model of brightness temperature has to be built. That is the main purpose of this chapter.

2.1 Definitions of Brightness Temperature

The fundamental quantity that a radio telescope measures is radiation power, which is related to the specific intensity I_v, defined as the radiation power per unit area, per unit frequency interval at a specified direction. In microwave frequency band, the intensity is usually expressed as brightness temperature, denoted as T_b [16] [17]. However, there are two popular definitions of the brightness temperature in microwave radiometry, which is confusing sometimes. Here, a brief discussion is presented. For a detailed discussion, please refer to Stogryn [18].

One of the definitions is Rayleigh-Jeans equivalent brightness temperature, defined as

$$T_b^{RJE} = \frac{\lambda^2}{2k} I_v \qquad (2.1)$$

where k is Boltzmann's constant, λ is wave-length of light.

The other definition is thermodynamic brightness temperature, defined as

$$T_b^{TRM} = B_v^{-1} I_v \qquad (2.2)$$

where B_v^{-1} is the inverse of the Planck function $B_v(T)$, which is the radiance emitted by a blackbody at physical temperature T and given by

$$B_v(T) = \frac{2hf^3}{c^2} \frac{1}{\exp(hf/kT) - 1} \qquad (2.3)$$

where h is Planck constant, and f is used to denote frequency as a usual practice of the astronomer.

In microwave frequency band, the difference between T_b^{RJE} and T_b^{TRM} is well represented by $\frac{hf}{2k}$, which is negligible. However, at higher frequencies ($f > 300GHz$), their difference becomes significant [19]. In the next section, it will be shown that the difference of these two popular definitions is due to the use of

Rayleigh-Jeans approximation, and that the difference of between T_b^{RJE} and T_b^{TRM} is due to the inaccuracy of T_b^{RJE}, especially at higher frequencies.

2.2 Brightness Temperature and Radiative Transfer

Radiative transfer theory describes the intensity of radiation propagating in a media (atmosphere this case) that absorb, emit and scatter radiation. In the atmosphere, radiation emitted by molecules is in part attenuated by atmospheric absorption. The absorbed energy is reemitted as thermal radiation. Attenuation depends on the distance traveled by the radiation in the atmosphere. The specific intensity received from a given direction in the atmosphere is given by [20]

$$I_v = I_v(s_o)e^{-\tau_v(s_o)} + \int_0^{s_o} k_a(f,s)B_v(T)e^{-\tau_v(s)}ds \qquad (2.4)$$

where $I_v(s_o)$ is the background intensity at a distance s_o, $k_a(v,s)$ is the atmospheric absorption coefficient, and τ_v is opacity or optical depth of the atmosphere, defined by

$$\tau_v(s) = \int_0^s k_a(f,l)dl \qquad (2.5)$$

Note that atmosphere scattering is ignored for the sake of simplification.
At microwave frequencies, the Planck's function given by (2.3) can be simplified by Rayleigh-Jeahs approximation into

$$B_v(T) \approx \frac{2kT}{\lambda^2} \qquad (2.6)$$

Based on the linearity between $B_v(T)$ and physical temperature T, the brightness temperature T_b is defined as

$$T_b = \frac{\lambda^2}{2k} I_v \qquad (2.7)$$

By comparing (2.7) with (2.1), it is easy to understand that Rayleigh-Jeans equivalent brightness temperature is introduced by simplifying thermodynamic brightness temperature via Rayleigh-Jeans approximation. Hence, the definition of thermodynamic brightness temperature is more general.
Substitute (2.7) into (2.4), and after rearrangement, brightness temperature can be expressed as

$$T_b(f) = T_{b0}(f)e^{-\tau_v(s_o)} + \int_0^{s_o} k_a(f,s)T(s)e^{-\tau_v(s)}ds \qquad (2.8)$$

where $T_{b0}(f)$ is the background brightness temperature, which is due to cosmic emission.

Note that the "brightness temperature" in (2.8) does not include noise due ground emission and scattering.

The Rayleigh-Jeans approximation that underlines the clouds absorption algorithm restricts its validity to non-precipitating clouds, whose particulate radii are less than 100 micrometers, scattering is neglected. Therefore, these simplifications limit the validity of brightness temperature less than 100 GHz [19].

2.3 Contributions to Brightness Temperature

There are mainly three factors contribute to the brightness temperature: first, emission from the gases in the atmosphere, namely, atmospheric absorption noise; second, apparent temperature of the background sky seen through the atmosphere, namely cosmic noise; third, emission and scattering from the ground, or ground noise for short.

Often microwave engineers, especially antenna engineers, like to refer noises come from the first two contribution as "sky noise"; while astronomers tend to omit contribution from ground and call "sky noise temperature" as brightness temperature.

Since ground emission and scattering indeed contribute to antenna noise temperature, which is actually our motivation to study the brightness temperature, here brightness temperature is considered as "sky brightness temperature" together with ground noise. Consequently, the "brightness temperature" derived in (2.8) is actually "sky brightness temperature", denoted as $T_b^{sky}(f)$.

Brightness temperature in our case should be

$$T_b(f) = \begin{cases} T_b^{sky}(f), & 0 \le \theta < \pi/2 \\ T_g(f), & \pi/2 \le \theta \le \pi \end{cases} \qquad (2.9)$$

where $T_g(f)$ is noise temperature due to ground emission and scattering and θ is radiometer observation angle with respect to the zenith.

2.3.1 Atmospheric Absorption

It is know that from the theory of blackbody radiation that any body which absorbs energy radiates the same amount of energy that it absorbs. Atmospheric attenuation is caused primarily by the absorption of microwave energy by water vapor and molecular oxygen. Maximum absorption occurs when the frequency coincides with one of the molecular resonance of water or oxygen, thus atmospheric attenuation has

distinct peaks at these frequencies. Generally, at frequencies below 10 GHz the atmosphere has little effect on the strength of a signal. At 22.2 and 183.3 GHz, resonance peaks occurs due to water vapor resonances, while resonance of molecular oxygen cause peaks at 60 and 120GHz [21]. Precipitation such as rain, snow and fog will increase the attenuation, especially at higher frequencies. Asoka [22] offers a procedure for predicting the combined effects rain attenuation, which provides the best average accuracy globally between 10 to 30 GHz.
For simplification, only water vapor and oxygen absorption is considered here, and therefore, the atmospheric absorption coefficient is reduced to

$$k_a(f,s) = k_{H_2O}(f,s) + k_{O_2}(f,s) \qquad (2.10)$$

2.3.1.1 Water Vapor Absorption Coefficient

The absorption coefficient for the water vapor in the atmosphere can be approximated as [20]

$$k_{H_2O}(f) = 2f^2\rho_v(300/T)^{2.5}\sum_{i=1}^{10} A_i e^{-\varepsilon_i^{'}/T} F_{H_2O}(f,v_i) + \Delta k(f) \quad \text{[dB/km]} \qquad (2.11)$$

with $F_{H_2O}(f,v_i) = \dfrac{r_i}{(v_i^2 - f^2)^2 + 4f^2 r_i^2}$

$$r_i = r_{i0}\left(\frac{P}{1013}\right)\left(\frac{300}{T}\right)^{x_i}\left(1 + 0.01a_i\frac{\rho_v T}{P}\right)$$

$$\Delta k(f) = 4.69\times10^{-6}\rho_v\left(\frac{P}{1000}\right)\left(\frac{300}{T}\right)^{2.1} f^2$$

where ρ_v is the water vapor density in the atmosphere, P is the atmospheric pressure.

Values for the first 10 transition line parameters for atmospheric water vapor are shown in Table 2-1.

Table 2-1: Water vapor line absorption transition parameters

i	v_i	$\varepsilon_i^{'}$	A_i	r_{i0}	a_i	x_i
1	22.23515	644	1	2.85	1.75	0.626
2	183.31012	196	41.9	2.68	2.03	0.649
3	323	1850	334.4	2.30	1.95	0.42
4	325.1538	454	115.7	3.03	1.85	0.619
5	380.1968	306	651.8	3.19	1.82	0.63
6	390	2199	127	2.11	2.03	0.33
7	436	1507	191.4	1.5	1.97	0.29
8	438	1070	697.6	1.94	2.01	0.36
9	442	1507	590.2	1.51	2.02	0.332
10	448.0008	412	973.1	2.47	2.19	0.51

2.3.1.2 Oxygen Absorption Coefficient

The oxygen absorption coefficient is [20]

$$k_{O_2}(f) = 1.61\times10^{-2} f^2 (\frac{P}{1000})(\frac{300}{T})^2 F_{O_2}(f, v_i) \quad \text{[dB/km]} \qquad (2.12)$$

where $F_{O_2}(f, v_i) = \frac{0.7 r_b}{f^2 + r_b^2} + \sum_{j=1,3,5...}^{39} \Phi_j [g_{j^+}(f) + g_{j^+}(-f) + g_{j^-}(f) + g_{j^-}(-f)]$

with $\Phi_j = 4.6\times10^{-3} (\frac{300}{T})(2j+1)\exp\{-6.89\times10^{-3}(\frac{300}{T})\, j(j+1)\}$

$$g_{j^\pm}(f) \frac{r_i d_{j^\pm}^2 + P(f - v_{j^\pm}) Y_{j^\pm}}{(f - v_{j^\pm})^2 + r_i^2}$$

$$r_j = 1.18(\frac{P}{1013})(\frac{300}{T})^{0.85}$$

$$r_b = 0.49(\frac{P}{1013})(\frac{300}{T})^{0.89}$$

$$d_{j^+} = [\frac{j(2j+3)}{(j+1)(2j+1)}]^{1/2}$$

$$d_{j^-} = [\frac{(j+1)(2j-1)}{j(2j+1)}]^{1/2}.$$

Values of the first 20 line absorption parameters for atmospheric oxygen are shown in Table 2-2.

Based on water-vapor and oxygen absorption models, atmosphere absorption coefficient at sea level, with water-vapor density of $7.5 g/m^3$ and ambient temperature of 293 K, is calculated and plotted, as shown in Fig.2.1.

Table 2-2: Oxygen line absorption parameters

j	ν_{j^+}	ν_{j^-}	Y_{j^+}	Y_{j^-}
1	56.2648	118.7503	4.51×10^{-4}	-2.14×10^{-3}
3	58.4466	62.4863	4.94×10^{-4}	-3.78×10^{-4}
5	59.592	60.3061	3.52×10^{-4}	-3.92×10^{-4}
7	60.4348	59.1642	1.86×10^{-4}	-2.68×10^{-4}
9	61.1506	58.3239	3.30×10^{-5}	-1.13×10^{-4}
11	61.8002	57.6142	-1.03×10^{-4}	3.44×10^{-5}
13	62.4112	56.9682	-2.23×10^{-4}	1.65×10^{-4}
15	62.998	56.3634	-3.32×10^{-4}	2.84×10^{-4}
17	63.5685	55.7838	-4.32×10^{-4}	3.91×10^{-4}
19	64.1278	55.2214	-5.62×10^{-4}	4.93×10^{-4}
21	64.6789	54.6711	-6.13×10^{-4}	5.84×10^{-4}
23	65.2241	54.13	-6.99×10^{-4}	6.76×10^{-4}
25	65.7647	53.5957	-7.74×10^{-4}	7.55×10^{-4}
27	66.302	53.0668	-8.61×10^{-4}	8.47×10^{-4}
29	66.8367	52.5422	-9.11×10^{-4}	9.01×10^{-4}
31	67.3694	52.0212	-1.03×10^{-3}	1.03×10^{-3}
33	67.9007	51.503	-9.87×10^{-4}	9.86×10^{-4}
35	68.4308	50.9873	-1.32×10^{-3}	1.33×10^{-3}
37	68.9601	50.4736	-7.07×10^{-4}	7.01×10^{-4}
39	69.4887	49.9618	-2.58×10^{-3}	2.64×10^{-3}

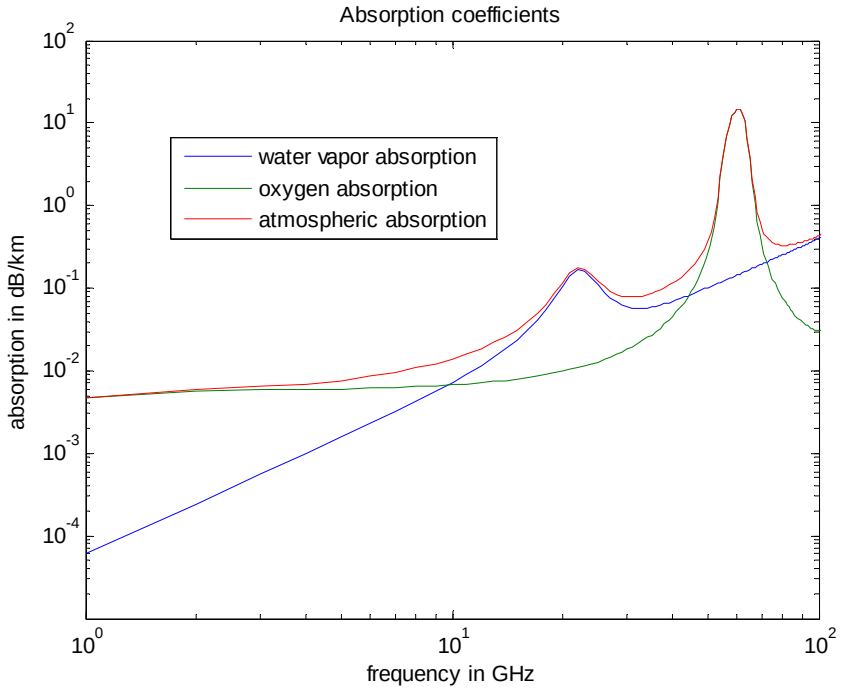

Figure 2.1: Water-vapor, oxygen, and atmosphere absorption coefficients at sea level.

2.3.2 Cosmic Emission

Background cosmic emission $T_{b0}(f)$ in (2.8) can be simplified into two factors [20]:

$$T_{b0}(f) = T_{CMB} + T_{gal}(f) \qquad (2.13)$$

where $T_{CMB} = 2.73K$ is the cosmic microwave background emission, and

$$T_{gal}(f) = T_{g_0}(\frac{f_o}{f})^{\beta} \qquad (2.14)$$

is the galactic emission. Both base temperature T_{g_0} and spectral index β are functions of the observed direction in the sky. $T_{gal}(f)$ is dependent on both frequency and direction. In general, galactic emission decreases with increasing frequency, and above 1 GHz is negligible. It is maximum when looking toward the center of galaxy, and minimum when observing along the pole about which the galaxy revolves [23]. By setting $\beta = 2.75$, $f_o = 0.408GHz$ and $T_{g_0} = 20K$, (2.13) will results a reasonable average cosmic noise temperature above 10 MHz (see Fig.2.2).

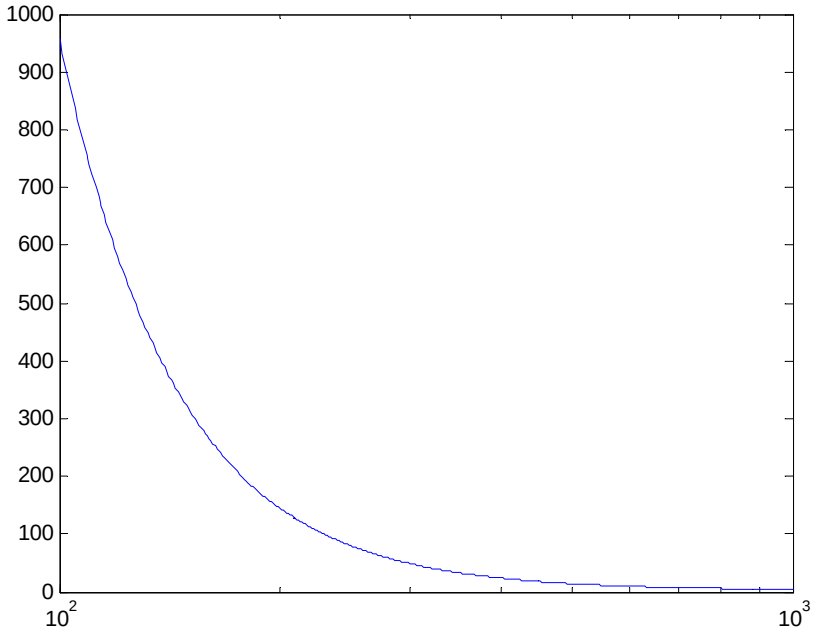

Figure 2.2: Average cosmic noise temperature.

2.3.3 Sky Brightness Temperature

For ground-based observations, sky brightness temperature is given by [20],

$$T_b^{sky}(f) = T_{b0}(f)e^{-\tau_v(\infty)/\cos\theta} + 1/\cos\theta \int_0^\infty k_a(f,s)T(s)e^{-\tau_v(s)/\cos\theta}ds \qquad (2.15)$$

where $\tau_v(\infty) = \int_0^\infty k_a(f,s)ds$ is zenith opacity.

Note that $k_a(f,s)$ given in (2.10) is in dB/km, which should be converted into NP/km first for calculation.

However, German's model is only valid for $\theta < 75^o$. For larger angles, the sky brightness temperature will become unacceptable, as shown in Fig. 2.3.

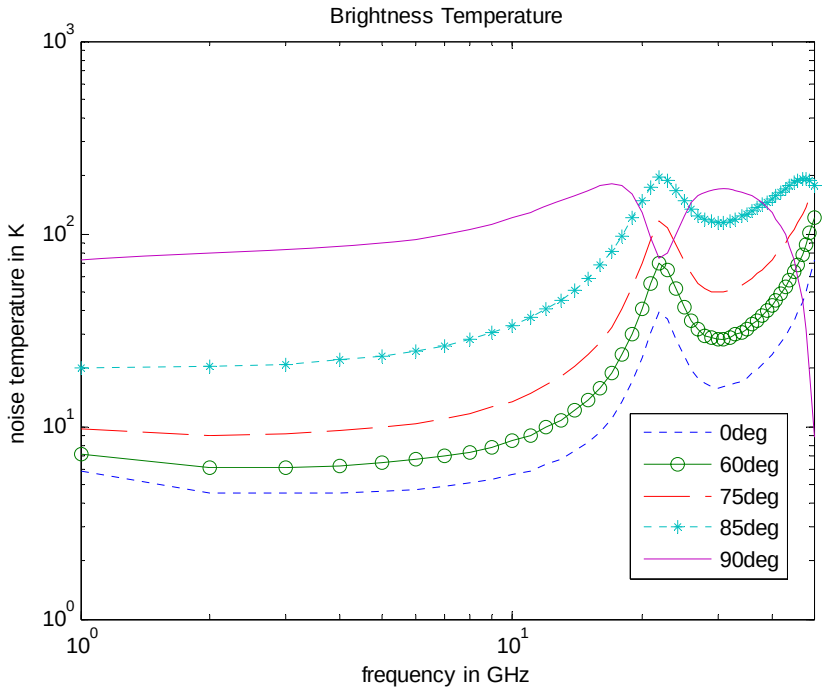

Figure 3: Sky brightness temperature.

By comparing the sky brightness temperature with that given in [23], German's model works well for $\theta < 75^o$, but quite undesirable for $\theta > 75^o$. This is because that it assumes a plane horizontally stratified atmosphere with a refractive index profile independent of altitude. For the real atmosphere, however, the earth curvature and the vertical gradient of the refractive index cause the term $1/\cos\theta$ in (2.15) inaccurate, especially for larger angles.

Y. Han [19] has proved that the effect of the refractive index profile on system calibration is negligible; and he provides a good solution for correcting the error introduced by neglecting the earth curvature.

In a spherically stratified atmosphere, the atmospheric opacity is given by [19]

$$\tau_v(\theta) = \int_0^{\infty} \frac{k_a(f,s)}{\sqrt{1-[\sin\theta/(1+s/R)]^2}} ds \qquad (2.16)$$

where $R = 6370.95km$ is the earth's radius.
By substituting (2.16) into (2.8), the accuracy of sky brightness temperature, especially at larger zenith angles will be improved.
Nevertheless, the sky brightness temperature given by [20] is accurate enough below 15 GHz even for $\theta > 75^o$ (see Fig.2.4).

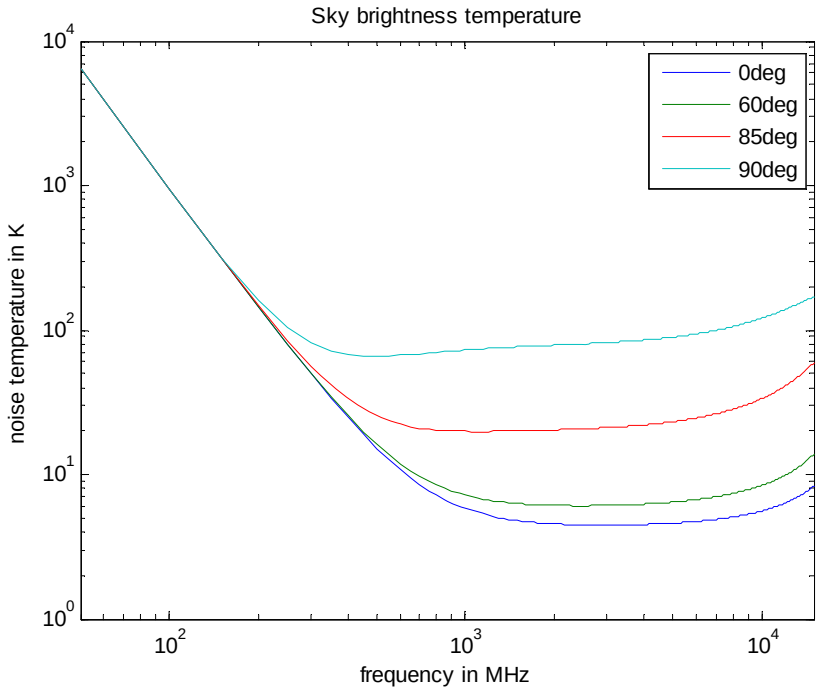

Figure 2.4: Sky brightness temperature.

2.3.4 Ground Emission and Scattering

Assuming the ground is dry land with $\varepsilon_r = 3.5$, and that reflections are very different for parallel and perpendicular polarizations, and that the far-side lobes of the co-polar pattern of the antenna are very low with respect to the maximum and comparable in value to the cross-polar pattern, which is usually the case for a radio telescope.
The noise temperature due to ground emission and scattering is given by

$$T_g(f) = [1-|\Gamma(\theta_1)|^2]T_{gnd} + |\Gamma(\theta_1)|^2 T_b^{sky}(f) \qquad (2.17)$$

where $T_{gnd} = 300K$ is a typical value for the physical temperature of the ground, and $|\Gamma(\theta_1)|^2$ is the average power reflection coefficient.

Note that θ_1 is the incident angle for the incoming wave with respect to the ground, thus has a relationship with the zenith angle θ as $\theta_1 = \pi - \theta$.

We denote parallel polarization reflection as $\Gamma_1(\theta_1)$, and perpendicular polarization $\Gamma_2(\theta_1)$, which are given by [24]

$$\Gamma_1(\theta_1) = \frac{(\varepsilon_r - \sin^2\theta_1)^{1/2} - \varepsilon_r \cos\theta_1}{(\varepsilon_r - \sin^2\theta_1)^{1/2} + \varepsilon_r \cos\theta_1} \qquad (2.18)$$

$$\Gamma_2(\theta_1) = \frac{\cos\theta_1 - (\varepsilon_r - \sin^2\theta_1)^{1/2}}{\cos\theta_1 + (\varepsilon_r - \sin^2\theta_1)^{1/2}} \qquad (2.19)$$

The average power reflection can be expressed as

$$|\Gamma(\theta_1)|^2 = [|\Gamma_1(\theta_1)|^2 + |\Gamma_2(\theta_1)|^2]/2 \qquad (2.20)$$

Ground emission and scattering noise based on (2.17) is calculated and plotted as shown in Fig.2.5.

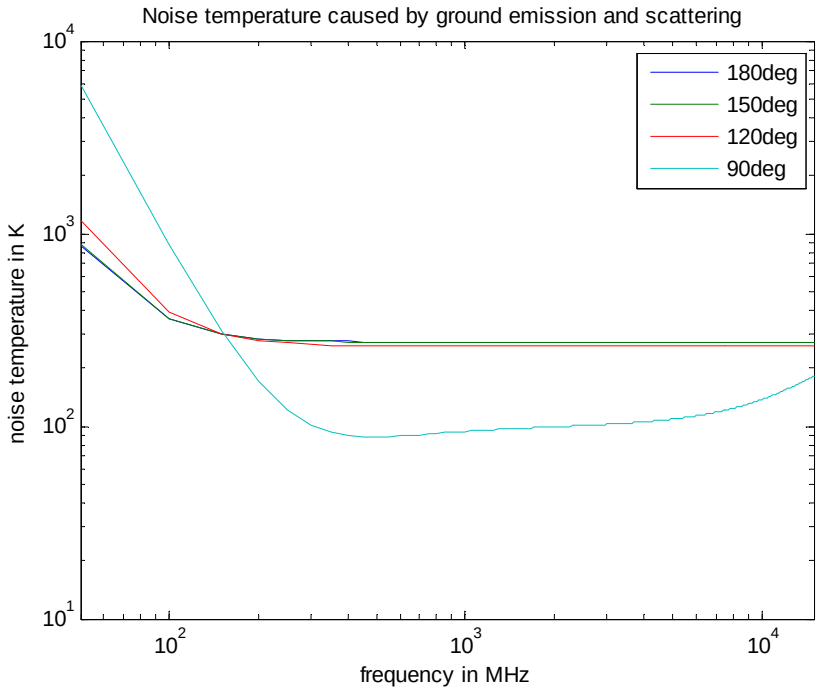

Figure 2.5: Noise temperature due to ground emission and scattering.

Note that the model of ground emission and scattering noise assumes the antenna responsive to two orthogonal polarizations.

3. Study of Receiver System Noise Temperature

Contributions to receiver system noise temperature differ a lot in wireless environments, e.g. mobile phones, and in radio observation environments, e.g. earth observation antennas. Hence they will be addressed in different chapters. This chapter will mainly focus on system noise temperature for radio telescopes, or satellite communication terminals. System noise temperature is the summation of antenna noise temperature T_{ant} and receiver noise temperature T_{rec}. Each of them is discussed in the following sections.

3.1 Antenna Noise Temperature

A ground-based radiometer is surrounded by the brightness noise temperature, as shown in Fig.3.1.

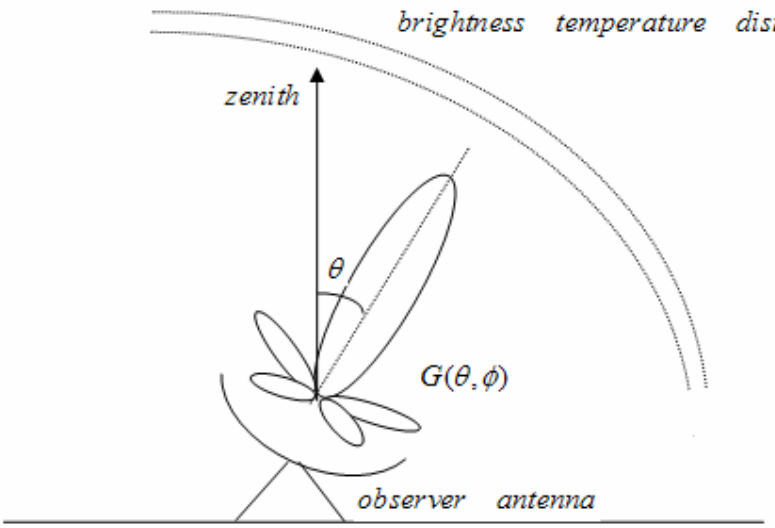

Figure 1: Antenna surrounded by brightness noise temperature.

The noise temperature seen by the antenna is given by [25]

$$T_a(f) = \frac{\int_{4\pi} T_b(f,\theta) G(\theta,\varphi) \sin\theta d\theta d\varphi}{\int_{4\pi} G(\theta,\varphi) \sin\theta d\theta d\varphi} \qquad (3.1)$$

where $G(\theta,\varphi)$ is antenna power radiation pattern, and T_b is brightness noise temperature defined as

$$T_b(f,\theta)=\begin{cases}T_{sky}(f,\theta), & 0\le\theta<\pi/2\\ T_g(f,\theta), & \pi/2\le\theta\le\pi\end{cases} \qquad (3.2)$$

with T_{sky} and T_g denoting sky and ground noise temperatures respectively.

For an actual antenna, dissipation loss and mismatch always exist. Therefore the antenna noise temperature is expressed as

$$T_{ant}(f)=T_a(f)e_{rad}+(1-e_{ohmic})T_p e_r \qquad (3.3)$$

where $T_p=290K$ is the physical temperature of the antenna, e_r is mismatch efficiency, e_{ohmic} is ohmic efficiency, or dissipation efficiency, and $e_{rad}=e_r e_{ohmic}$ is defined as radiation efficiency [25].

Usually, the approximated formula (3.4) is used to estimate the noise temperature seen by a reflector antenna, provided that its spillover efficiency e_{spill} is known.

$$T_a=T_{sky}e_{spill}+T_g(1-e_{spill}) \qquad (3.4)$$

GMRT antenna is used here as an example to compare the simplified approximation (3.4) with the standard formula (3.1).

The GMRT antenna power radiation pattern at 250 MHz is shown in Fig.3.2.

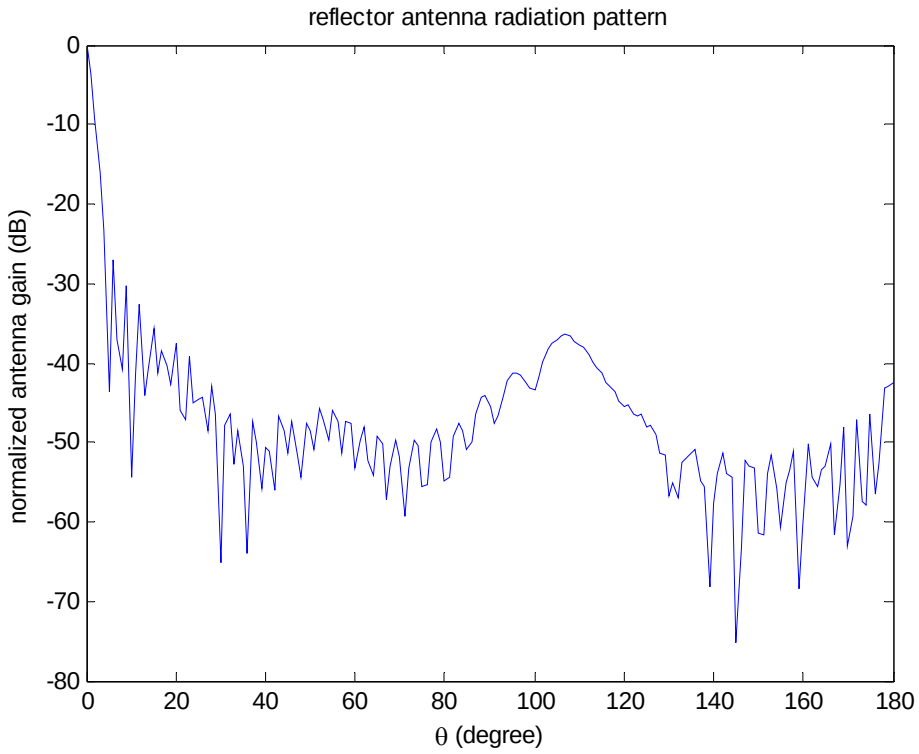

Figure 3.2: GMRT antenna radiation pattern at 250 MHz.

Using (3.1), the noise temperature picked up the antenna $T_a = 114K$. While using (3.4), and assuming a spillover efficiency of 90%, $T_a = 106K$. The difference is not much. In the following, (3.4) will be used to calculate the antenna noise temperature and consequently system noise temperature.

The antenna noise temperature of a reflector antenna can be expressed as

$$T_{ant} = T_{sky} e_{spill} e_{rad} + T_g (1 - e_{spill}) e_{rad} + (1 - e_{ohmic}^{refl}) T_p e_{spill} e_r + (1 - e_{ohmic}^{feed}) T_p e_r + (1 - e_{ohmic}^{cable}) T_p \quad (3.5)$$

where $e_{rad} = e_r e_{ohmic}^{refl} e_{ohmic}^{feed} e_{ohmic}^{cable}$ is the total radiation efficiency, with e_{ohmic}^{refl}, e_{ohmic}^{feed} and e_{ohmic}^{cable} as the dissipation efficiencies of the reflector, feed and cable, respectively. The dissipation efficiency is the reciprocal of the insertion loss, which is frequency dependent. T_{sky} and T_g is available from the brightness noise temperature model. Here we just assume that $e_{spill} = 90\%$, $e_{ohmic}^{refl} = 99\%$, $e_{ohmic}^{feed} = 99\%$ and $e_{ohmic}^{cable} = 97\%$ for simplicity. The antenna noise temperature based on the above assumptions is shown in Fig.3.3.

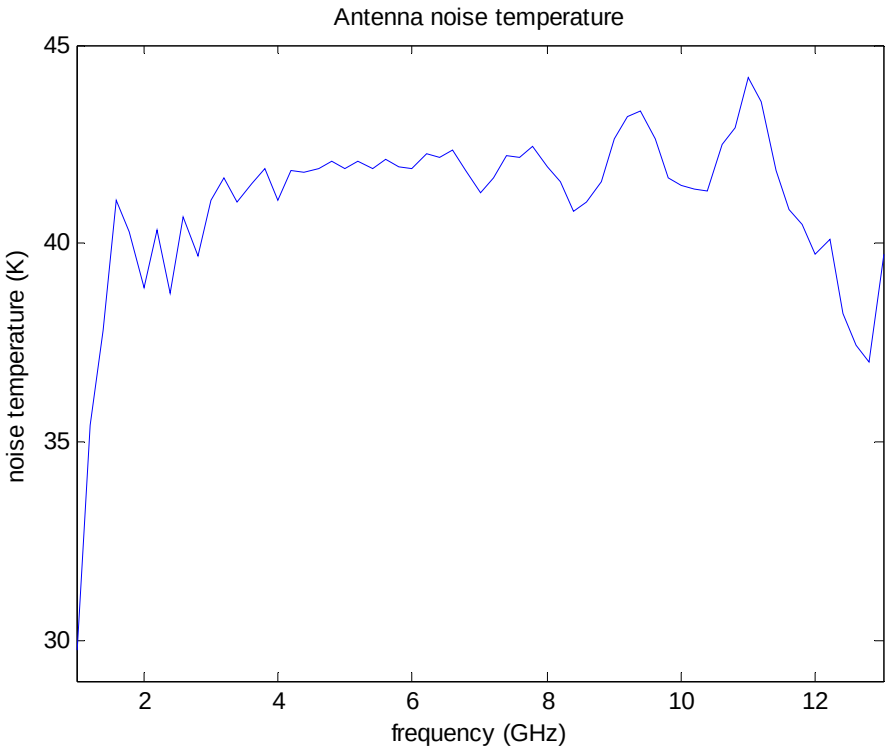

Figure 3.3: Reflector antenna noise temperature with ELEVEN antenna as the feed.

3.2 LNA

A LNA is usually used right after the antenna to provide sufficient transducer gain and minimum noise temperature. If the LNA gain is high enough, the noise temperature given by the next stages of the receiver (e.g. mixer) will be negligible. The receiver that will be studied here is the ELEVEN antenna after reflector with a broadband LNA, designed by Niklas Wadefalk from MC2, Chalmers. Fig.3.4 shows the schematic circuit of Niklas's LNA.

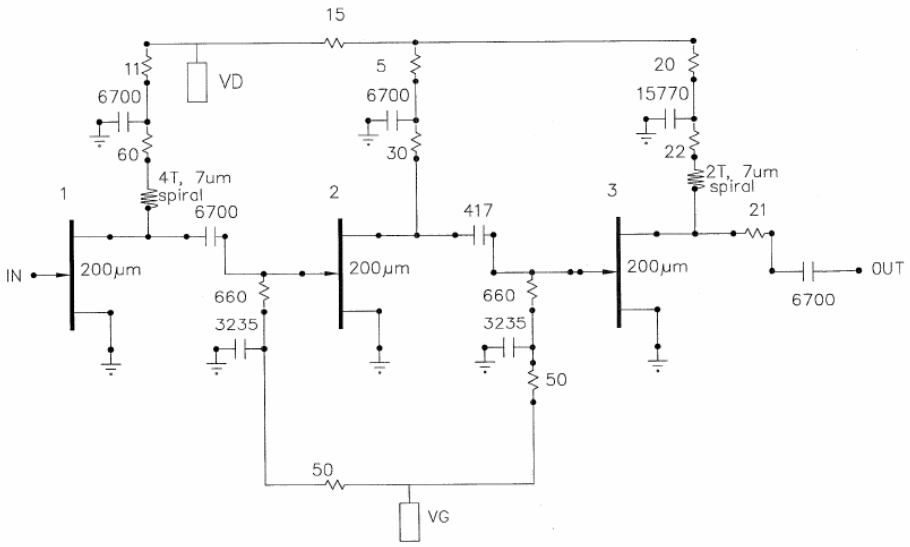

Figure 3.4: LNA schematic (Courtesy of Niklas Wadefalk).

The LNA shown in Fig.3.4 is without input matching network. Later on, we will show that the LNA is more or less noise matched even without the input matching network. But, in the aspect of power match an input matching network is needed.

The LNA is made unconditionally stable with or without input matching network (see Fig.3.5), which enable us to directly connect our ELEVEN antenna directly to it without oscillation.

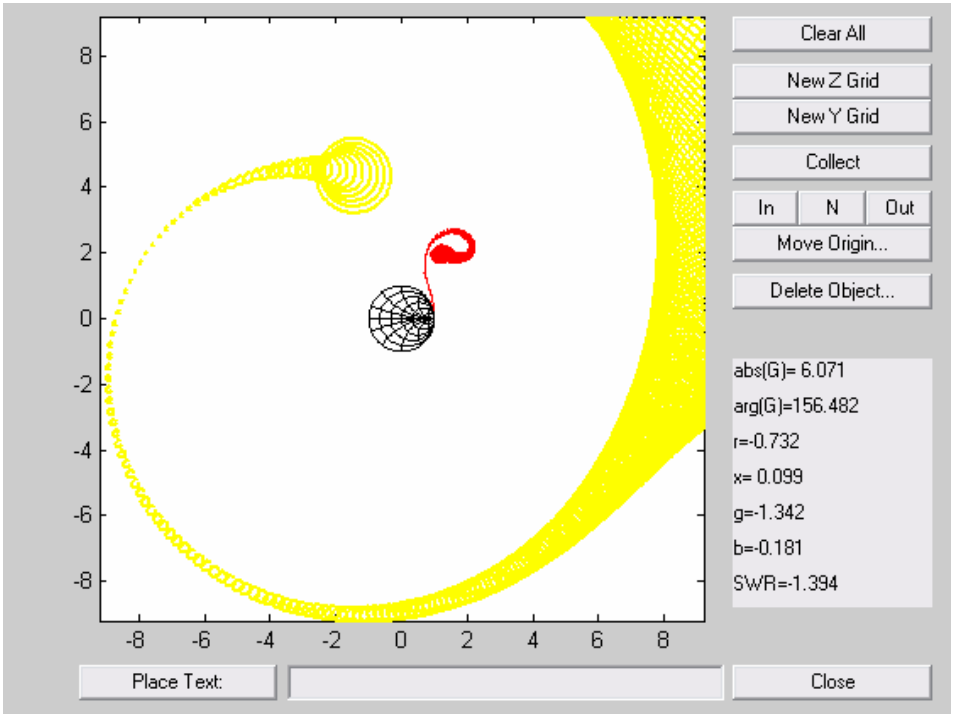

(a)

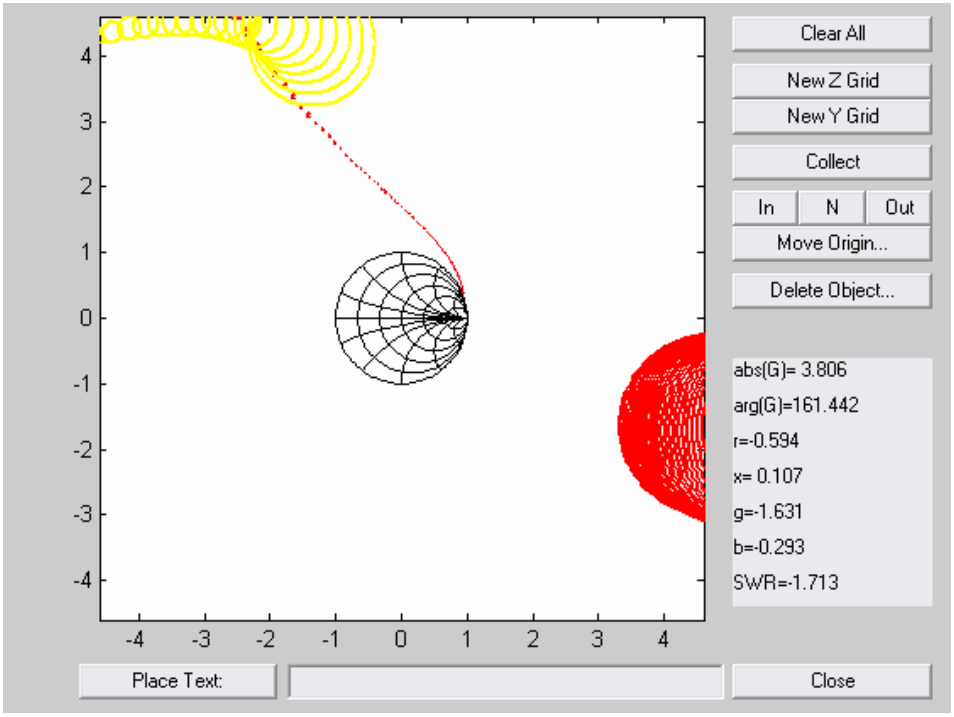

(b)

Figure 3.5: Input (red) and output (yellow) stability circles from 1 to 15 GHz: (a) LNA without input matching network; (b) LNA with input matching network.

Fig.3.6 shows the input reflection of the ELEVEN antenna. The blue curve is the return loss with 75 ohms load, and the green curve 50 ohms load.

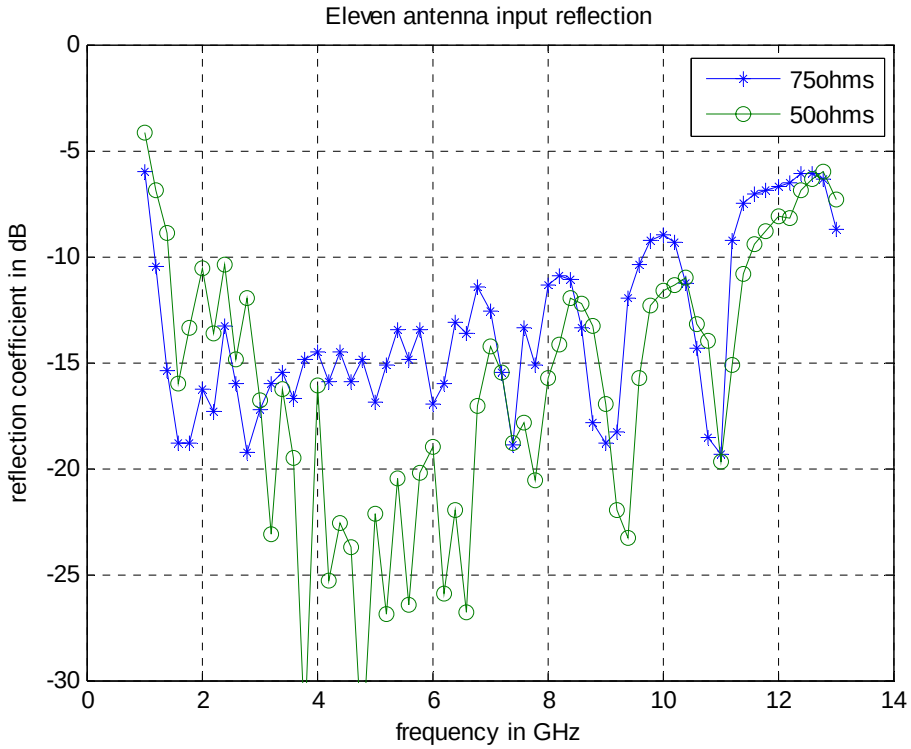

Figure 3.6: Return loss of ELEVEN antenna.

If there are no cables in between ELEVEN antenna and LNA, the antenna input impedance is the source impedance seen by the LNA. The LNA noise temperature is shown in Fig.3.7. Blue curve corresponds to LNA noise temperature when it is directly connected with ELEVEN antenna. For references, another two curves are plotted also to show LNA noise temperature when LNA source impedances are 75 ohms (red), and 50 ohms (green).

The LNA noise factor can be calculated using equation (3.6)

$$F = F_{\min} + \frac{4r_n |\Gamma_s - \Gamma_{opt}|^2}{(1-|\Gamma_s|^2)|1+\Gamma_{opt}|^2} \qquad (3.6)$$

where $F_{\min}$ is the minimum noise factor, r_n is the equivalent normalized noise resistance, Γ_s is source reflection coefficient and Γ_{opt} optimal reflection coefficient. The noise temperature can be converted from noise factor by [33]

$$T_e = T_0(F-1) \qquad (3.7)$$

where T_e is equivalent noise temperature, and T_0 is ambient temperature, which is usually equal to 290 K for room temperature. Combing (3.6) and (3.7), the LNA noise temperature can be expressed as

$$T_{LNA} = T_0(F_{\min} - 1) + \frac{4r_n T_0 |\Gamma_s - \Gamma_{opt}|^2}{(1-|\Gamma_s|^2)|1+\Gamma_{opt}|^2} \tag{3.8}$$

It is shown that the LNA with input matching network (Fig.3.7 (b)) provides better performance in terms of noise temperature below 12 GHz; but, above 12 GHz, there is a noise temperature peak. While the LNA without input matching above 12 GHz seems better in terms of noise temperature.

The reason can be shown by plotting the noise circles of the LNA and input impedance of the ELEVEN antenna (see Fig.3.8). The input matching network is used to optimize LNA performance assuming the source impedance is 75 ohms. Thus the centers of the 0.9 dB (67 K) noise circles of the matched LNA is concentrated around 75 ohms in smith chart from 1 to 13 GHz, as shown in Fig.3.8 (b). However, the impedance of ELEVEN antenna at 12.6 GHz is around 50+j50 ohms (see Fig.3.8 (c)). That's why there is a noise temperature peak above 12 GHz for the matched LNA. On the other hand, the 0.9 dB noise circles of the unmatched LNA is concentrated around 40+j50 ohms (close to 50+j50 ohms), as can be seen in Fig.3.8 (a), therefore the unmatched LNA just happens to provide a better noise performance above 12 GHz.

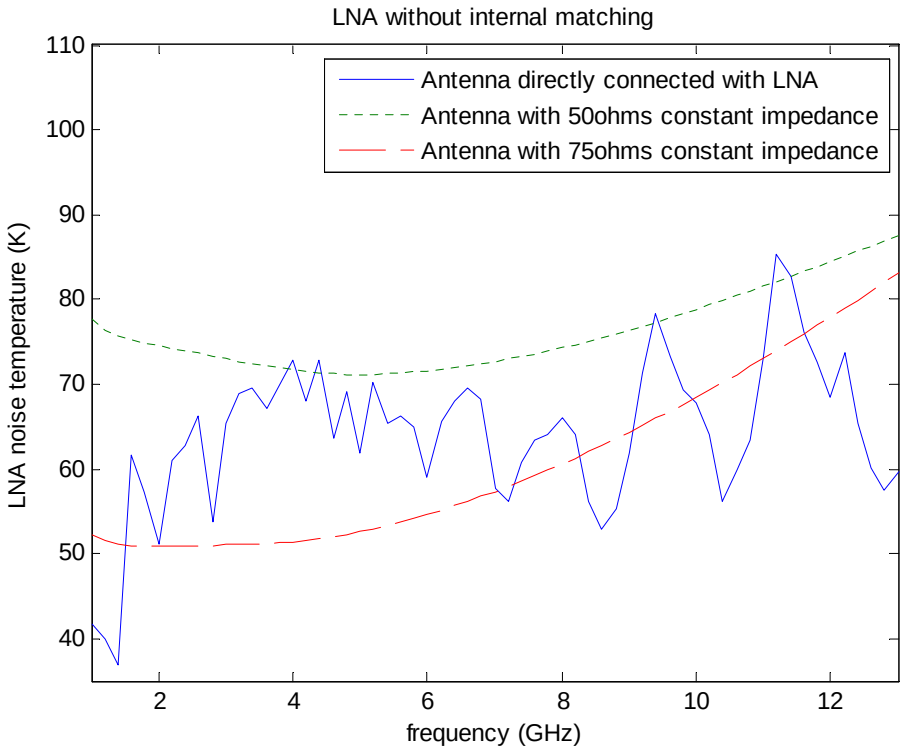

(a)

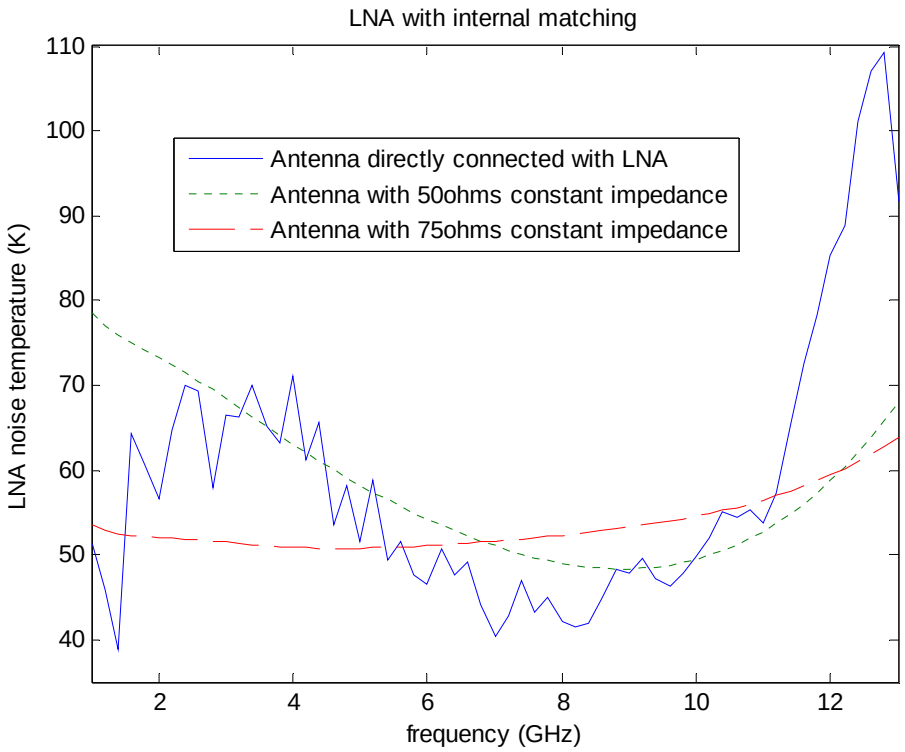

(b)

Figure 3.7: LNA noise temperature: (a) Matched LNA; (b) Unmatched LNA.

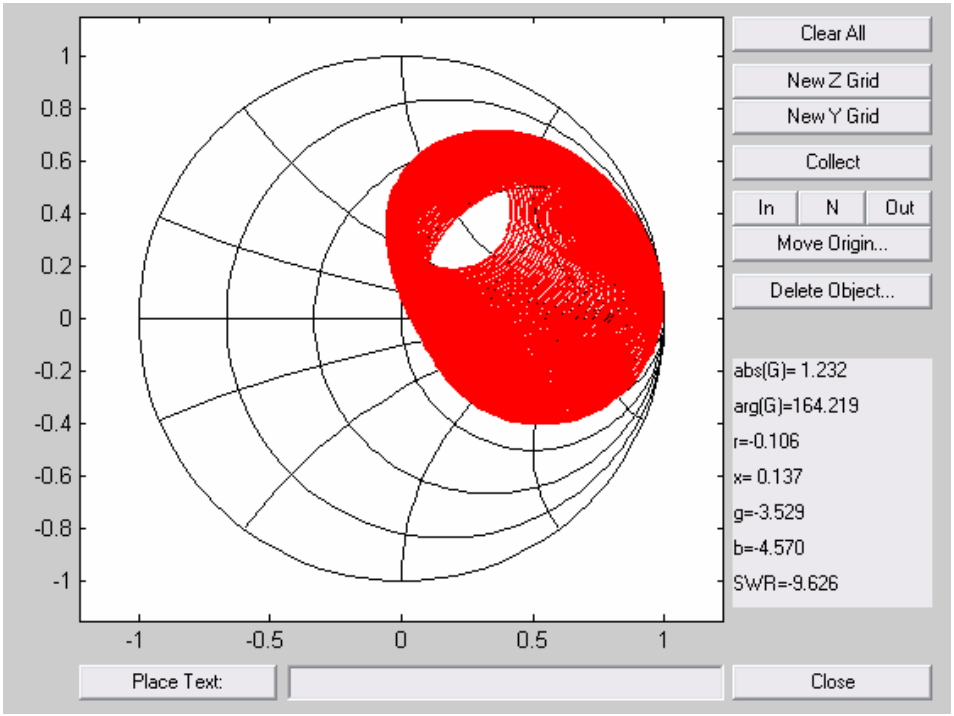

(a)

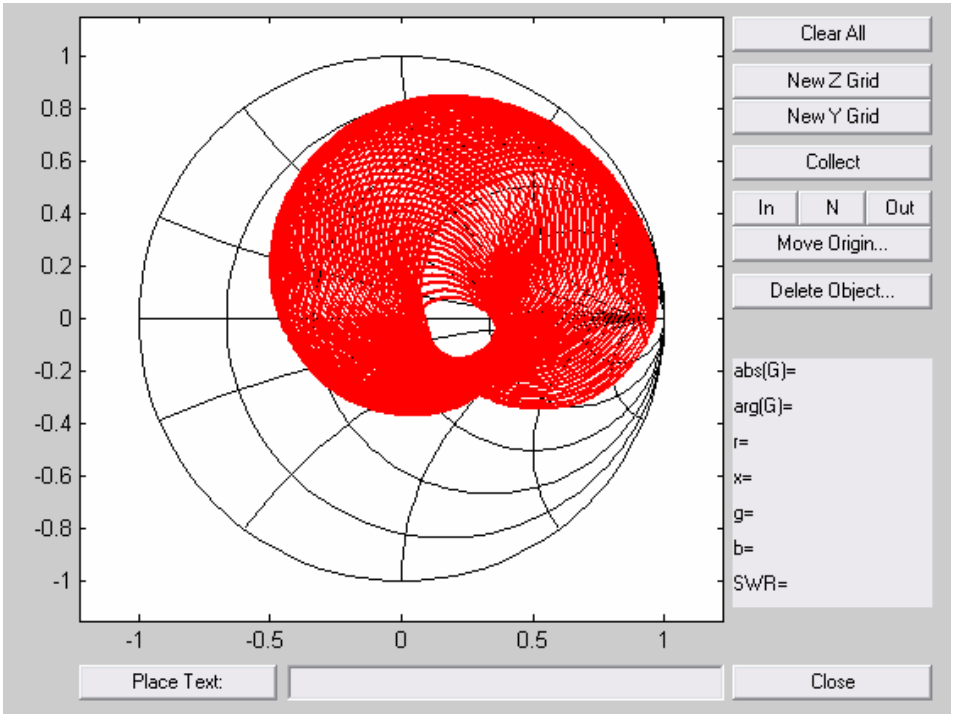

(b)

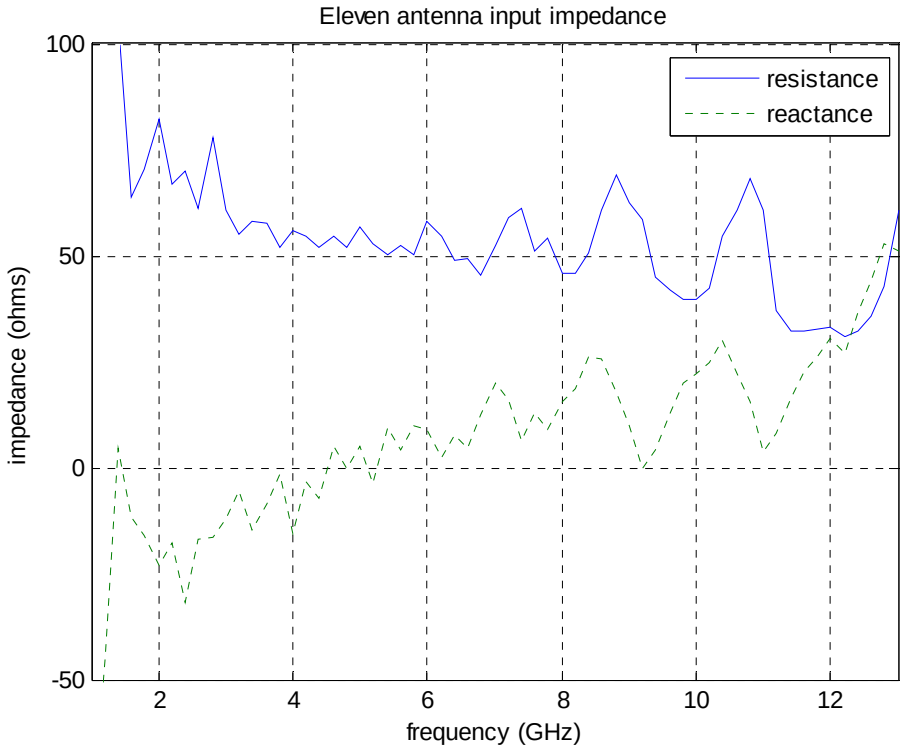

(c)

Figure 3.8: (a) 0.9dB noise circles of unmatched LNA; (b) 0.9dB noise circles of matched LNA; (c) input impedance of ELEVEN antenna.

The cables in between ELEVEN antenna and LNA will change the source impedance seen by the LNA, and consequently the LNA noise temperature. Fig.3.9 shows the LNA noise temperatures with cables in between it and ELEVEN antenna. Fig.3.9 (a) shows the unmatched LNA with 50 ohms 0 cm long (blue), 1 cm long (green) and 5 cm long (red) cables. Fig.3.9 (b) shows the unmatched LNA with 75 ohms 0 cm long (blue), 1 cm long (green) and 5 cm long (red) cables. Fig.3.9 (c) shows the matched LNA with 50 ohms 0 cm long (blue), 1 cm long (green) and 5 cm long (red) cables. Fig.3.9 (d) shows the matched LNA with 75 ohms 0 cm long (blue), 1 cm long (green) and 5 cm long (red) cables. Generally speaking, the cables degrade LNA noise performance.

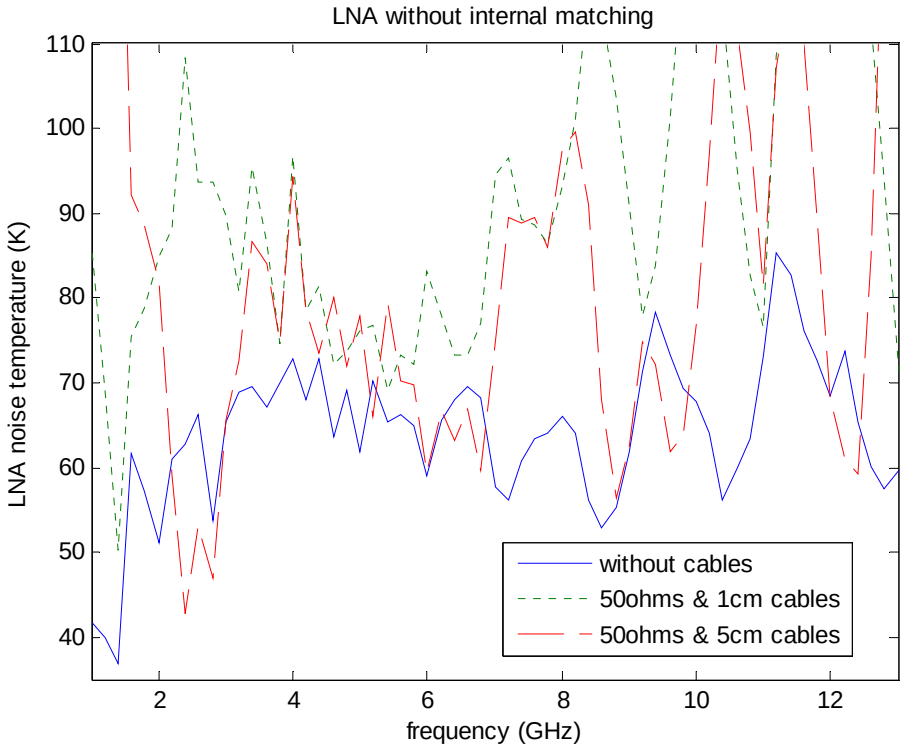

(a)

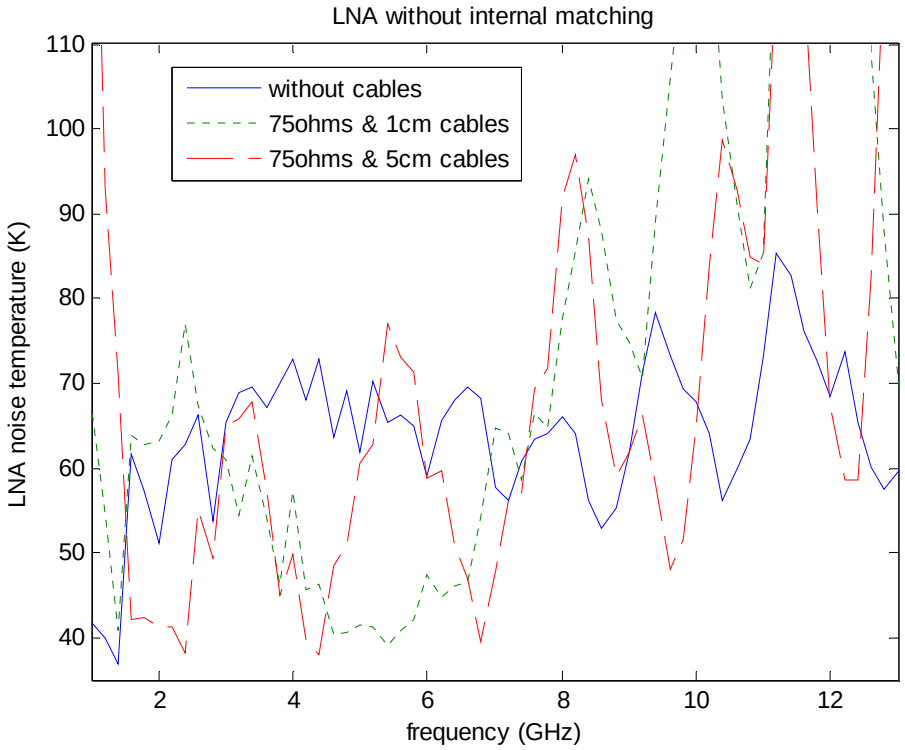
LNA without internal matching
without cables
75ohms & 1cm cables
75ohms & 5cm cables
LNA noise temperature (K)
frequency (GHz)
110
100
90
80
70
60
50
40
2
4
6
8
10
12

(b)

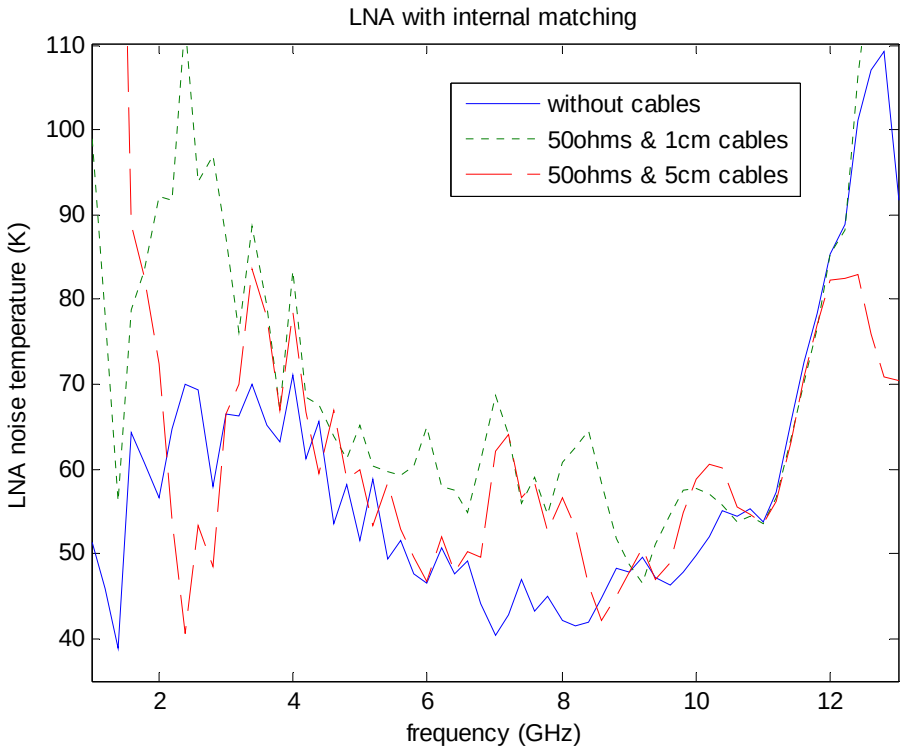
LNA with internal matching
without cables
50ohms & 1cm cables
50ohms & 5cm cables
LNA noise temperature (K)
frequency (GHz)
110
100
90
80
70
60
50
40
2
4
6
8
10
12

(c)

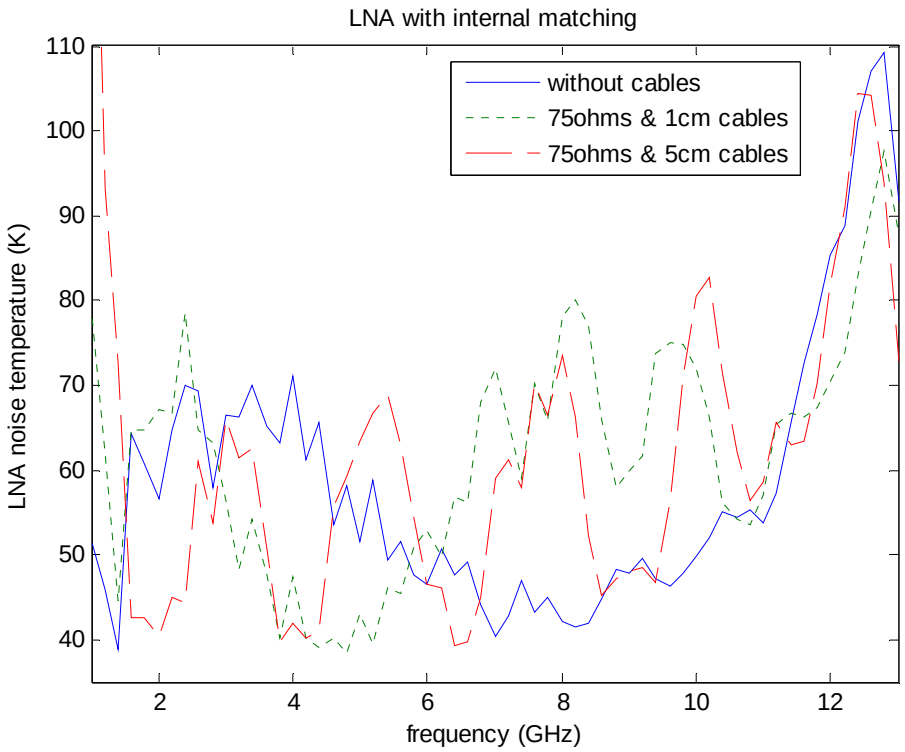

(d)

Figure 3.9: LNA noise temperature: (a) unmatched LNA with 50 ohms cables; (b) unmatched LNA with 75 ohms cables; (c) matched LNA with 50 ohms cables; (d) matched LNA with 75 ohms cables.

The transducer gain of the LNA is shown in Fig.3.10.

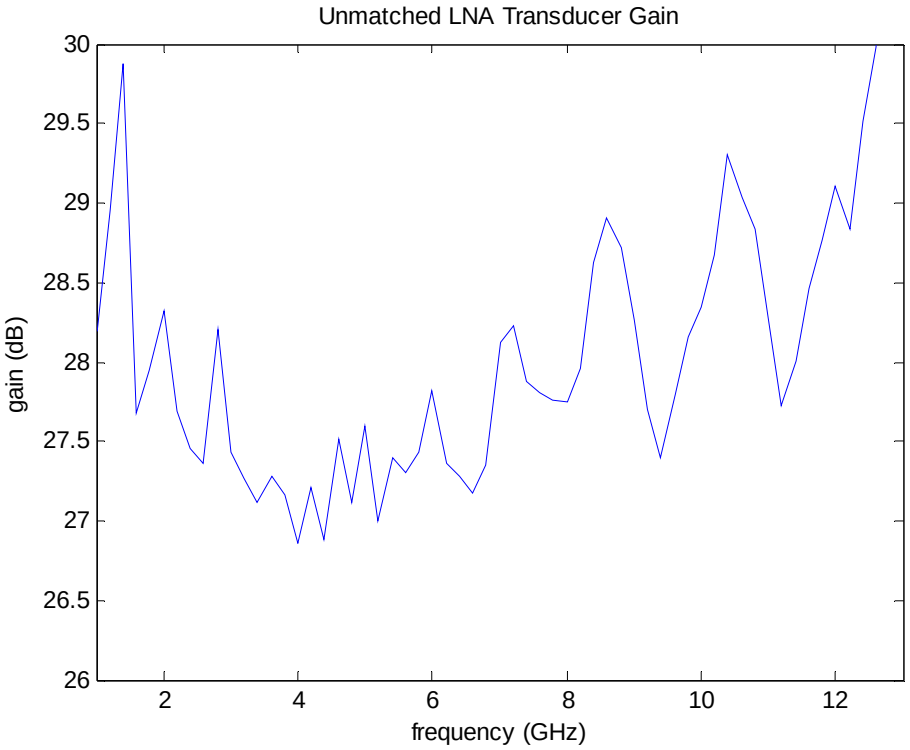

(a)

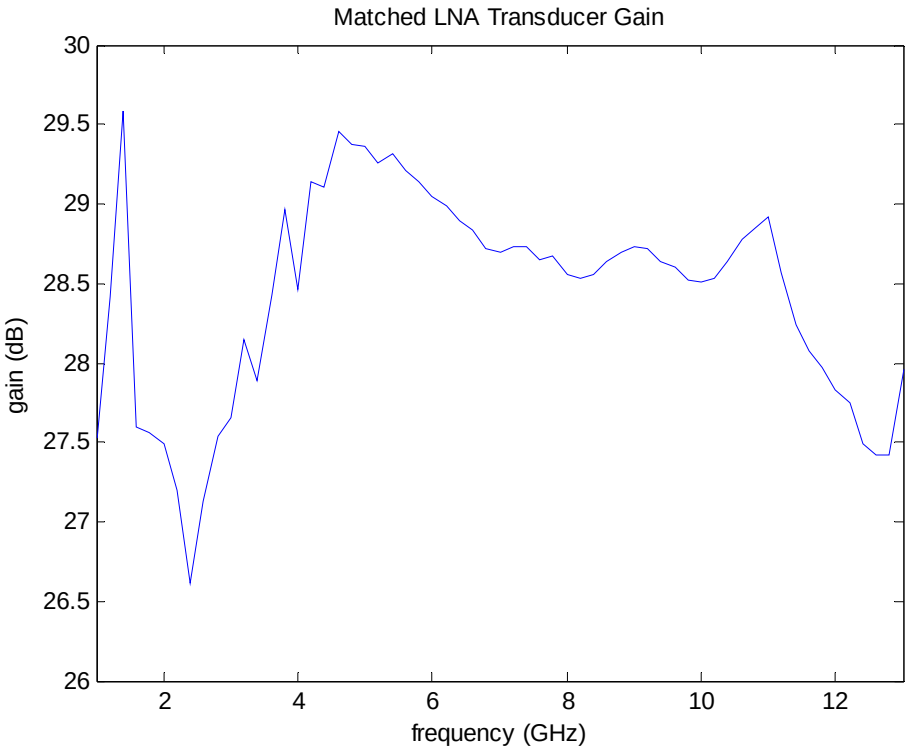

(b)

Figure 3.10: Transducer gain: (a) unmatched LNA; (b) matched LNA.

It is seen in Fig.3.9 that the transducer gain of the LNA is around 28 dB from 1 to 13 GHz. The noise temperature contributed by the next stages will be reduced by the LNA gain, and thus become negligible provided that the noise figure of the next stage components are not very large. Hence, the receiver system temperature can be approximated by the LNA noise temperature.

3.3 System Noise Temperature

The system noise temperature is shown in Fig.3.11. Fig.3.11 (a) shows the unmatched LNA with 50 ohms 0 cm long (red), 1 cm long (green) and 5 cm long (blue) cables. Fig.3.11 (b) shows the unmatched LNA with 75 ohms 0 cm long (red), 1 cm long (green) and 5 cm long (blue) cables. Fig.3.11 (c) shows the matched LNA with 50 ohms 0 cm long (red), 1 cm long (green) and 5 cm long (blue) cables. Fig.3.11 (d) shows the matched LNA with 75 ohms 0 cm long (red), 1 cm long (green) and 5 cm long (blue) cables.

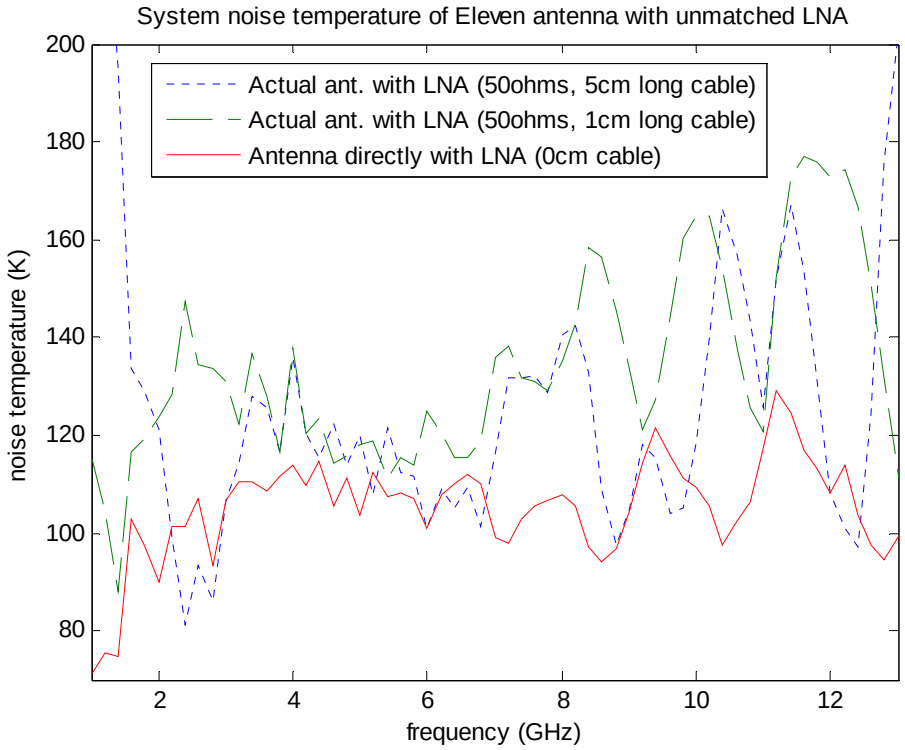

(a)

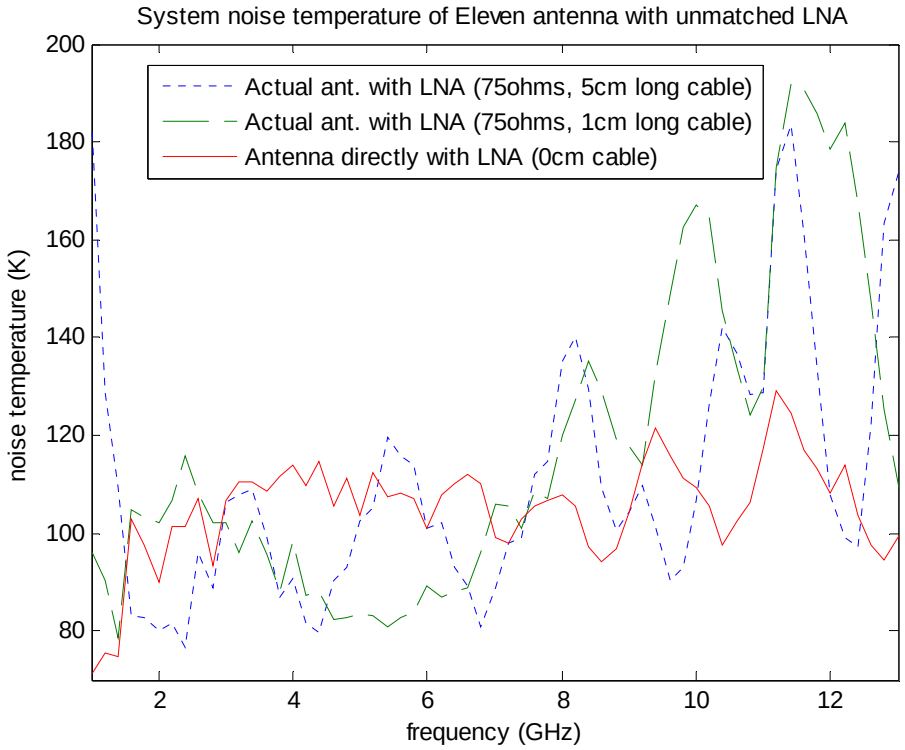
System noise temperature of Eleven antenna with unmatched LNA
Actual ant. with LNA (75ohms, 5cm long cable)
Actual ant. with LNA (75ohms, 1cm long cable)
Antenna directly with LNA (0cm cable)
noise temperature (K)
frequency (GHz)
200
180
160
140
120
100
80
2
4
6
8
10
12

(b)

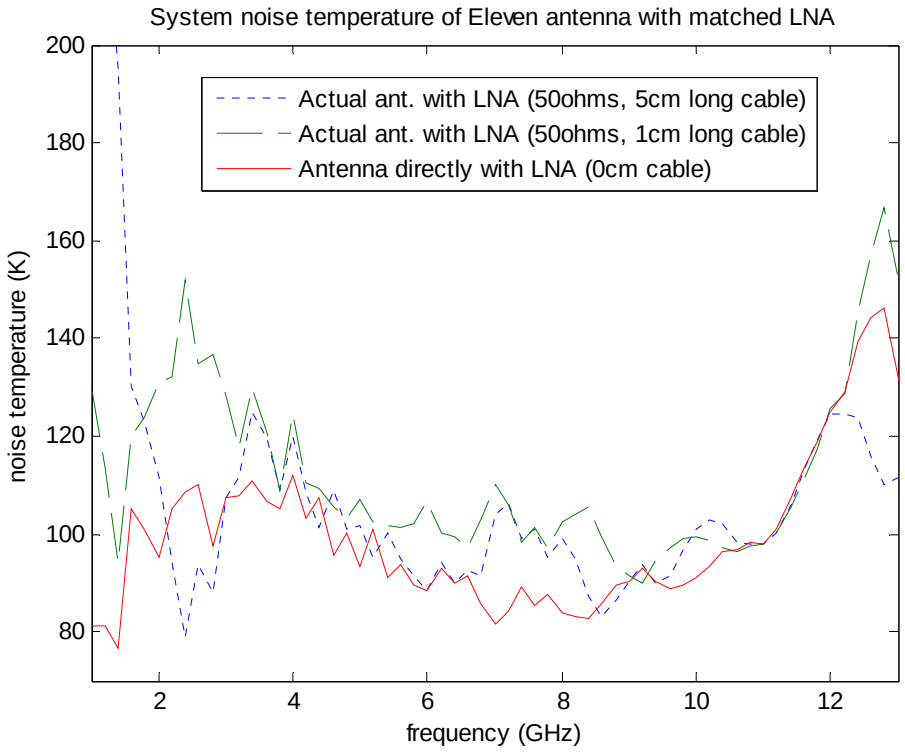
System noise temperature of Eleven antenna with matched LNA
Actual ant. with LNA (50ohms, 5cm long cable)
Actual ant. with LNA (50ohms, 1cm long cable)
Antenna directly with LNA (0cm cable)
noise temperature (K)
frequency (GHz)
200
180
160
140
120
100
80
2
4
6
8
10
12

(c)

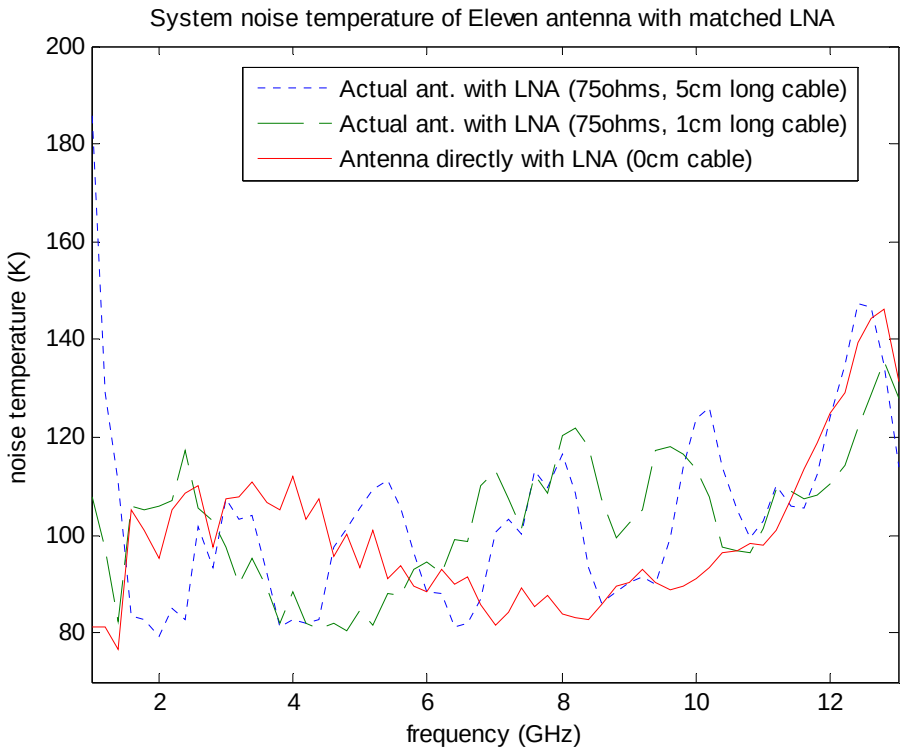

(d)

Figure 3.11: System noise temperature: (a) unmatched LNA with 50 ohms cables; (b) unmatched LNA with 75 ohms cables; (c) matched LNA with 50 ohms cables; (d) matched LNA with 75 ohms cables.

Note that both the feed and LNA are supposed at room temperature. For Radio telescope, both the feed and LNA need to be cooled to low temperature to reduce the system noise temperature.

4. Mobile Phone System Noise Temperature

The first generation (1G) cellular phone systems are analog. Advanced mobile phone services (AMPS), Nordic mobile telephone (NMT) and Nippon telephone and telegraph (NTT) are examples of the 1G mobile phone systems. The second generation (2G) systems are designed based on digital transmission. 2G systems includes global system for mobile communications (GSM) and DCS 1800 systems, north American dual-mode cellular system Interim Standard (IS-54 and IS-95) systems, and Japanese personal digital cellular (PDC) system. The third generation (3G) mobile communication systems are developed to provide users with high data rates to transmit multi-media. Universal mobile telecommunications system (UMTS) and international mobile telecommunications (IMT) are typical 3G systems [26].
Here only GSM will be used for the study of mobile phone system noise temperature.

4.1 Mobile Phone Antenna

The first mobile phone antenna used in 1984 is a half-wavelength monopole antenna. At that time the typical weight of a cellular phone is 850 g. By 1999, the weight had been reduced less than 90 g. The volume of the mobile phones had also been reduced tremendously [27]. All of these require smaller mobile phone antennas. Consequently, normal mode helical antenna (NMHA), meandered line antenna and planar inverted F antenna (PIFA) are developed. Among them, PIFA seems the most popular one. All these mobile phone antennas are used trying to achieve larger bandwidth, lower specific absorption rate (SAR), higher radiation efficiency and omni-directional radiation pattern. Here we just assume an arbitrary omni-directional mobile phone antenna for the sake of system noise temperature estimation.

Usually, human body is presented, which results power absorption associated with SAR. Lots of researches have been done to investigate the human tissue absorption [28]-[32]. It has been shown that human tissue absorption is mainly due to the head and hand. And the absorption varies with the mobile phone antenna types, mobile phone tilt angles, distance from head, size of head, right or left cheek, hand positions and operating frequency. Pedersen [29] shows that the hand positions on the phone effects the absorption the most. For PIFA antenna, hand loss could be 8 dB at the worst case. Zervos [31] found that 50% absorbed power reduction can be achieved by moving the phone 1 cm away from the head. Kivekäs [32] shows that the increase in SAR and decrease in radiation efficiency are affected by the phone chassis.
There are too many factors affecting body loss and consequently radiation efficiency. It is impossible to incorporate all the factors when estimating mobile phone system noise temperature. Here we just make some necessary assumptions: 1800 MHz

operating frequency, 2.5 dB loss by head, 2 dB loss by hand, -6 dB antenna return loss, and 1.5 dB ohmic loss introduced by antenna, diplexer, duplexer, cable etc.
The mobile phone antenna radiation efficiency can be defined as

$$e_{rad} = e_r e_{diss} e_{bloss} \qquad (4.1)$$

where e_{diss} is dissipative loss efficiency caused by mobile phone hardware, such as antenna, switch, duplexer and so on, e_{bloss} is the efficiency caused by human body absorption, or body loss.

4.2 Mobile Phone Antenna Noise Temperature

In theory, the noise temperature picked up by a mobile phone can be calculated using (3.1). But the brightness noise temperature T_b in (3.1) must be replaced by the actual background noise temperature that surrounds the mobile phone antenna. In a mobile wireless environment, the background noise temperature could be very complicated, and it changes a lot with space and time. Therefore, in practice (3.1) is never used for a mobile phone antenna. In a mobile wireless environment, the antenna noise temperature can be considered as the noise temperature contributed by human body, hardware ohmic loss and other surrounding environments.

4.2.1 Human Body Contribution

If we assume 2.5 dB loss by the head and 2 dB loss by hand at upper GSM band, then total body loss is 4.5 dB, which means 65% power radiated by the mobile phone is absorbed by human tissue. Based on the above assumptions, the mobile phone antenna has a radiation efficiency of -7 dB, namely 19%.
Note that at 900 MHz band, the body loss introduced by the head is larger (up to 4~5 dB), and that the total radiation efficiency in the worst case could be as low as -17 dB.

Here we denote the antenna noise temperature contributed by body loss as

$$T_{body} = T_{human} e_{rad} = 59K \qquad (4.2)$$

where $T_{human} \approx 310K$ is the physical temperature of a human body.

4.2.2 Hardware Ohmic Loss Contribution

Assuming 1.5 dB ohmic loss introduced by antenna, diplexer, duplexer, cable etc, the noise temperature contributed by this ohmic loss is given by

$$T_{ohmic} = (1 - e_{ohmic})T_0 e_r = 88K \qquad (4.3)$$

where T_0 is the physical temperature of the mobile phone; we assume it is 300 K, slightly higher than room temperature, in that it is held by a "hot" hand.

4.2.3 Environments Contribution

Here for simplicity, we just assume two extreme scenarios: one is in an open area without any blocking structures or trees, the other is in a room without any widows.

4.2.3.1 Open area environment contribution

In the open area, the noises come from the sky and ground is like brightness noise temperature. Fig.4.1 shows the noise temperature picked up by an omni-directional antenna. As shown in Fig.4.1, from 1 to 13 GHz, the noise temperature just increases from 113 K to 128 K. Actually there is not much difference at 900 MHz and 1800 MHz. Here we assume the noise temperature picked up by a mobile phone antenna is 120 K, slightly higher to account for the "hot" wireless environment, and denote the noise temperature contributed by the open area environment as

$$T_{openarea} = 120 e_{rad} = 23K \qquad (4.4)$$

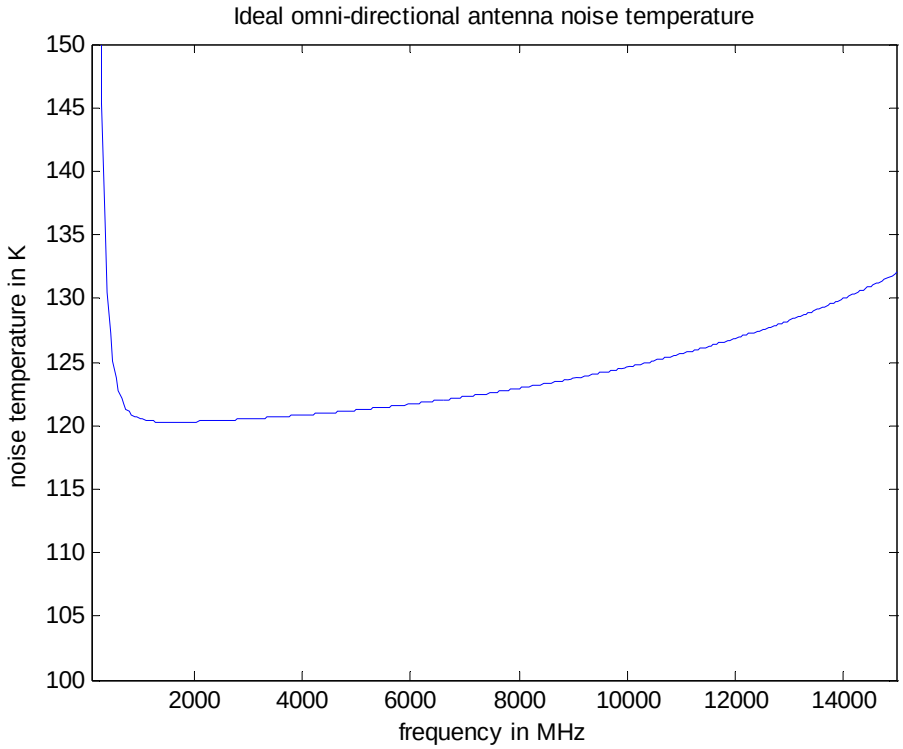

Figure 4.1: Noise temperature seen by an omni-directional antenna from 100 MHz to 15 GHz.

Note that the noise temperature seen by an omni-directional antenna at below 800 MHz increased dramatically due to the cosmic noise.

4.2.3.2 Indoor environment contribution

As an extreme case, we assume that the mobile phone is in a room without any window, and that the ground, walls and ceiling have the same physical temperature of 300 K. Then the noise temperature contributed by the indoor environment can be calculated as

$$T_{indoor} = 300 e_{rad} = 57K \qquad (4.5)$$

In summary, the mobile antenna noise temperature for open area and indoor cases can be denoted as (4.6) and (4.7) respectively.

$$T_{ant}^{openarea} = T_{body} + T_{openarea} + T_{ohmic} = 170K \qquad (4.6)$$

$$T_{ant}^{indoor} = T_{body} + T_{indoor} + T_{ohmic} = 204K \qquad (4.7)$$

4.3 Mobile Transceiver Hardware

A typical mobile transceiver block diagram is shown in Fig.4.2. It is a proposed 2G GSM transceiver where direct conversion is used for the receiver. Many components in this circuit can be integrated into two or three chips, with a total parts count of less than 90 [33]. Actually, there are already commercial monolithic devices that integrate all of the functions necessary to implement a multi-band homodyne global system for mobile phone except for the power amplifier (PA) and radio frequency (RF) passives [34].

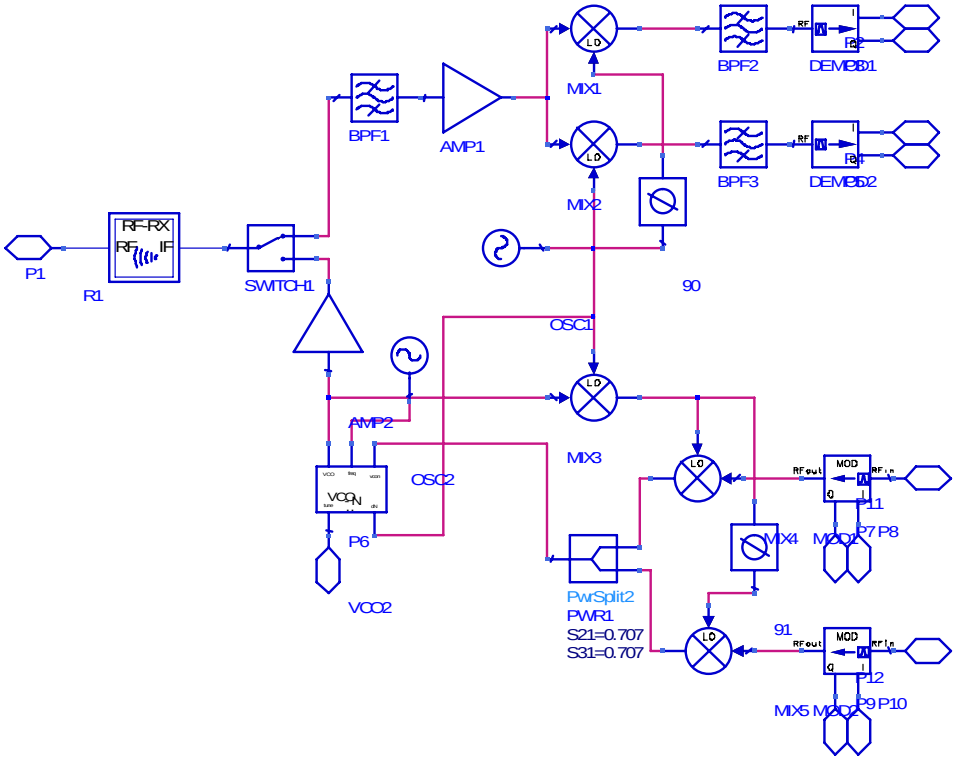

Figure 4.2: Transceiver schematic diagram.

4.3.1 Mobile receiver noise temperature

In order to estimate the mobile receiver noise temperature, Fig.4.2 is further simplified into Fig.4.3. And assumptions about the LNA, mixer, PA and duplexer must be made.

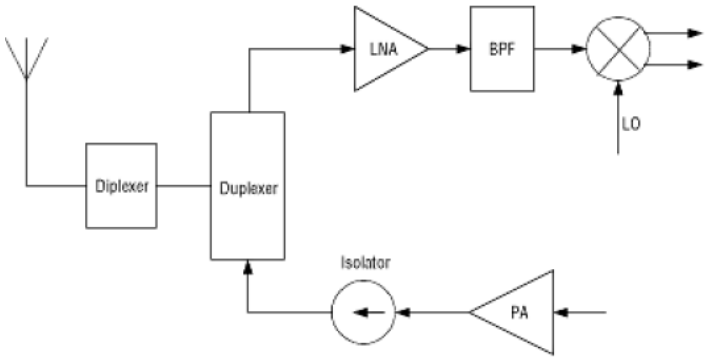

Figure 4.3: Simplified transceiver block diagram.

4.3.2 LNA in Cellular Phones

The LNA in mobile phone is based on CMOS technology instead of HEMT, which means that the performance of LNA used in a cellular phone can not be as good as that in a radio telescope. A summary of CMOS LNA is presented in [35]. For noise temperature study, noise figure (NF) and LNA gain have to be assumed, while LNA IIP3 is out of our concern.

The NF is a vital parameter, which affects profoundly the system noise temperature. A minimum NF promises a low system noise temperature. But a reduction in NF usually degrades the linearity of the LNA. For practical use, the NF of LNA is usually above 0.8 dB in a cellular phone.

The LNA gain must be high enough to overcome the noise contribution of the following circuit stages, which may otherwise degrade the receiver sensitivity. However, the gain is constrained by the strong unwanted signals and the linearity of the following stages (for example, if the LNA gain is too high, the mixer will overload). An LNA with a gain of 14 dB to 16 dB is a proper selection for mobile phones [36]. The LNA achieves 14.5 dB gain with a typical NF of 1.1 dB [37].

Thus, we assume a LNA with 15 dB gain and 1.1 dB NF here.

4.3.3 Mixer in Cellular Phones

Active mixers are usually used in mobile phones. A typical mixer has a gain of 13 dB and NF of 6.5 dB [37]. And these are also our assumption here.

The LNA cascaded with mixer together has a chain gain of 28 dB, which is high enough to suppress the noise contribution from the circuit stages after the mixer. Hence, the circuits after mixer are omitted in Fig.4.3.

4.3.4 PA in Cellular Phones

A cellular phone is a transceiver, which means that in addition to receiving it must transmit simultaneously as well. The PA is the most vital component in the transmitting chain. Different PA configurations for GSM are studied in [38]. The most important parameters for PA are power efficiency and intermodulation distortion. But here we are only interested in its power spectral density (PSD) in the receiver frequency band, in that the PSD of a PA will contribute to the system noise temperature.

A typical power amplifier has an output thermal noise PSD in the receiver frequency band of -135dBw/Hz [36]. Assuming a 41 dB attenuation through the duplex from transmitter to receiver. Noise PSD leakage into receiver is -176dBw/Hz. The conversion from PSD into noise temperature is given by

$$T_{PA} = \frac{P_{PSD}}{k} \qquad (4.8)$$

where k is Boltzmann constant.

Using (4.8), the noise temperature contribution from PA can be calculated as 182 K. Note that the duplexer isolation is vital to suppress the noise leakage from PA to receiver.

4.4 Mobile Phone Receiver Noise Temperature

The receiver noise temperature of a mobile phone can be expressed as

$$T_{rec} \approx T_{LNA} + \frac{T_{mix}}{G_{LNA}} + \frac{T_{PA}}{L_{dupl}} \qquad (4.9)$$

Based on the above assumptions, using (4.9) the mobile phone receiver noise temperature is calculated as 302 K.

4.5 System Noise Temperature of a Cellular Phone

The system noise temperature of a cellular phone is the summation of the antenna noise temperature and the receiver noise temperature.

Assume that the receiver noise temperature does not change with the environment, the system noise temperature for open area and indoor cases can be calculated as (4.10) and (4.11) respectively.

$$T_{sys}^{openarea} = T_{ant}^{openarea} + T_{rec} = 472K \qquad (4.10)$$

$$T_{sys}^{indoor} = T_{ant}^{indoor} + T_{rec} = 506K \qquad (4.11)$$

Note that the man-made noise is not included here.

Usually mobile wireless communications are constrained by the interferences from a nearby transmitter or base station rather than the ambient noise temperature.

5. Study of Mobile Antennas in Multipath Propagation Environments

The explosive growth of the information transmission in wireless communications has created a revolution in antenna designs, represented by diversity antenna and MIMO system. This chapter will discuss these antennas or antenna systems in wireless communication environment.

5.1 Fading

In practical mobile communication systems, there may be no line-of-sight (LOS) path between the transmitter and receiver. The signal between base station and mobile station (MS) probably will be blocked by buildings, moving vehicles and so on. Multipath arises due to scattering, reflection and diffraction, which results rapid variation in received amplitude over distances as short as $\lambda/2$. If the MS is moving, or if some of the scatterers are moving, these variations may occur over relatively short time intervals. This kind of effect is defined as fading, which is one of the most significant factors affecting the performance of mobile phones. Apart from large amplitude variation, fading can also cause frequency modulation due to Doppler effects, and variable signal delays by virtue of time-varying propagation paths.
However, it is multipath itself that make mobile communication possible at the absent of LOS. While various diversity strategies are developed to combat multipath fading, MIMO systems, on the contrary, exploit multipath due to the fact that the separablility of the MIMO channel relies on the presence of rich multipath [39]. In the following sections, diversity antenna and MIMO antenna will be discussed separately.

5.1.1 Large-scale Fading

Large-scale fading is affected by prominent terrain contours between transmitter and receiver. Its statistics provide a way of estimating the path loss as a function of distance. Sometimes large-scale fading is also referred as local mean or lognormal fading.
The mean path loss is given by

$$\bar{L}_p(d)[dB] = L_s(d_0)[dB] + 10n\log(\frac{d}{d_0}) \qquad (5.1)$$

where $L_s(d_0) = (\frac{4\pi d_0}{\lambda})^2$, with d_0 as reference distance; and n is path loss exponent, which depends on the frequency, antenna height, and propagation environment. $d_0 = 1km$ for macrocells, 100 m for microcells and 1 m for indoor channel. $n = 2$ for free space, 3~4 for urban environments.

Fig.5.1 shows mean path loss versus distance with various n. Note that if distance is logarithmically plotted, the mean path loss will be a straight line with slope of $10n$ dB/decade. That's why large-scale fading is also called lognormal fading.

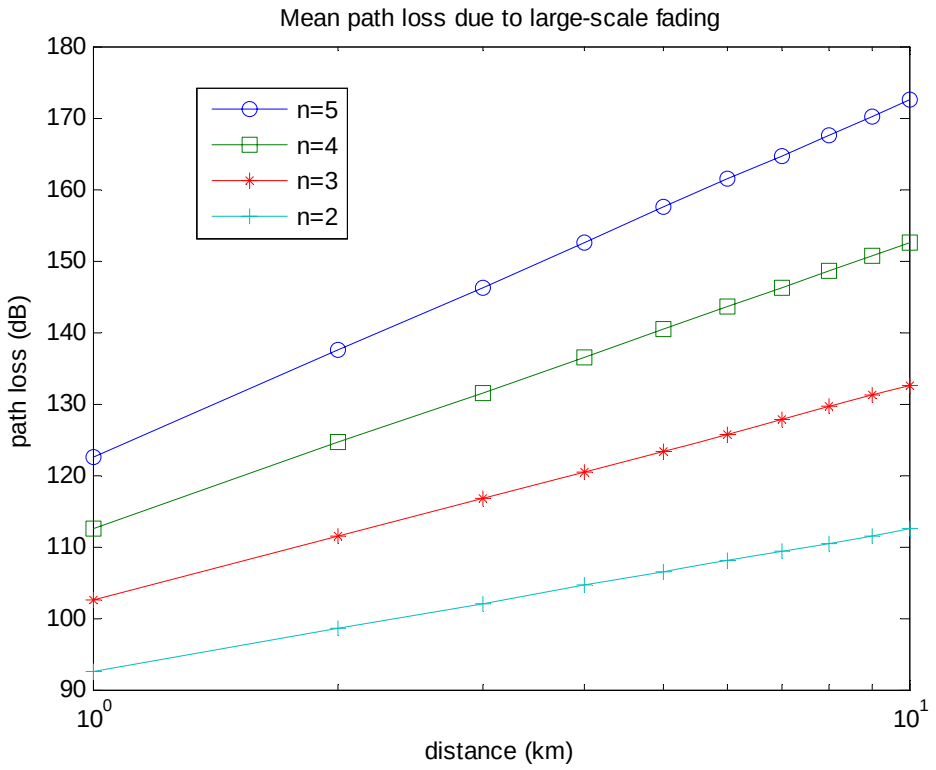

Figure 5.1: Mean path loss vs. distance.

5.1.2 Small-scale Fading

Small-scale fading refers to the dramatic changes in signal amplitude and phase over small spatial interval. Note that usually the terminology of "fading" is referred to this small-scale fading (especially in the fields of diversity or MIMO antennas), while large-scale fading is regarded as its spatial average (over 10 to 30 λ), as shown in Fig.5.2. Later on, without specification, the term fading in this chapter means small-scale fading.

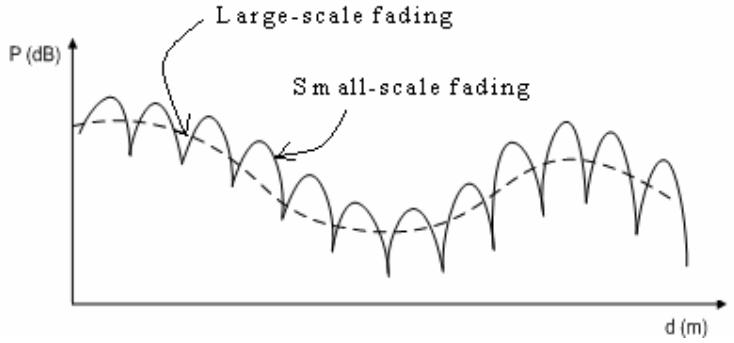

Figure 5.2: large and small-scale fading over small spatial interval.

There are several types of fading in reality, depending on whether the signal bandwidth is greater or lesser than the channel bandwidth (see Fig.5.3), and whether Doppler shift is appreciable. The most common type of fading is flat fading, defined as the case for which Doppler effects are negligible and the signal bandwidth is less than the channel bandwidth, which means that the transfer function of the propagation channel has a constant amplitude and a linear phase variation versus frequency over the bandwidth of the signal. Note that the famous Rayleigh probability distribution function is the statistics of the received signal amplitude in the case of flat fading without LOS; when there is a dominant non-fading signal, such as LOS, the statistical envelope of the received signal is determined by Rician distribution [40] [41].

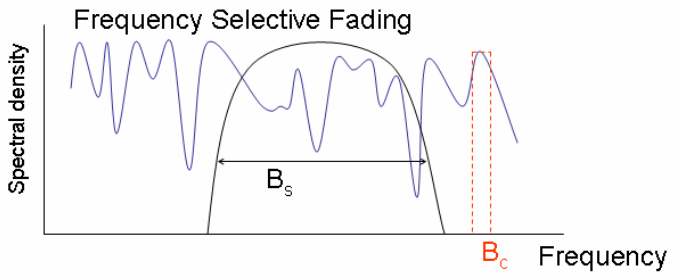

(a)

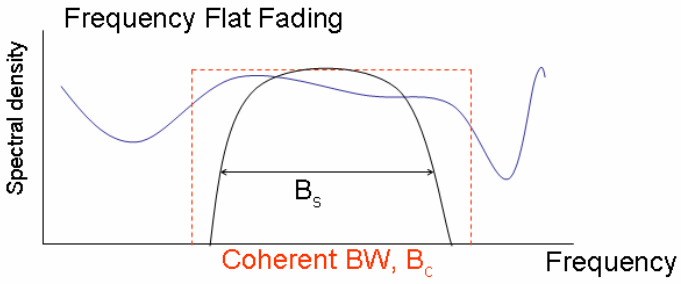

(b)

Figure 5.3: Fading: (a) frequency selective fading when signal bandwidth is larger than channel bandwidth; (b) frequency flat fading when signal bandwidth is smaller than channel bandwidth.

5.2 Diversity Techniques

Diversity is one of the most effective ways to combat deep fades. There are three most important and widely used diversity technologies: frequency diversity, time diversity and antenna diversity [42]. Without specification, the term diversity in this chapter means antenna diversity.

Diversity antenna involves two or more antenna elements to receive signal simultaneously, which is equivalent to provide the receiver with multiple replicas of the same information bearing signal. Provided the correlation between antenna elements is negligible, and denote the outage probability (the probability that instantaneous SNR is below receiver threshold) in one branch as p_e, and antenna branch number as L, then the outage probability of the receiver is p_e^L, which will be considerably small.

5.2.1 Diversity Combining Technologies

There are three most often used methods for combing the different diversity branches at the receiver: maximal ratio combing (MRC), equal gain combing (EGC) and selective combing (SC) [41]. Generally speaking, MRC provides the best performance at the cost of complexity; the performance of SC is the lowest, but it is the simplest way to achieve; and the performance of EGC is in between them. Later on, it will be shown that the performance improvement of MRC, compared with SC, is insignificant. In the following sections, it will shown that the maximum apparent diversity gain [43] for a two-branch diversity antenna is 10 dB for SC, and 12 dB for MRC.

5.2.1.1 Selective Combining

In an ideal selective combing modulator, the branch with the highest SNR is always chosen for the system output. Assume that there are L diversity branches, instantaneous SNR in each of them is denoted as r_i $(i = 1, 2, ..., L)$ with threshold SNR= r and average SNR of received signal in a branch equal to Γ. If the braches experience independent fading (without correlation), the outage probability is given by

$$P\{r_i \le r\} = P_L(r) = [1 - \exp(-r/\Gamma)]^L \qquad (5.2)$$

which is also the cumulative distribution function (CDF) of the output of the selective combing modulator, as shown in Fig.5.4.

Fig.5.4 shows that the largest diversity gain is obtained from L=1 (one branch) to L=2 (two branches); then when the number of antenna elements increases, the increases in diversity gains become trivial.

The apparent diversity gain for a two-branch diversity antenna is obtained simply by combining the signals on the two branches and comparing the combined signal with the signal on one of the branch, i.e., the reference branch [43]. Provided that the correlation between the two branches is negligible, the apparent diversity gain for a two-branch diversity antenna using SC technique is 10 dB (referred to 1% outage probability level). When correlation between the two branches become significant, the apparent diversity gain is expressed as

$$G_{app} = G_{div,\max} e_\rho \qquad (5.3)$$

where $G_{div,\max}$ is maximum achievable diversity gain when there is no correlation between braches, and e_ρ is correlation efficiency, approximately given by [44]

$$e_\rho = \sqrt{1 - 0.99\rho^2} \qquad (5.4)$$

with ρ denoting correlation.

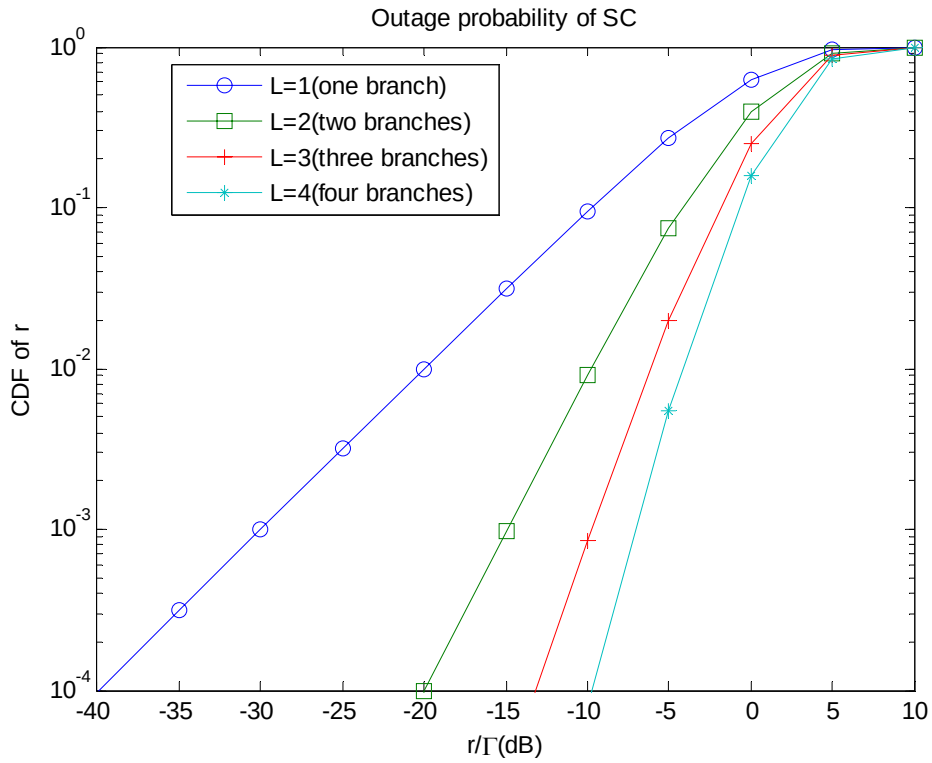

Figure 5.4: Outage probability of SC

5.2.1.2 Maximal Ratio Combining

In maximum ratio combining, the branch signals are weighted and combined so as to yield in the highest instantaneous SNR possible with any linear combining technique. The CDF of the MRC output is given by

$$P_L(r) = 1 - \exp(-r/\Gamma)\sum_{k=1}^{L}\frac{(r/\Gamma)^{k-1}}{(k-1)!} \qquad (5.5)$$

Fig. 5.5 shows the outage probability when using MRC. It is shown that the maximum apparent diversity gain for a two-branch diversity antenna is 12 dB using MRC. Compared with $G_{app,\max}$ by using SC, MRC provides a 2 dB improvement. However, MRC involves continuously adapting each weight of branches differently, which adds the complexity for the diversity combining modulator.

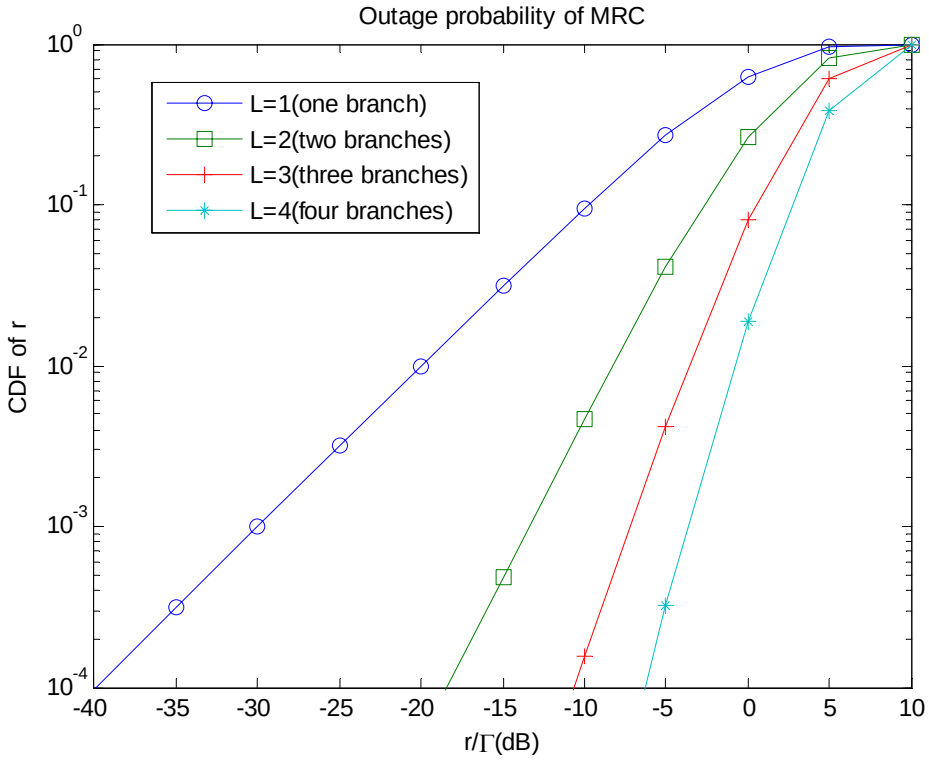

Figure 5.5: Outage probability of MRC

5.2.1.3 Equal Gain Combining

If each branch weight is set to unity and co-phased, MRC becomes equal gain combining. Thus, EGC is a special case of MRC. Without continuously adapting each weight of branches differently, EGC allows receiver to exploit received signals

simultaneously. Therefore, it is quite useful for modulation techniques having equal energy symbols, such as M-PSK [41].
The CDF of the output of EGC can not be obtained in closed form when the number of branches is larger than 2. Nevertheless, from the definitions, it is clear that EGC has slightly lower performance than MRC, but slightly higher performance than SC.

5.2.2 Diversity Antenna

The first diversity antenna is used for base station in 1965. It proves that fading reduction could be achieved by placing two antennas approximately ten wavelengths apart in the horizontal plane. It was shown that the received level at a probability of 1% with the diversity antenna is larger than 8 dB than that with a single antenna [42]. The achievements are more or less like the ones shown in Fig.8 and 9, depending on how much antenna elements are used. As a result, the transmitting power of the mobile station is reduced, and the quality of the transmission is enhanced, which is a great advantage from the total-system point of view. Reception diversity in the base station has been in commercial use in AMPS since 1982.
Antenna diversity can be achieved by spatial, polarization, or pattern diversity. Due to the dimension limit in mobile handset, it is unlikely to achieve polarization or pattern diversity for the antenna in a mobile phone. Spatial diversity seems the only solution for mobile handset antenna, however, limited space in a handset make it difficult to achieve perfect spatial diversity. Right now there is no diversity antenna in a GSM mobile phone. (Usually, there are two antennas in a GSM phone. One is triple or quad-band antenna, probably a PIFA, for different operating frequency bands, the other is for Bluetooth.)
To combat multipath fading, an AMPS user has to talk slowly; GSM use error correction, interleaving, and fade margins in cell planning. There might be diversity antenna in a 3G or 4G mobile phone to achieve high data rate.
This chapter will only focus on spatial diversity in the following sections. And effective and Apparent Diversity of Two Parallel Dipoles are discussed as an example.

Apparent diversity gain has been introduced before. The effective diversity gain of a two-branch diversity antenna is defined as the diversity gain multiplied by the radiation efficiency of the antenna element that is used as reference for the diversity gain [43]-[46]. For a diversity antenna element, the radiation efficiency should be calculated when all the other elements are present, and terminated with loads representing source impedance on their ports.
For simplicity, two parallel dipoles are used here as a diversity antenna [25] [43]. Fig.5.6 shows it and its equivalent circuits.

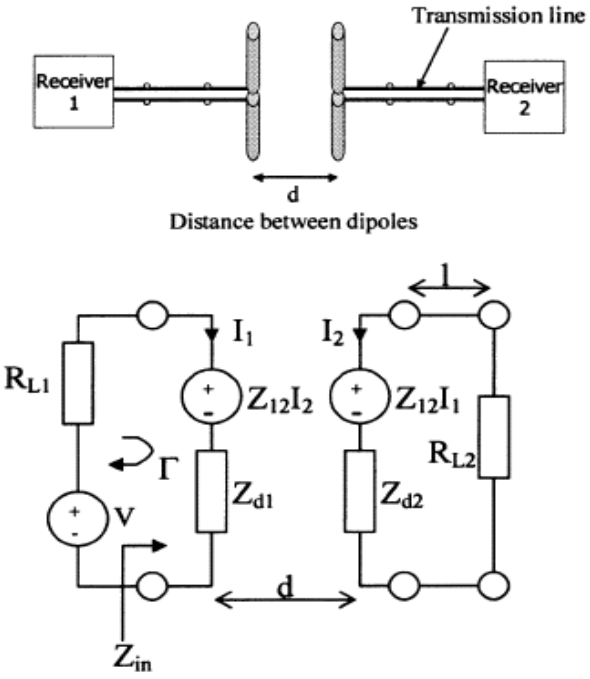

Figure 5.6: Parallel dipoles and their equivalent circuit [43]

Assuming two identical thin dipoles with radius of 0.005λ, so that the current on the dipole is approximately sinusoidal, and that their self and mutual impedances are the same, namely $Z_{d1} = Z_{d2} = Z_d$, and $Z_{12} = Z_{21}$.

Self-impedance Z_d is calculated and plotted (versus dipole length) as shown in Fig.5.7.

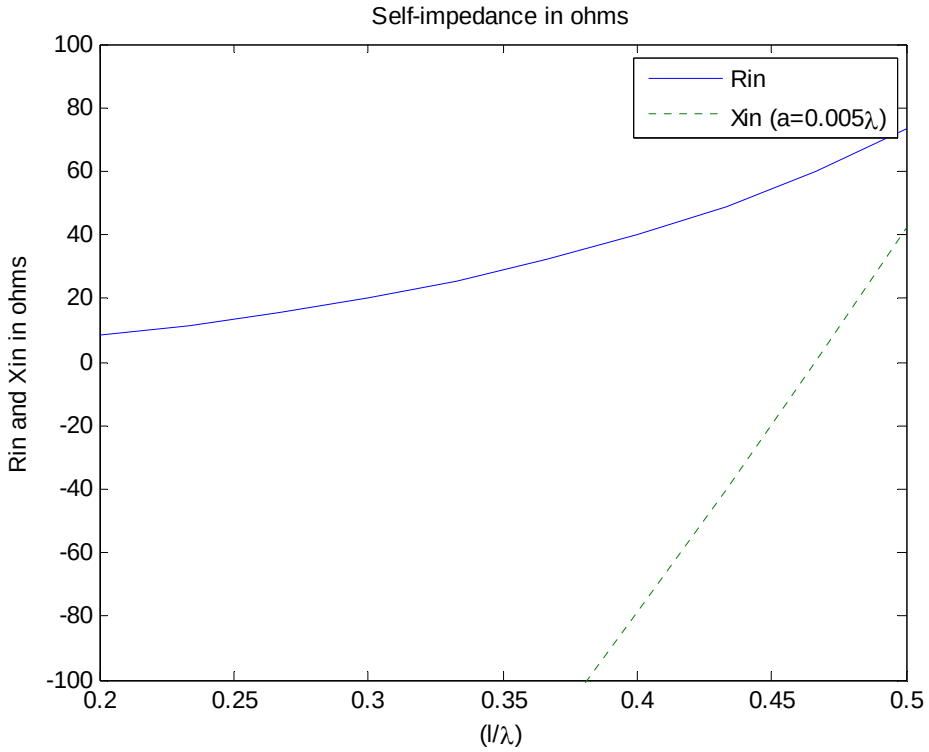

Figure 5.7: Self-impedance (resistance and reactance) of isolated dipole antenna

Z_d of half-wavelength dipole is $73.1 + j42.5$ ohms; when the length of dipole is 0.47λ, the impedance become 60 ohms, as shown in Fig.5.7. This indicates that an isolated resonating dipole should have a length of about 0.47λ instead of $\lambda/2$.
Parallel $\lambda/2$ dipoles are assumed in this chapter. At 900 MHz, the mutual-impedance is calculated and plotted in Fig.5.8. Fig.5.8 shows that the mutual impedance is quite serious when the dipoles are closer than $\lambda/2$.

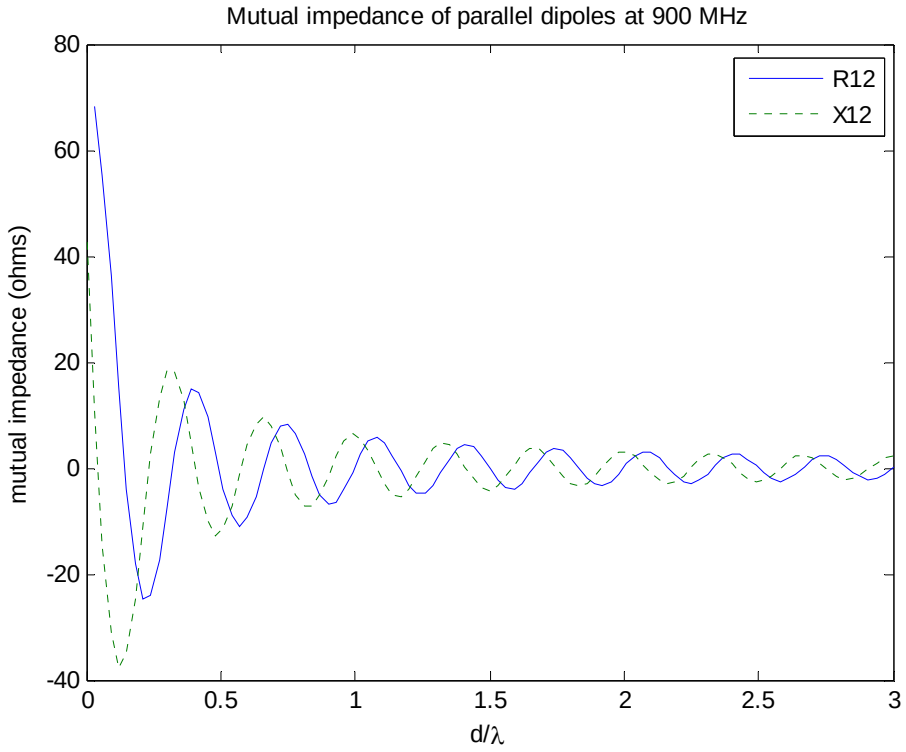

Figure 5.8: Mutual-impedance of two parallel identical dipoles at 900 MHz.

The maximum achievable diversity gain (referred to 1% outage probability) of a two-branch diversity antenna is 10 dB using selective combining, and 12 dB using maximum ratio combining, as shown before. For the convenience of comparison, diversity gains are referred to selective combining at 1% outage probability.

The apparent diversity gain is defined as (5.3) and (5.4), where the correlation coefficient ρ is given by

$$\rho = \frac{\iint_{4\pi} G_{tot}^{1}(G_{tot}^{2})^{*} d\Omega}{[\iint_{4\pi} G_{tot}^{1}(G_{tot}^{1})^{*} d\Omega]\cdot[\iint_{4\pi} G_{tot}^{2}(G_{tot}^{2})^{*} d\Omega]} \tag{5.6}$$

In [47], (5.6) is derived into an expression in terms of S-parameters (5.7), which simplified the numerical calculations and measurements. Moreover, the introduction of this concept makes it easier to design a matching network for a diversity antenna system, where low correlation can still be achieved even if the diversity branches are close to each other.

$$\rho = \frac{|S_{11}^{*}S_{12} + S_{21}^{*}S_{22}|^{2}}{(1-|S_{11}|^{2}-|S_{21}|^{2})(1-|S_{22}|^{2}-|S_{21}|^{2})} \tag{5.7}$$

The effective diversity gain is defined as

$$G_{eff} = G_{app} e_{rad} \tag{5.8}$$

where $e_{rad} = e_{refl} e_{abs}$ is the radiation efficiency, with efficiency due to mismatch e_{refl} and efficiency due to absorption by neighboring antennas e_{abs}.

Theoretically calculations of apparent diversity gain and effective diversity gain are cumbersome. Fortunately, both of them can be easily measured in the reverberation chamber [43]-[46]. As shown in Fig.5.9, the diversity gains measured (at 900 MHz) in reverberation chamber agree well with the theoretical results. From Fig.5.9, it is the degradation of total efficiency rather than that of correlation that reduce the effective gain dramatically when two parallel dipoles are close to each other. Therefore, the matching network introduced in [47] is useless in the system overview of diversity of performance.

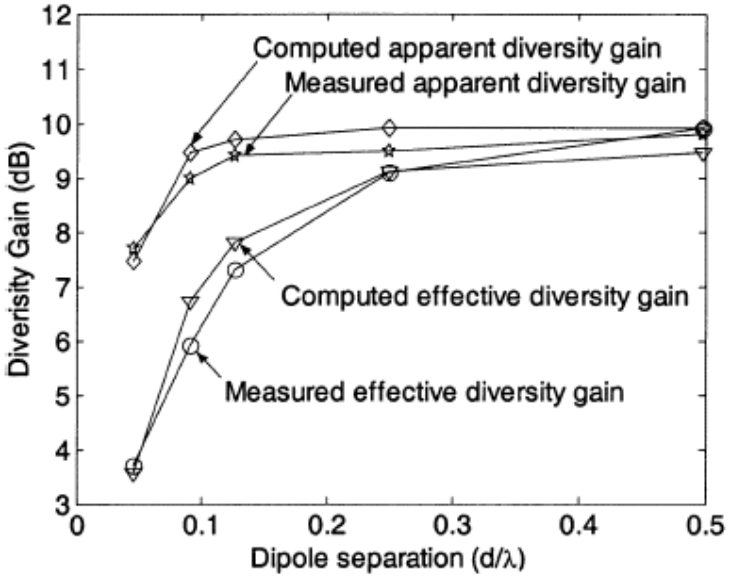

Figure 5.9: Measured and computed apparent and effective diversity gains [43].

5.3 MIMO System

The multiple-input multiple-output (the use of multiple antennas at both the transmitter and receiver sides), popularly know as MIMO, has gained increasing popularity over the past decade due to its communication performance-enhancing capabilities. Previously communications in wireless channels are impaired predominantly by multi-path fading. A key feature of MIMO systems is the ability to turn multi-path propagation, traditionally a pitfall of wireless communication, into a benefit for the user. A core idea in MIMO system is space-time signal processing in

which the natural dimension of digital communication data is complemented with the spatial dimension inherent in the use of multiple spatially distributed antennas. It effectively takes advantage of random fading and when available, multi-path delay spread, for multiplying transfer rates. The prospect of many orders of magnitude improvement in wireless communication performance, at no cost of extra spectrum or transmitted power, is largely responsible for the success of MIMO as a hot topic for new research. [39] [48].

Channel capacity was pioneered by Claude Shannon in the late 1940, using mathematical theory of communication. The capacity of a channel, denoted by C, is the maximum rate at which reliable communication can be performed. Although it is theoretically possibly to communicate at any rate below capacity, it is actually difficult to develop practical channel codes at rates close to capacity. Tremendous progress has been made in code development over the past decades, and practical codes at rates very close to capacity do exist for certain channels, i.e. single-antenna Gaussian channels. However, these codes can not be used for MIMO channels, in that MIMO codes must also utilize the spatial dimension. The capacity limits of MIMO channels provide a benchmark against which performance of space-time codes and general MIMO transmission and reception strategies can be compared. In addition, the study of MIMO channel capacity will give insights into limiting capacity achieving transmission strategies, receiver structures, and codes [48]. SISO, SIMO, MISO and MIMO will be discussed first in this chapter.

5.3.1 Capacity of MIMO System

The single-input, single-output (SISO) system is the conventional system that has been used ever since wireless communication become available. For a given channel with bandwidth of B and transmitter power of P, the signal at the receiver has an average signal-to-noise ratio of SNR_0. An estimation of the Shannon limitation on channel capacity is

$$C \approx B\log_2(1+SNR_0) \qquad (5.9a)$$

Or more commonly in MIMO papers, it is expressed as [39]

$$C = \log_2(1+\rho|h|^2) \qquad (5.9b)$$

where h is the mormalized complex gain of a fixed wireless channel, or that of a particular realization of a random channel, and ρ is the signal to noise ratio at any receive (RX) antenna.

A single-input, multiple-output (SIMO) system has a number of N antennas at the receiver side. If the signals received on these antennas have approximately the same

amplitude, then they can be added coherently to produce an increase by a factor of N^2 in the signal power level. On the other had, there are N sets of noise that are added incoherently and result in an increase by a factor of N in the noise power level. Therefore, there is an overall increase in SNR by a factor of N. The channel capacity for this system is given by

$$C \approx B\log_2(1+N\cdot SNR_0) \qquad (5.10a)$$

As more RX antennas are deployed, the statistics of capacity improve, another expression for SIMO system capacity is given by [39],

$$C = \log_2(1+\rho\sum_{i=1}^{N}|h_i|^2) \qquad (5.10b)$$

where h_i is the gain for the i th RX antenna.

In a multiple-input, single-output (MISO) system, there are a number of M transmitting antennas. The total transmitted power is the summation of the M transmitter branches. A common expression for the capacity of MISO system is given by [39],

$$C = \log_2(1+\frac{\rho}{M}\sum_{i=1}^{M}|h_i|^2) \qquad (5.11)$$

Where the normalization by M ensures a fixed total transmitted power and shows the absence of the array gain in that case, compared with (5.10b), in which the channel energy can be combined coherently.

Assume that the signals transmitted by each antenna are uncorrelated, and that the number of antennas at the receiver side is no smaller than that at the transmitter side, namely, $N \geq M$. In this arrangement, all the transmitted signals can be decoded at the receiver. The big idea in MIMO is that different signals can be sent using the same signal bandwidth, and still be decoded correctly at the receiver. It is equivalent to that each transmitter has one channel. The capacity of each one of these channels is roughly equal to

$$C_0 \approx B\log_2(1+\frac{N}{M}\cdot SNR_0) \qquad (5.12)$$

Since there are M of these channel (as there are M transmitter), the total capacity of the MIMO system is given by

$$C \approx M\cdot B\log_2(1+\frac{N}{M}\cdot SNR_0) \qquad (5.13a)$$

Again a more common expression is given by [39],

$$C = \log_2[\det(I_N+\frac{\rho}{M}HH^*)] \qquad (5.13b)$$

where H denotes the $N \times M$ channel matrix (5.14). Note (5.13b) is based on M equal power uncorrelated sources.

$$H = \begin{bmatrix} h_{11} & h_{12} & .. & h_{1M} \\ h_{21} & h_{22} & .. & h_{2M} \\ . & . & & . \\ . & . & & . \\ h_{N1} & h_{N2} & .. & h_{NM} \end{bmatrix} \qquad (5.14)$$

A system transmitting the signal vector of $x = [x_1, x_2, ..., x_M]^T$, where x_i is the signal transmitted from the k^{th} antenna element at the transmitter side. A signal vector of $y = [y_1, y_2, ..., y_N]^T$ is received at the receiver side, where y_j is the signal received by the j^{th} antenna element at the receiver side. The relation expression of x and y is given by,

$$y = H \cdot x + n \qquad (5.15)$$

where n is the noise vector. The channel matrix H in the MIMO system capacity is the mathematical representation of the physical transmission path, which includes not only the multipath channel characteristics of the physical environment but also the antenna configurations. Therefore, the multipath channel characteristic and the antenna configurations play a key role in determining the communication performance in a MIMO system. The channel matrix H can be evaluated by measurement and modeling in a propagation environment [39] [52], or can be evaluated by using a commercial software package, e.g. Wireless Insite, based on ray tracing method [53], which has emerged as the most popular technique for analyzing the physical environment.

Fig.5.10 shows the comparison of SISO and different MIMO systems capacities. Note that flat Rayleigh fading and zero correlation between all channel transmission coefficients are assumed here. In reality, due to anisotropic antenna pattern and correlations between different channels, the capacities achieved must be smaller than those shown in Fig.5.10.

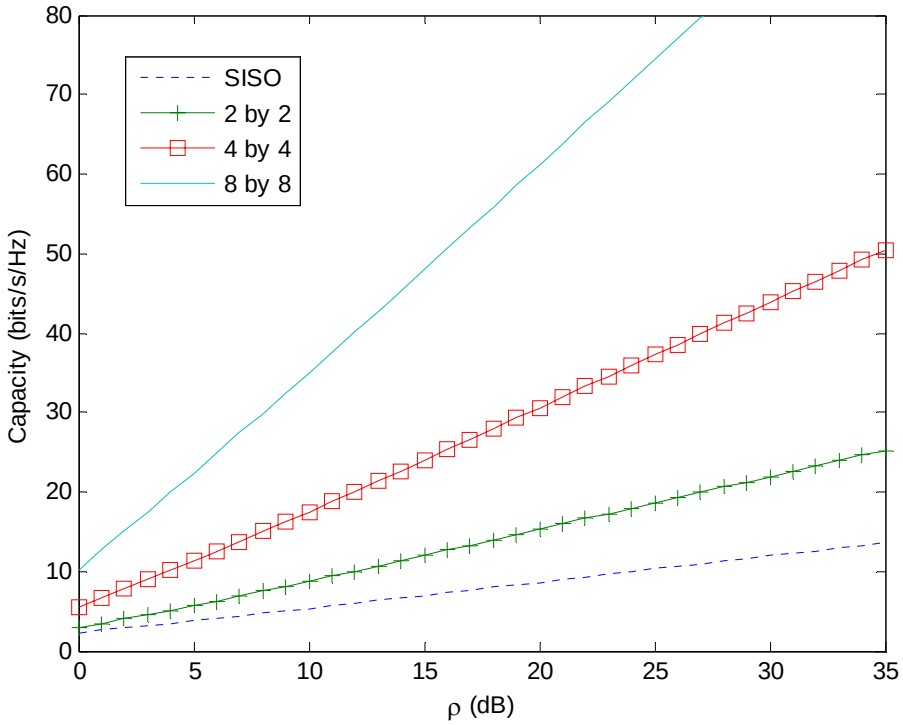

Figure 5.10: Comparison of SISO and different MIMO configuration capacities.

The motivation of using MIMO system is the possibility to achieve orthogonal sub-channels between transmitters and receivers through a rich scattering environment, and consequently to increase the offered capacity. It is seen from (5.13b) that the capacity of the MIMO system is linearly increasing with respect to the number of transmitting antennas. It is more beneficial to transmit data using many different low power channels than using one single, high power channel.

5.3.2 Implementation of MIMO System

There is currently little commercial implementation of MIMO in cellular systems as yet and none is currently being deployed for 3G system, except from pure transmit diversity solution for MISO, which technically belongs to diversity technology. Antenna element numbers and inter-element spacing are key parameters, especially the latter, in MIMO system. An inter-element spacing of around 10λ is required for base stations, in that base stations are usually mounted on elevated positions where the presence of local scatterers to decorrelate the fading cannot be always guaranteed. For terminals, however, $\lambda/2$ spacing is sufficient to ensure a fair amount of uncorrelated fading, because the terminals are presented among local scatterers already, and that there is usually no LOS path. It is shown in [47] that with proper matching network, two parallel dipoles can be put as close as $\lambda/10$ without correlation degradation. However, it is pointed out in [49] that the performance of

compact antenna arrays is strongly influenced by a reduced efficiency, rather than by the correlation of the received signals. In most papers on MIMO, antennas are usually modeled as isotropic radiators, or even neglected in MIMO system simulations. In reality, however, antennas do modify the transmission channel in reality [50]. There are some papers that take antennas into account e.g. [51]. It is expected someone with strong background in both antennas and MIMO signal processing can design better MIMO systems.

5.4 Small Antenna on Mobile Terminals

Mobile terminal market has been growing rapidly for the last decades. One of the trends in mobile terminal technology is to reduce the size of the antennas in mobile terminals. However, due to fundamental dimension limits of antennas [54], a reduction of antenna dimension usually degrades the gain, radiation pattern and bandwidth and the antenna. Small size, low profile, light weight and robustness are the common characteristics needed to be taken into account during antenna designs. Nowadays, PIFA probably is the most popular antenna type in mobile terminals. Different antennas are mentioned briefly in chapter 4 already. The most of built-in antenna used for mobile phone have been designed in a way that the ground plane is utilized as part of the radiator. However, it is shown in [54] that not all the currents on the ground plane contribute to the antenna radiation; moreover, the antenna degradation is partially due to the ground current. A solution to this is balanced antenna. Here the main effort will be put on a balanced folded dipole antenna used for mobile terminals [55]-[57].

5.4.1 Folded Dipole Antennas for Mobile Terminals

For a PIFA antenna in a mobile phone, the current on the mobile phone ground plane is caused by the excitation of unbalanced feed lines, e.g. coaxial cable, for it. The antenna performance degradation caused by variation of the surface current coupled to the user can be avoided by decreasing the current flow on the ground plane. It has shown that antenna having balanced structure and being fed with a balanced line are effective to mitigate the antenna performance degradation due to the body effect, and also reduce SAR [57] [58].

A folded dipole consists of two parallel dipoles connected at the two ends, forming a loop as shown in Fig.5.11, provided that the spacing between the two parallel dipoles d is much shorter than $\lambda/2$. For the folded dipole with an unbalanced feed line, the currents on the upper wire and the lower wire are unbalanced, but the sum of the currents on the arms is balanced. This makes it a suitable antenna element for MIMO

in mobile terminals, in that the reduction of current on ground plane, introduced by the folded dipole, also reduces the coupling between nearby antenna elements.

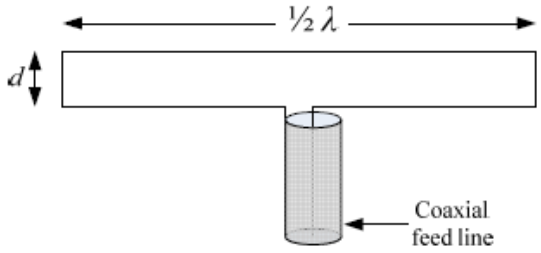

Figure 5.11: $\lambda/2$ folded dipole.

5.4.2 A Dual-band PIFA Antenna for Mobile Phones

In order to compare the ground current of a folded dipole with that of a PIFA antenna, a dual-band PIFA antenna designed by Jani [59] is modeled in CST, and presented here in Fig.5.12.

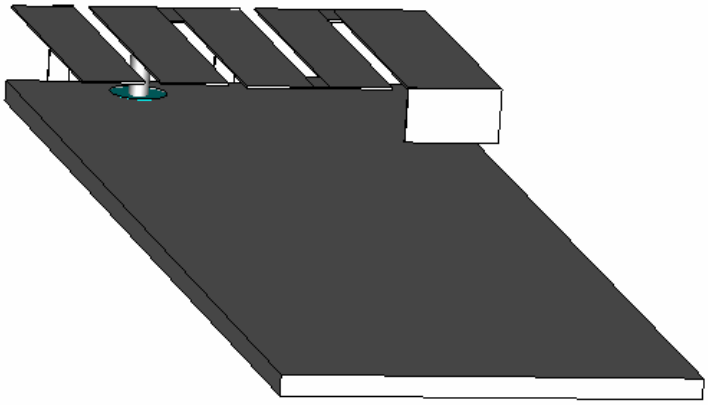

Figure 5.12: A dual-band PIFA antenna with a ground plane size of 40 mm×110 mm.

The upper band patch is divided into two parts to increase the impedance bandwidth [60]. The lower band patch is meandered to reduce its size, and its bandwidth is creased too with a capacitive load. Its return loss is shown in Fig.5.13. Since its radiation patterns are out of our concern, they are omitted here. And its ground current will be shown in the next section with comparison of that of a folded loop antenna.

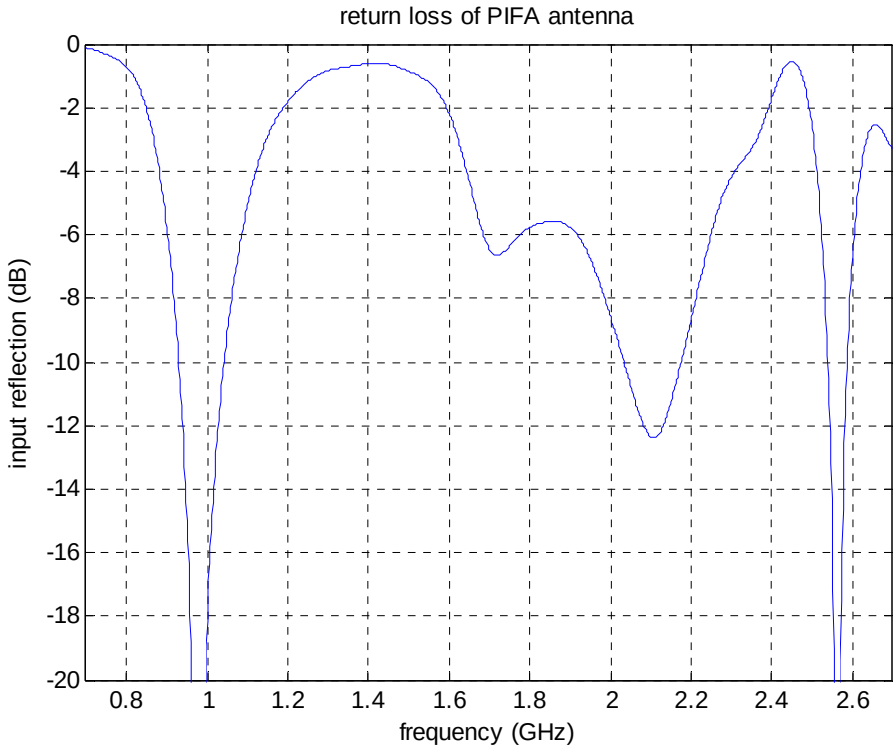

Figure 5.13: Return loss of the dual-band PIFA antenna.

5.4.3 Folded Loop Antenna for Mobile terminals

Even for the upper GSM band (1710-1880MHz), a have-wavelength is too long for a mobile phone. Therefore, the folded dipole antenna presented in section 5.4.1 will be folded again to form a folded loop antenna as shown in Fig.5.14.

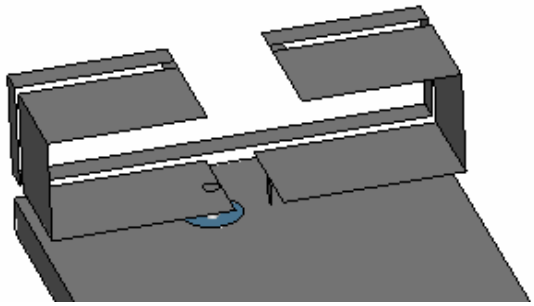

(a)

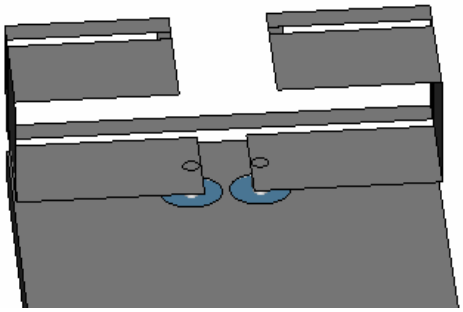

(b)

Figure 5.14: Folded loop antenna: (a) with unbalanced feed; (b) with balanced feed.

Fig.5.15 shows the return loss of the folded loop antenna with unbalanced feed. A folded loop antenna has generally narrow bandwidth. However, by changing the ratio of width of the upper dipole and that of the lower dipole ($w1/w2$), the bandwidth can be increased a lot. It is assumed that for the folded loop antenna with balanced feed, the bandwidth can be increased further by optimizing $w1/w2$. Note that the bandwidth can be increased further for both cases by optimizing their ground plane sizes. But, in order to fairly compare the ground currents of the folded loop and PIFA, the ground plane size is set to 40 mm×110 mm for both of them.

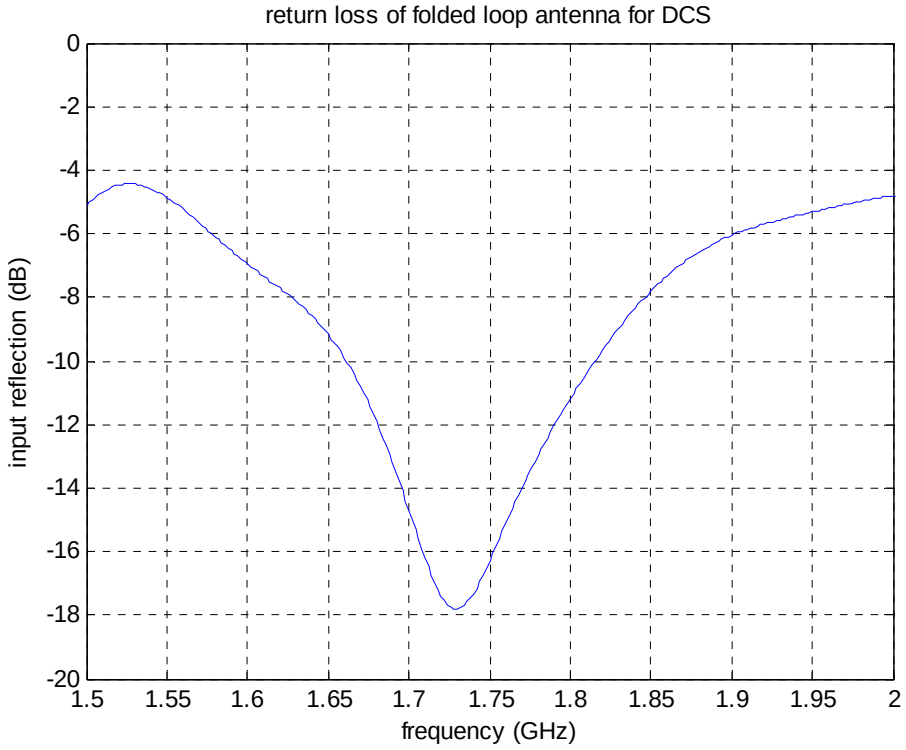

Figure 5.15: Return loss of the folded loop antenna with unbalanced feed.

The ground current for the folded loop with balanced feed is supposed to be smaller than that of the folded loop with unbalanced feed. But a balanced feed needs a balun, which increase the complexity and cost for mobile phones. Hence, the folded loop with unbalanced feed is preferred, and used to compare the ground current with the PIFA, as shown in Fig.5.16. And it is shown in Fig.5.16 that the ground current distribution for a folded loop antenna is smaller than that of the PIFA antenna.

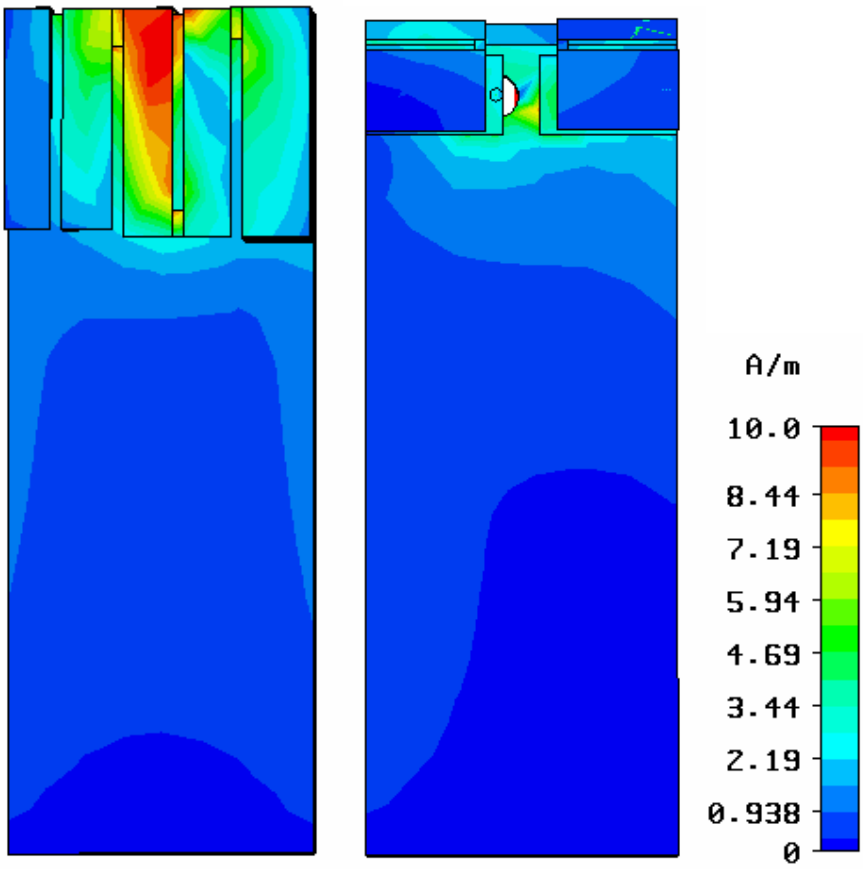

Figure 5.16: Comparison of ground current distributions of a PIFA and folded loop.

The less ground current density of the folded loop antenna may provide a less correlation and better diversity gains when more than one folded loop is incorporated in a mobile terminal. It should be noted that the folded loop antennas are still too large to be used as diversity antenna elements in a real mobile phone. Inserting a low-loss dielectric slab with high dielectric constant into the folded loop will definitely reduce its size, but its bandwidth will also decrease. A more sophisticated study about the possibility of a trade-off should be made to check the possibility of MIMO terminal for mobile phones. Nevertheless, the folded loop antennas should be a promising option for MIMO implementation for other larger mobile terminals e.g. laptops or wireless routers.

Another possibility of using folded loop antenna for diversity uses is to view the two ports in Fig. 5.14 (b) as two diversity branches. Two independent receivers are

connected to each port, and then combined with a diversity combining modulator e.g. selective combining modulator.

The efficiencies of the diversity two-port folded loop antenna are plotted in Fig.5.17. And the apparent and effective diversity gains are plotted in Fig.5.18. Note the diversity gains are calculated based on the assumptions of selective combining and 1% outage possibility. It should be also noted that there is a dip in the diversity gains at around 1.65 GHz shown in Fig.5.18. This is because at this frequency, the folded loop antenna is resonating; the signals received at the two ports are almost the same but a 180 degree phase shift, and therefore, the correlation between the two ports at this single frequency is so strong that there is nothing to gain for diversity combining.

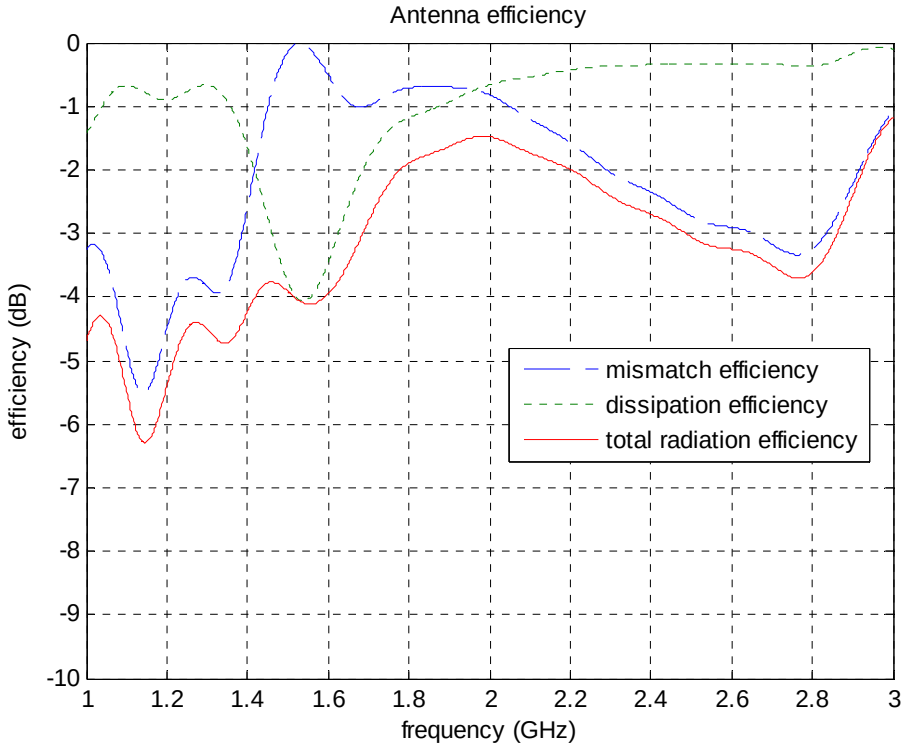

Figure 5.17: Diversity folded loop antenna efficiencies.

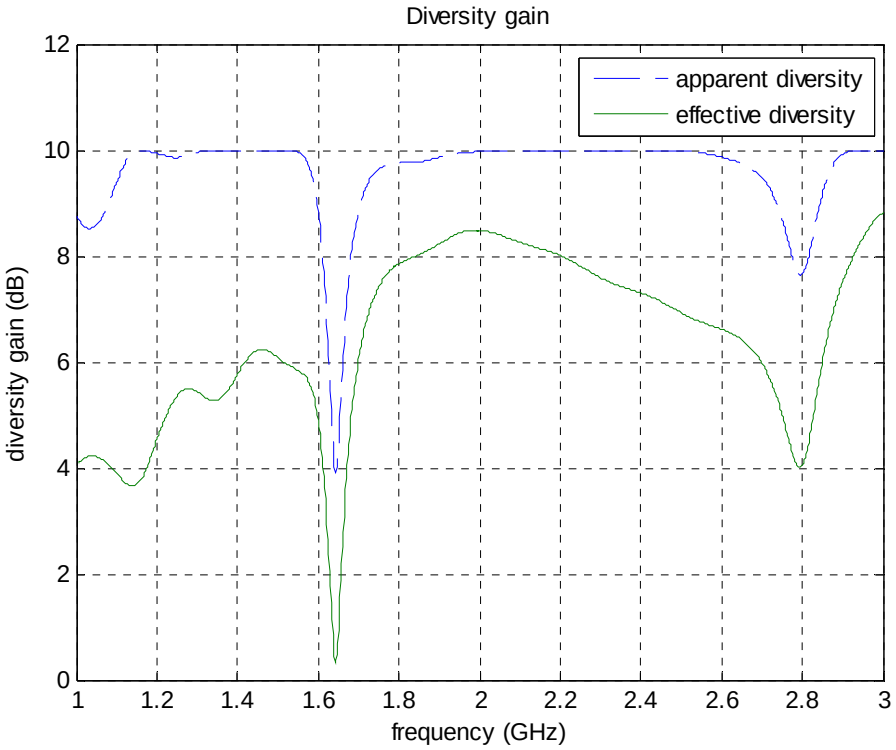

Figure 5.18: Diversity gains of the two-port folded loop antenna.

6. Center Puck of ELEVEN Antenna

As shown in Fig. 1.2, the ELEVEN [2]-[7] antenna is in essence a dual log-periodic folded dipole comb, which can work over decade frequency bandwidth. If coupling between each dipole element is negligible, by cascading infinite dipoles resonating at different frequencies, ELEVEN antenna can have an infinitely large bandwidth in principle. However, in reality, the coupling between several neighboring dipole elements cannot be neglected. Duo to practical manufacture limitation, the dipole elements can not be made infinitely small in the center. Therefore, the operating frequency can not go infinitely high. Further more, more radio telescope applications, the ELEVEN feed has to be put into a Dewar so that it can be cooled to low physical temperature. The Dewar will constrain the size of the ELEVEN feed in a way that it can not be made too large. This makes it impossible to design an ELEVEN antenna that is able to cover really low frequencies. Since the LNA is developed at MC2, Chalmers, the main job at antenna group is to minimize the input reflection of the ELEVEN antenna while maintaining the other antenna characteristics.

Compared with the whole size of the ELEVEN antenna, its center region, or center puck, is a tiny piece (see Fig.6.1). Previously, it is usually neglected in computer-aided antenna design. But the measurement may differ a lot from the simulation without including the center puck. One of the tasks of this thesis work is to model the center puck in CST, and try to improve the return loss introduced by the center puck. In the following sections, different center puck configuration is presented.

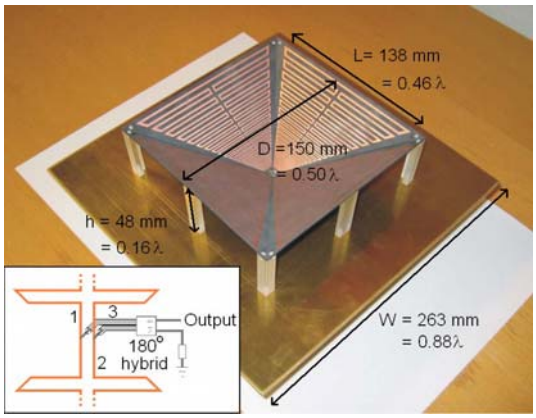

Figure 6.1: Photograph of dual polarization ELEVEN antenna.

6.1 2×1 and 2×2 configurations of center pucks

Actually, all the early designs of ELEVEN antennas are designed with a cross-over center puck. Here M×N configuration is introduced with M denoting the port number

per polarization, and N denoting the number of polarizations. For example, the ELEVEN antenna shown in Fig.6.1 is a 2×2 configuration, in that it has two polarizations and two ports for each polarization. It can be denoted by a simple drawing shown in Fig. 6.2. Fig.6.3 shows a photograph of a 2×1 configuration ELEVEN antenna.

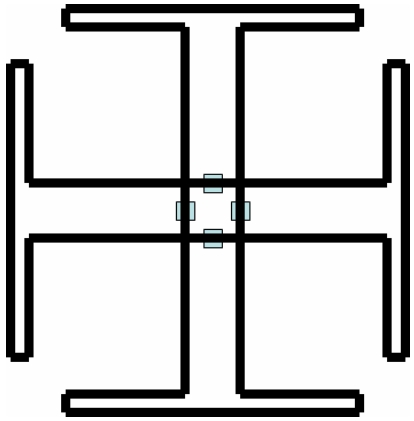

Figure 6.2: Symbol drawing of a 2×2 configuration ELEVEN antenna.

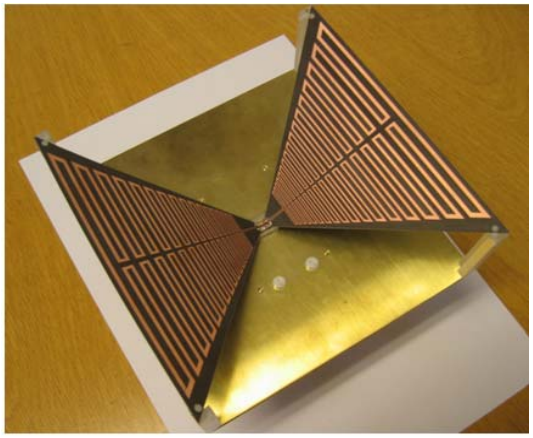

Figure 6.3: Photograph of a 2×1 configuration ELEVEN antenna.

Since the feeding points for the ELEVEN antenna are at the center region, the center puck becomes crucial. By feeding the antenna at high resonating frequency region, the loss is small compared with ATA antenna. However, on the other hand, this configuration requires high accuracy manufacture of the center puck. Moreover, the 2×1 or 2×2 configurations have other serious problems, which will be addressed in the following sections. To overcome the drawbacks of these configurations, 4×2 configuration will be used in the future development of ELEVEN antenna.

6.2 4×1 and 4×2 Configurations of ELEVEN Antennas

The purpose of introducing the 4-port per single polarization (4×2) configuration is to remove the center puck, making it easier for manufacture, applicable for more applications. Note that 4×1 configuration is mainly for tracking applications rather than return loss improvement.

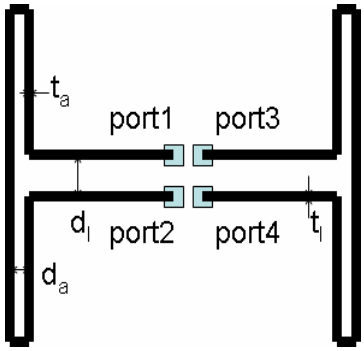

Figure 6.4: Symbol drawing of a 4×1 configuration ELEVEN antenna.

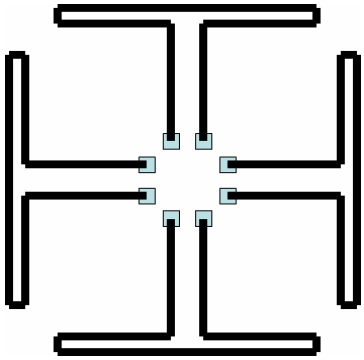

Figure 6.5: Symbol drawing of a 4×2 configuration ELEVEN antenna.

Due to the Master thesis time limitation, the designs of these configuration antennas are out of the scope of this report.

6.3 Center Puck Model

There are several ways to manufacture the ELEVEN antennas. One way is to manufacture the center puck and antenna petals separately, and connect them together. The advantage of this method is that by separating the manufactures of the center puck and antenna petals, the center puck can be made more accurately. The ELEVEN antenna manufactured at Caltech, US, was using this method. However, it is difficult to solder the antenna petals to the center puck properly. Moreover, without realizing the importance of the center puck of the ELEVN antenna, the manufacturer at Caltech made it almost twice in size than it should be. Therefore the one made at Caltech did

not work at all. Another way is etching the two polarization antenna elements at two sides of the same substrate, and the four petal parts of the ELEVEN antenna are bended. In this way, the whole antenna is manufactured on the same piece of plate, and there is no connection problem. But, to manufacture two polarization antennas on two sides of one substrate will degrade the coupling between the two pairs of orthogonal coupled striplines for 2×2 configuration.

6.3.1 Initial 1-13 GHz 2×2 configuration model in 2006

Fig.6.6 (a) shows a CST model of the center puck made for Jet Propulsion Laboratory (JPL), Caltech in 2006. The four lumped resistors representing the four petal antenna impedance, which is 200 ohms approximately. The differential return losses of the center puck are shown in Fig.6.6 (b). The high feed corresponds for the upper parallel striplines; and the low feed corresponds for the lower parallel striplines. The supporting dielectric is polystyrene with dielectric constant of 2.54.

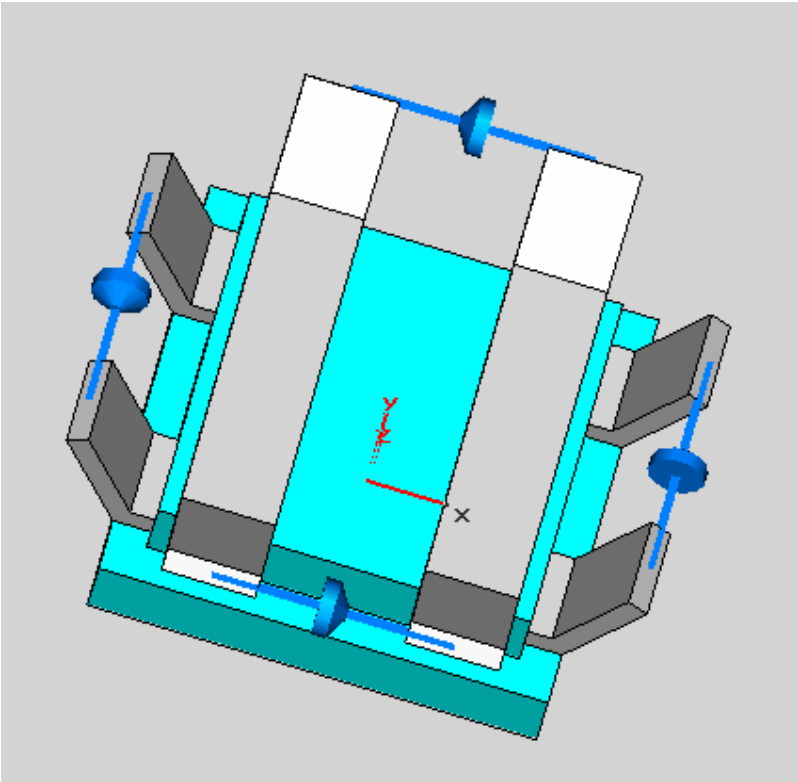

(a)

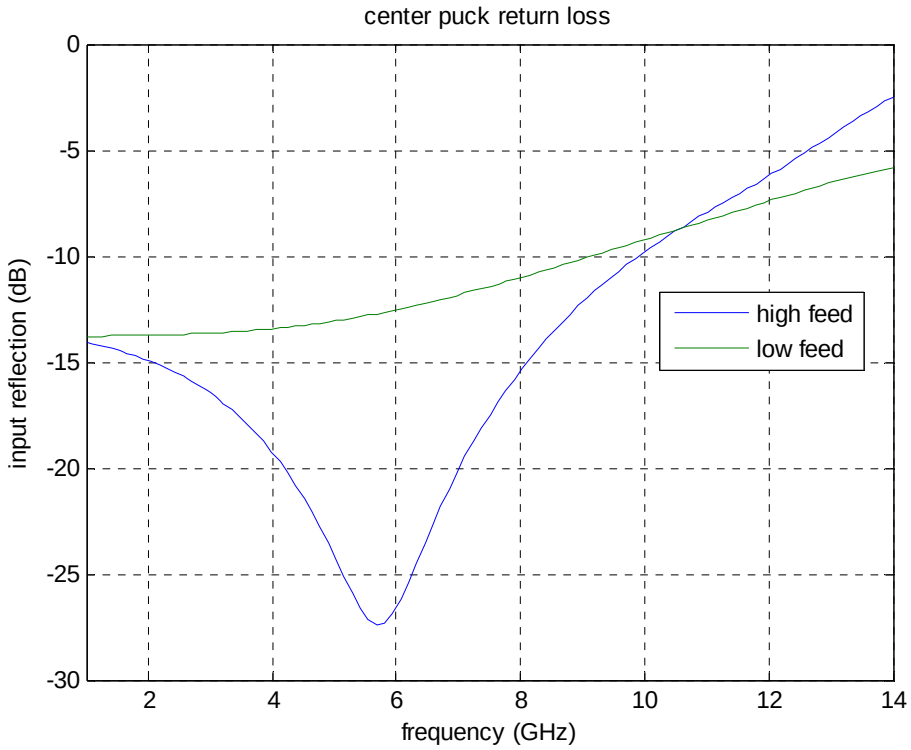

(b)

Figure 6.6: (a) CST model of the initial center puck made at 2006, with dielectric constant of 2.54; (b) Return losses of the initial center puck model.

Each two striplines are differentially terminated, which means that the odd mode dominates. In odd modes, the 200 ohms lumped resistor can be interpreted as two 100 ohms short-circuited resistor [61]. Each stripline is then terminated at two ends by 100 ohms short-circuited resistor. Assume the coupled striplines has an odd characteristic impedance of 100 ohms, it is seen by two 100 ohms parallel resistors from the middle of each stripline. If a 50 ohms coaxial cable is connected to the center of each stripline, the impedance seen by the cable port is approximately still 50 ohms. However, in reality the coupled striplines can not be designed perfectly with an odd characteristic impedance of 200 ohms. Moreover, the coax-to-microstrip junction is a low pass filter [33] [62], which may partially explain why there is a trend of increasing of the return losses. Another reason of the increasing return losses is that the coupling between orthogonal striplines degrades with increasing frequency.

The return losses at high frequency can be improved by simply reducing the width of the striplines. By reducing the stripline width from 1 mm to 0.5 mm, the return losses at high frequencies are improved, as shown in Fig.6.7. From Fig.6.7, it is noticed that the overall return losses at most frequency range does not improve much. One reason is that when reducing the width of the striplines, the odd impedance changed in a way, that the total return losses do not improve much. Actually the return losses can be

further reduced by optimizing all the model parameters (e.g. substrate thickness, dielectric constant, spacing between coupled striplines and stripline thickness) together. And by using this model, the coupling between two orthogonal pair of striplines is not very much. However, as mentioned before, the biggest problem with this model is the manufacture, because it is difficult to solder the center puck with four antenna petals properly. And this method may not work. So efforts will not be put to optimize this model.

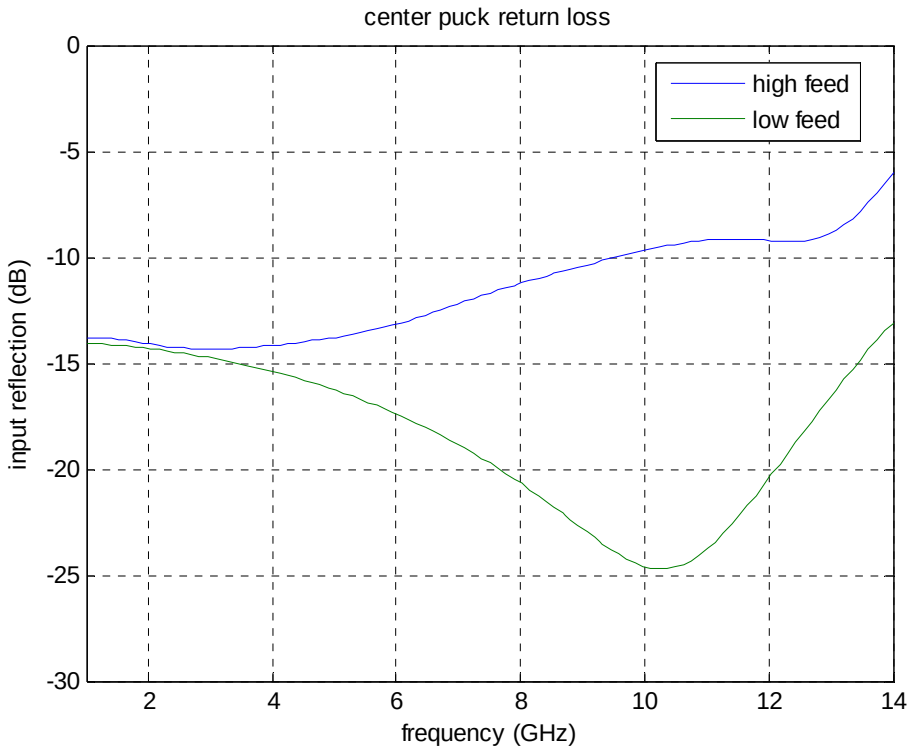

Figure 6.7: Return losses of initial center puck but with narrower striplines.

6.3.2 The second 1-13 GHz 2×2 configuration model made in 2007

The second 2×2 configuration ELEVEN antenna is based on the method of manufacturing the two polarization pairs on two sides of the same substrate (Kapton) with dielectric constant of 3.5. At the center puck of this antenna, the supporting dielectric is polystyrene dielectric constant of 2.54. As mentioned before, there is no connection problem for this antenna. But the distance between the two orthogonal pairs of striplines at the center puck region becomes very small compared with the initial model. The coupling between the two pairs of orthogonal striplines degrades so much that the return losses above 6 GHz become unacceptable. To study this center puck configuration, a circuit model has been built to give some insight into this structure.

Fig.6.8 (a) is a simple circuit model of the center puck that stresses the coupling between the two pairs of orthogonal striplines. In order to illustrate Fig.6.8 (a), a schematic counterpart of it is shown in Fig.6.8 (b). Fig.6.8 (c) is the return loss of this circuit model simulated in ADS. It is seen from Fig.6.8 (c) that the mutual coupling between the orthogonal striplines increased linearly with increasing frequency. That's the reason about the return loss degradation at high frequency.

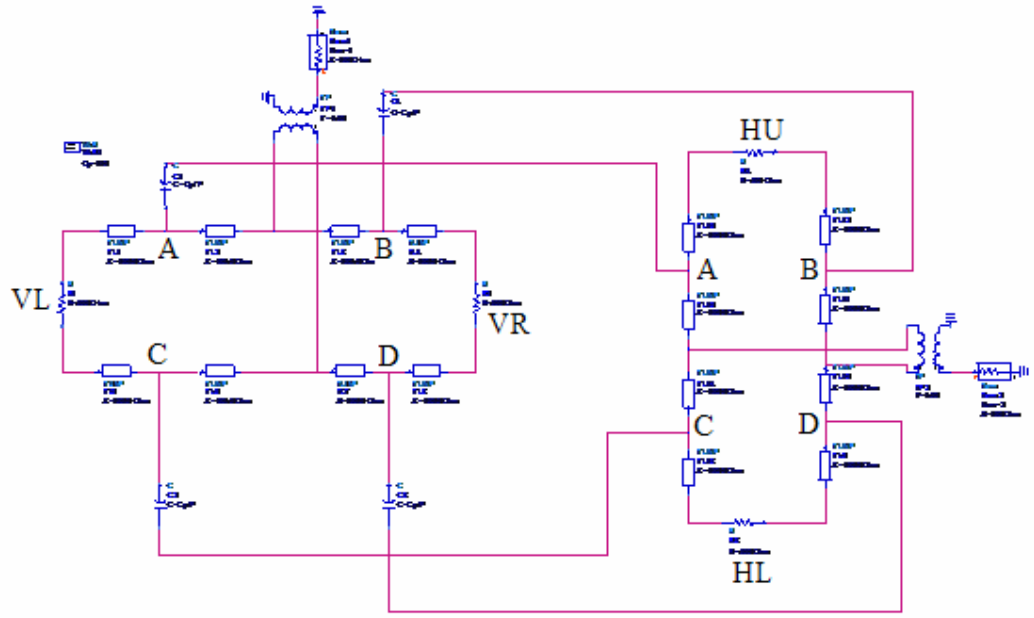

(a)

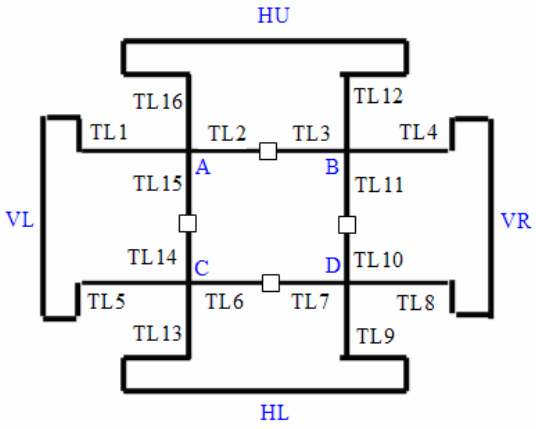

VL: vertical left dipoles
VR: vertical right dipoles
HL: horizontal lower dipoles
HU: horizontal upper dipoles

(b)

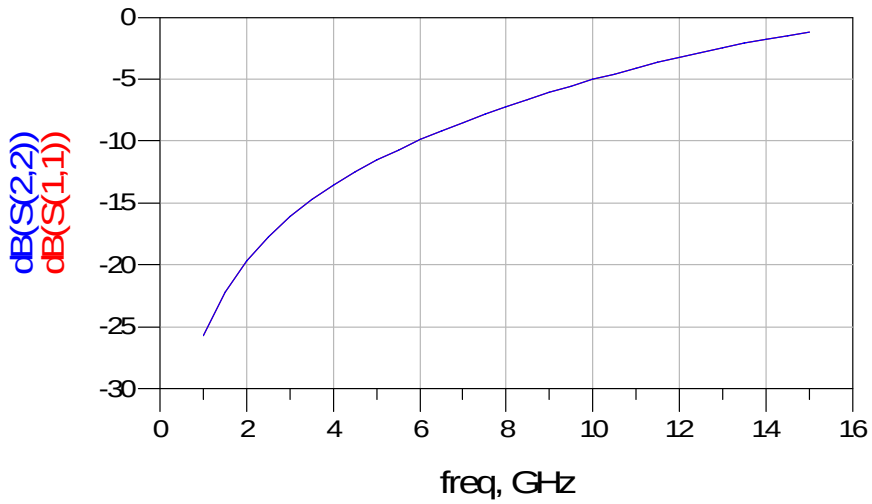

(c)

Figure 6.8: (a) Simple circuit model of the center puck in ADS; (b) Schematic illustration of the simple circuit model; (c) Return losses of the simple circuit model. (Courtesy of Niklas Wadefalk)

This simple model assumes that the mutual coupling between orthogonal striplines can be represented by the capacitance caused by two parallel plate conductors. It neglects other parasitic ground capacitors, stripline inductors and the effect of coax-to-microstrip junction. More rigorous circuit model about the orthogonal coupled striplines [63] [64] are given by Fig. 6.9.

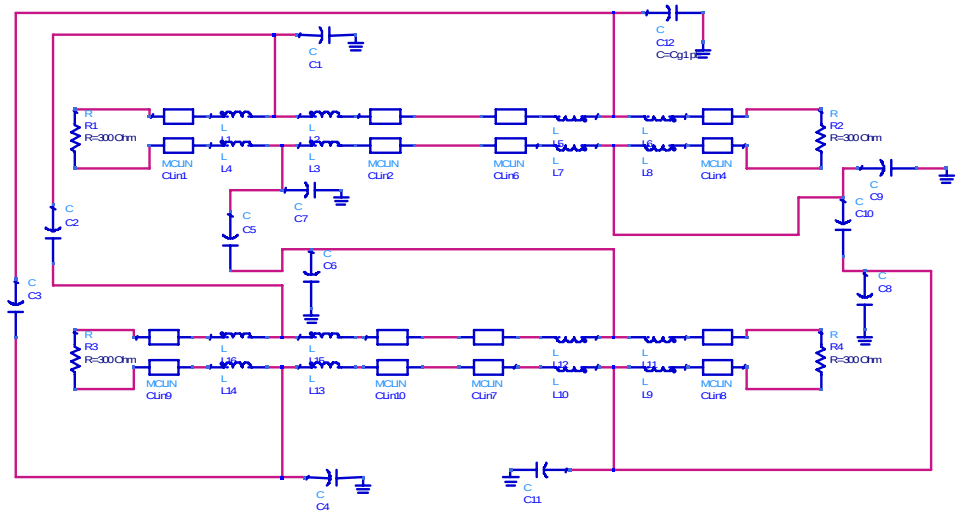

Figure 6.9: Equivalent circuit of four layer coplanar orthogonal coupled strip lines [64].

For microstrip line structure the capacitance per unit length is given by [24],

$$C = 4\varepsilon_r\varepsilon_0(\frac{w}{h} + \frac{2}{\pi}\ln 2) \quad w/h > 3 \tag{6.1a}$$

$$C = 2\pi\varepsilon_r\varepsilon_0[\ln(\frac{8}{\pi}\frac{2h}{w}) + \frac{\pi^2}{48}(\frac{w}{2h})^2] \quad w/h < 3 \tag{6.1b}$$

where h is the substrate thickness and w is the stripline width (the width of upper and lower striplines are the same).

The upper strip affects the electric field distribution between the down strip and the ground plane in a way that the self capacitances of the down striplines decrease. For both striplines in the second 2×2 configuration center puck, the width is much more than the thickness. The effect of the lower striplines on the current distribution of the upper striplines is negligible [63]. Assume that current distribution of the upper strips is uniform; the parasitic inductance can be given by [64],

$$L = \frac{\mu_0}{2\pi} l[\ln(u + \sqrt{u^2+1}) + u\ln(\frac{1}{u} + \sqrt{(\frac{1}{u})^2+1}) + \frac{u^2}{3} + \frac{1}{3u} - \frac{1}{3u}(u+1)^{3/2}] \tag{6.2}$$

where $u = \frac{l}{w}$.

The cross region can be modeled by a plate capacitor with fringing fields. Ideal capacitance of the a parallel plate capacitor is

$$C = \frac{\varepsilon_r\varepsilon_0 w^2}{d} \tag{6.3}$$

where d is the shortest distance between two orthogonal striplines.

Fringing effect is considered by introducing effective stripline width w_{eff}.

$$w_{eff} = \frac{2\pi d}{\ln[\frac{dF}{w} + \sqrt{1+(\frac{2d}{w})^2}]} \tag{6.4}$$

where $F = 6 + (2\pi - 6)\exp[-(\frac{4\pi^2}{3})(\frac{h}{w})^{-\frac{3}{4}}]$.

The mutual capacitance of the cross talk region is given by

$$C_{12} = \frac{w_2}{h_{12}}[\varepsilon_r - \frac{\varepsilon_r - \varepsilon_{eff}}{1+G(\frac{f}{f_p})^2}][w + \frac{w_{eff} - w}{1+(\frac{f}{f_p})^2}] \tag{6.5}$$

where $\varepsilon_{eff} = \frac{\varepsilon_r + 1}{2} + \frac{\varepsilon_r - 1}{2}(1 + \frac{10h}{w})^{-1/2}$, $f_p = \frac{Z_0}{2\mu_0 h}$ and $G = 0.6 + 0.009Z_c$ with Z_c as the characteristic impedance.

However, it must be note that equations (6.1)-(6.5) just give an approximation of the real value in this structure. These values are optimized by comparing with the full wave simulation in [63] [64]. Moreover, the coax-to-microstrip junction effect must be taken into account as shown in Fig.6.10. Note that there is no formula for the parasitic parameter in that model though.

The CST model of the 2×2 configuration center puck is shown in Fig.6.11 (a). The return losses of this model are shown in Fig.6.11 (b). It is shown that the return losses degrade dramatically above 5 GHz. This agrees with the ADS simulation in Fig.6.18 (c). The reason that the ADS simulation shows slightly better return losses is that it did not consider the parasitic inductance and coax-to-microstrip junction effect.

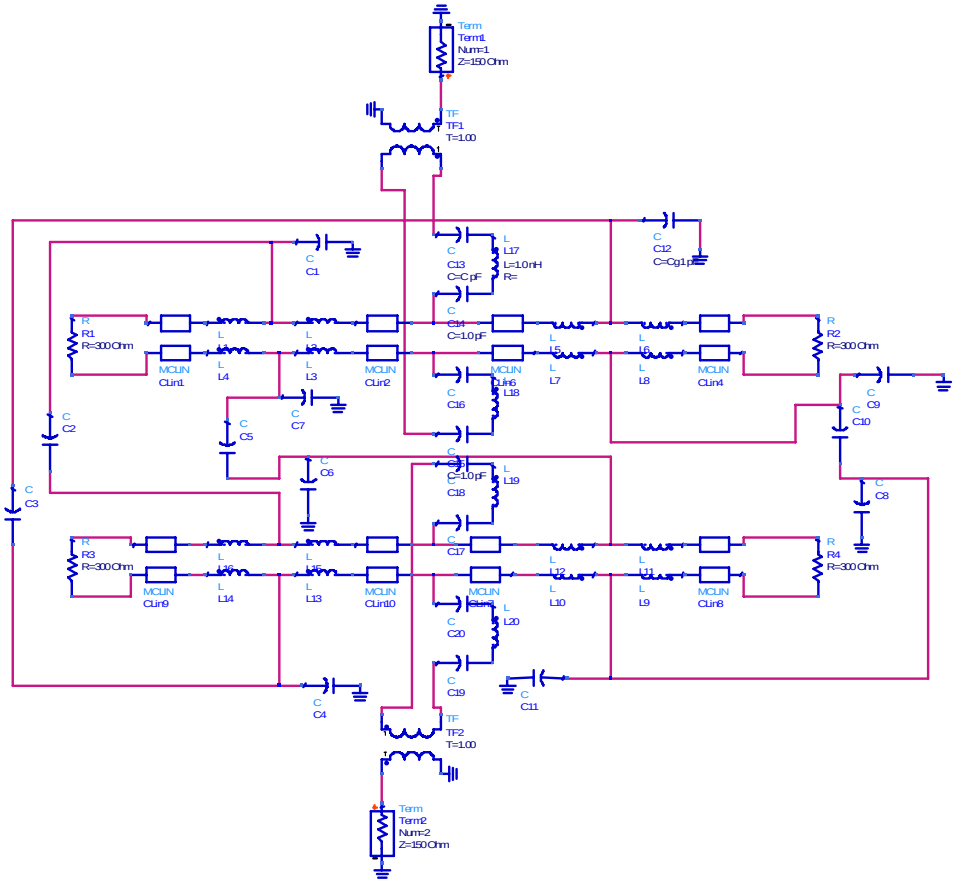

Figure 6.10: Equivalent circuit of 2×2 configuration center puck.

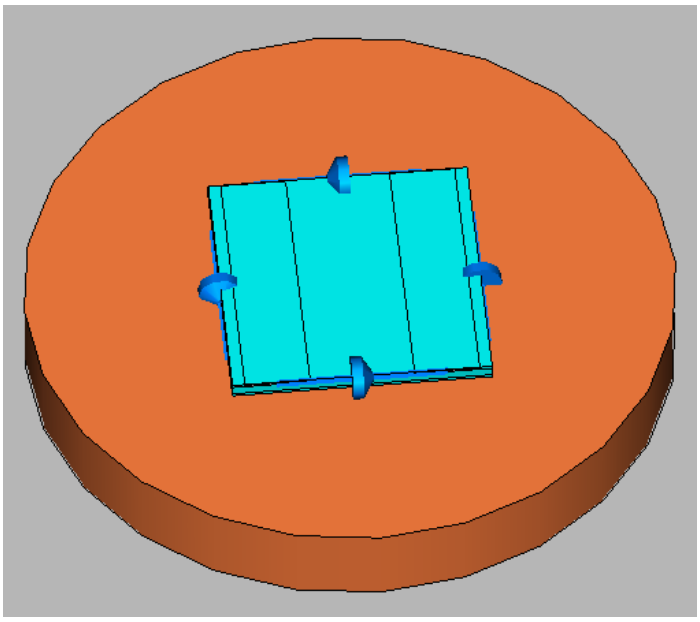

(a)

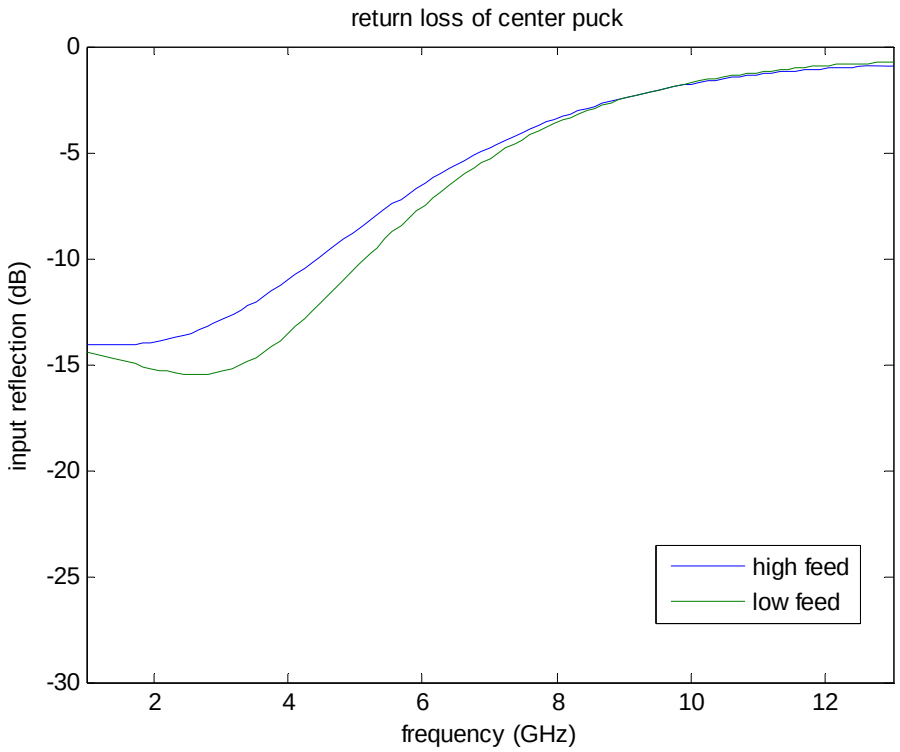

(b)

Figure 6.11: (a) CST model of the second 1-13 GHz 2×2 configuration center puck with striplines manufactured on Kapton ($\varepsilon_r = 3.5$) and supporting dielectric of polystyrene ($\varepsilon_r = 2.54$); (b) Return losses of it.

In order to prove that this degradation is mainly due to the mutual coupling between the two pairs of coupled striplines, only a single pair of coupled striplines is modeled as shown in Fig.6.12. The return loss of the single polarization (2×1 configuration) of the second 2×2 configuration center puck is shown in Fig. 6.12 (b), from which it is shown the overall return loss of this model is below -13 dB.

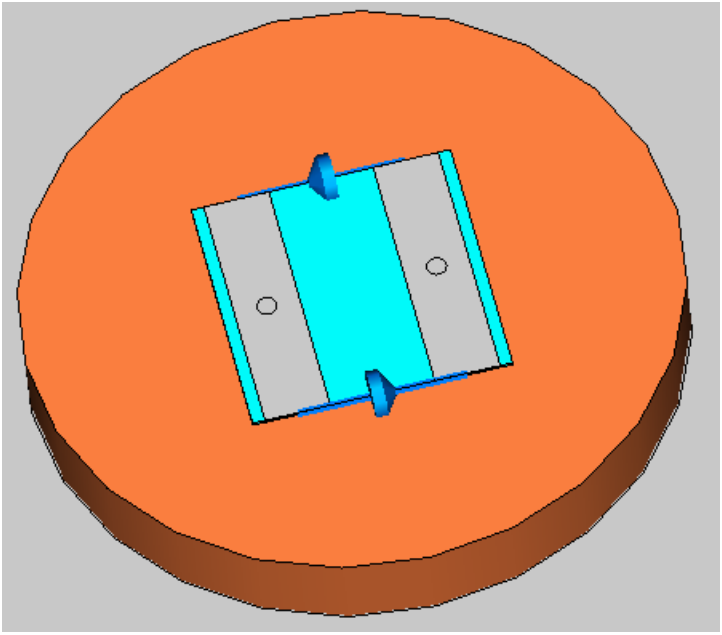

(a)

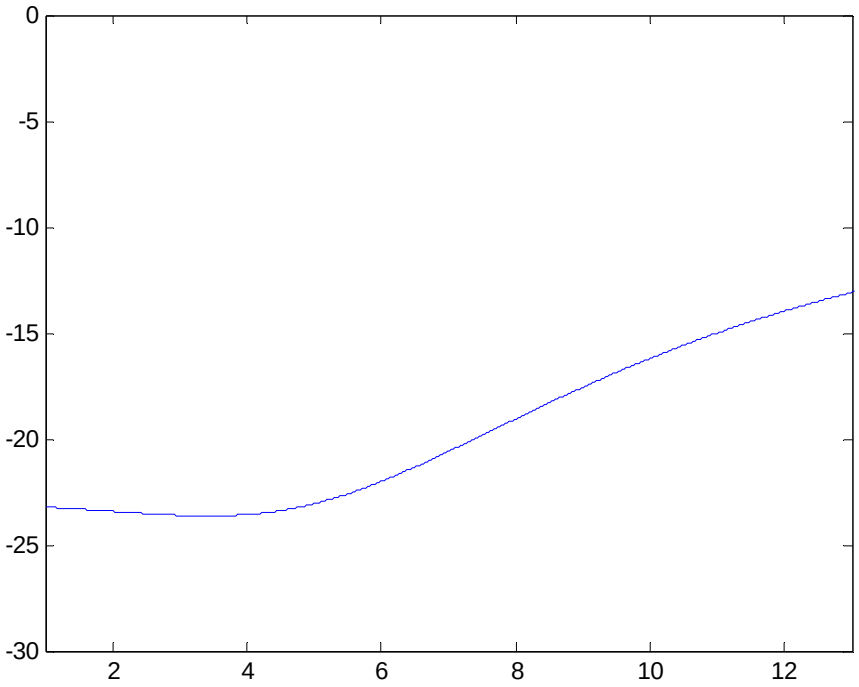

(b)

Figure 6.12: (a) 2×1 configuration of the second center puck with striplines manufactured on Kapton ($\varepsilon_r = 3.5$) and supporting dielectric of polystyrene ($\varepsilon_r = 2.54$); (b) Return loss of it.

One effective way to improve the return loss of the second 2×2 configuration center puck is to cut one pair of coupled striplines to turn it into 2×1 configuration, as shown in Fig.6.12. It is shown that the return loss is improved a lot compared with that of Fig. 6.11 (b). This proves that the degradation of the second 2×2 configuration center puck is mainly due to the mutual coupling between the two pairs of coupled striplines for two polarizations.

One way of improving the return loss is to improve the perpendicular coax-to-microstrip transition [65] [66]. However, the novel approach to the optimization of coax-to-microstrip transition proposed in [65] [66] is mainly for small MMIC external connection, in which application the accuracy about soldering is not a problem. The ELEVEN antenna, on the other hand, is huge compared with its center region, which makes the soldering accuracy at the feeding points unreliable.

6.4 Comparison of Simulation and Measurement of the Return loss of the ELEVEN Antenna Made in 2007

The measurement of the ELEVEN antenna was done at antenna group, Chalmers. In order to compare the return loss of simulation with that of measurement, the center puck (the second 2×2 Configuration) has to be connected to the antenna petals. The center puck is simulated in CST. The antenna petal impedance is simulated in WIPL-D (commercial EM-simulation software based on Method of Moments) by Dr. Jian Yang. For short it is called “three-software-method” in this chapter. All the simulation data files are converted into touchstone format files, and connected in Agilent ADS (a software mainly used for electronic designs), as shown in Fig.6.13.

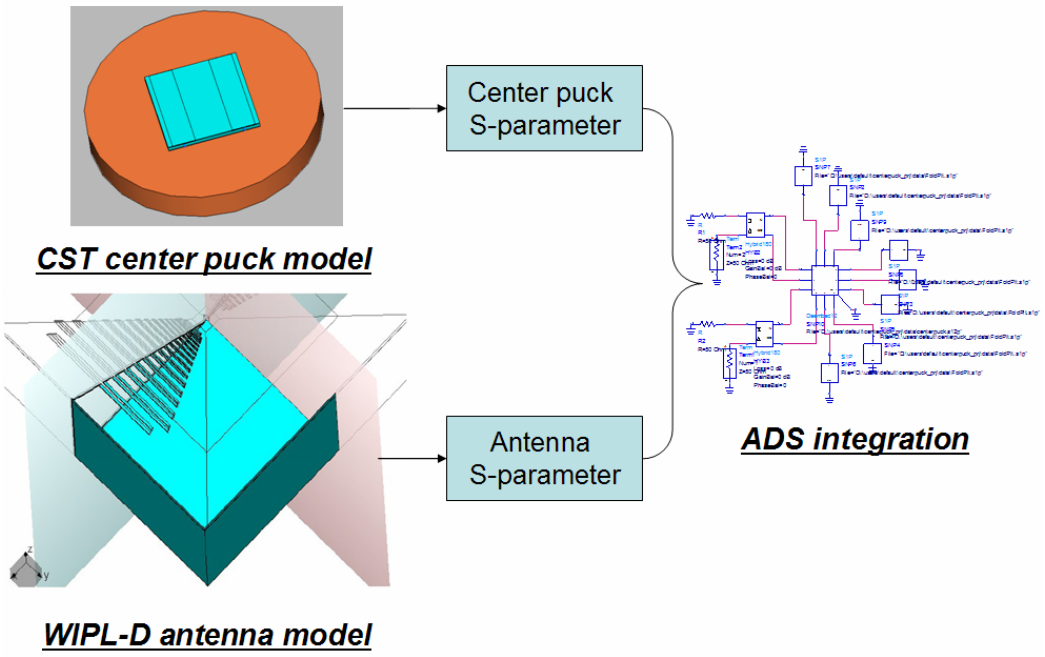

(a)

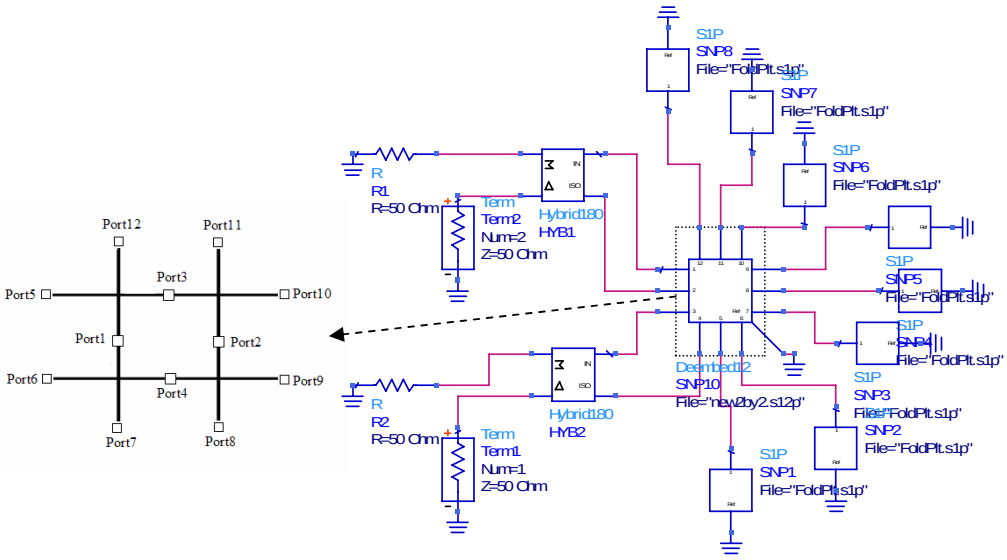

(b)

Figure 6.13: (a) Return loss simulation procedure by combing WIPL-D, CST and ADS; (b) Blocks diagram of the second 2×2 configuration center puck connected with antenna petals in ADS and its schematic illustration of the port numbers of the second center puck.

The second 1-13 GHz 2×2 configuration ELEVEN antenna is almost symmetric for both polarizations. Fig.6.14 shows the real ELEVEN antenna. The return losses of this ELEVEN antenna are almost the same for both polarizations, as can be seen in Fig.6.15.

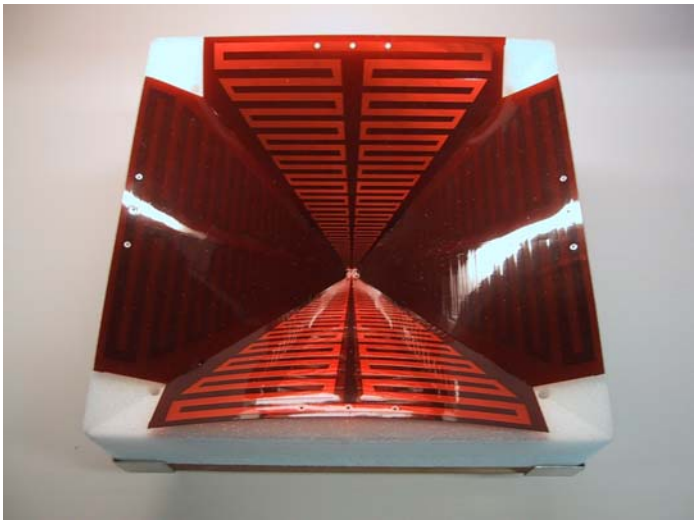

Figure 6.14: Photograph of the second 2×2 configuration ELEVEN antenna.

Figure 6.15 shows the comparison of the return loss of simulation (S11 and S22 for dual polarizations) and that of measurement (S33 and S44 for dual polarization). It is shown that the measurement is slightly better then the simulation, which may be due to the losses in the actual ELEVEN antenna. Although the return loss of this ELEVEN antenna is rather poor as shown in Fig.6.15, it is as we expected agrees with our simulation, which is a good start point for further antenna development. It should be noted that the return loss degradation above 5 GHz is mainly due to the strong coupling between the two pairs of orthogonal striplines in the center puck. And it is the reason why more effort should be paid on the center feeding part of the ELVEN antenna.

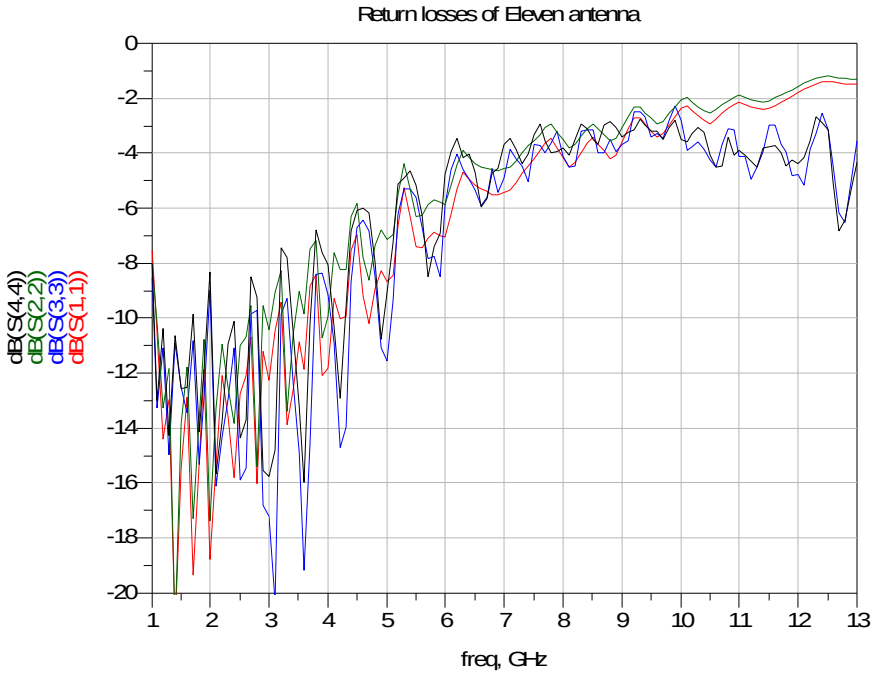

Figure 6.15: Comparison of measured (S33 & S44) and simulated (S11 & S22) return losses for the second 2×2 configuration ELEVEN antenna.

To verify the argument that the return loss degradation is mainly caused by the mutual coupling between the two orthogonal pairs of stripline in the center puck, the lower parallel striplines are taken away (by scraping). And the 2×2 configuration becomes 2×1 configuration. In a similar way, the simulated return loss of this single polarization configuration is obtained by combining WIPL-D, CST and ADS simulations, and is plotted together with the measured one in Fig.6.15. In Fig.6.16, S11 (in red) is the simulated return loss; and S22 (in blue) is the measured return loss. Although the simulation result does not coincide with the measurement perfectly, it indeed shows the trend of the actual return loss variation, which is satisfying. Fig. 17 shows the comparisons of return losses of 2×1 and 2×2 configurations for both simulations and measurements.

The return loss of the 2×1 configuration is below -10 dB from 1 GHz up to 8 GHz, which is a considerable improvement compared with the previous ELEVEN antenna versions. Due to the dielectric effect in the center puck, it degrades above 9 GHz. Nevertheless, the main constraint of the return loss is clear by now, and we are confident that the return losses of the ELEVEN antenna can be improved from 1 GHz to 13 GHz (even up to 18 GHz) by further development.

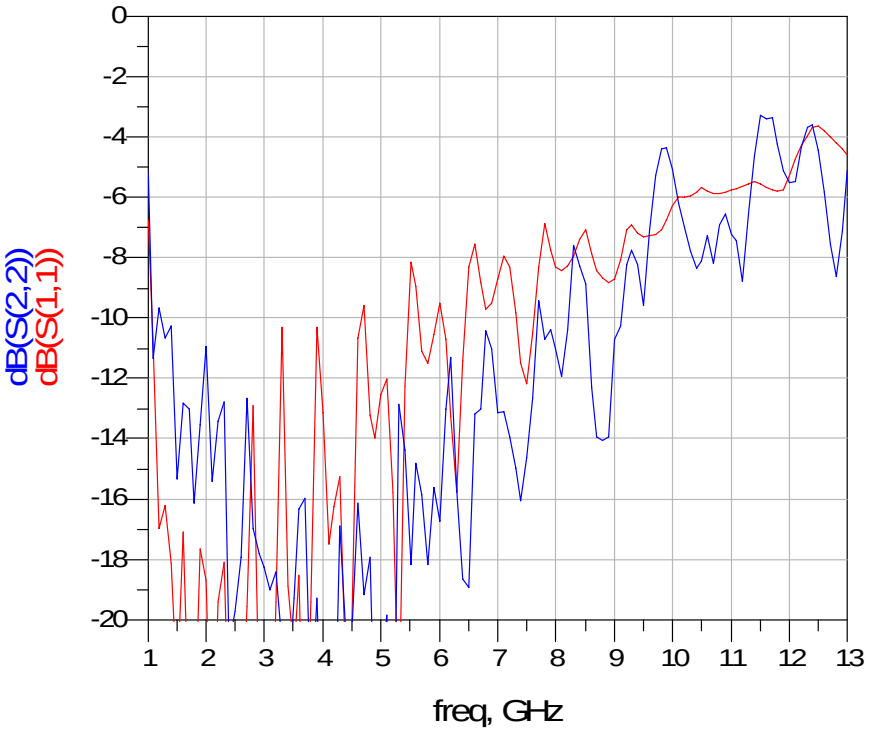

Figure 6.16: Comparison of measured (in blue) and simulated (in red) return losses for the second 2×1 configuration ELEVEN antenna.

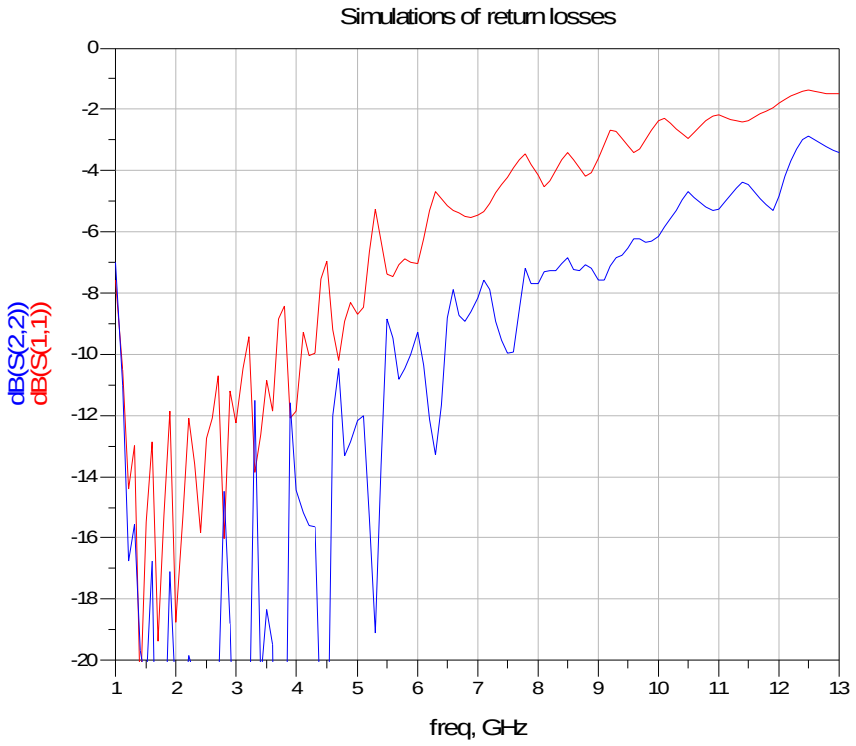

(a)

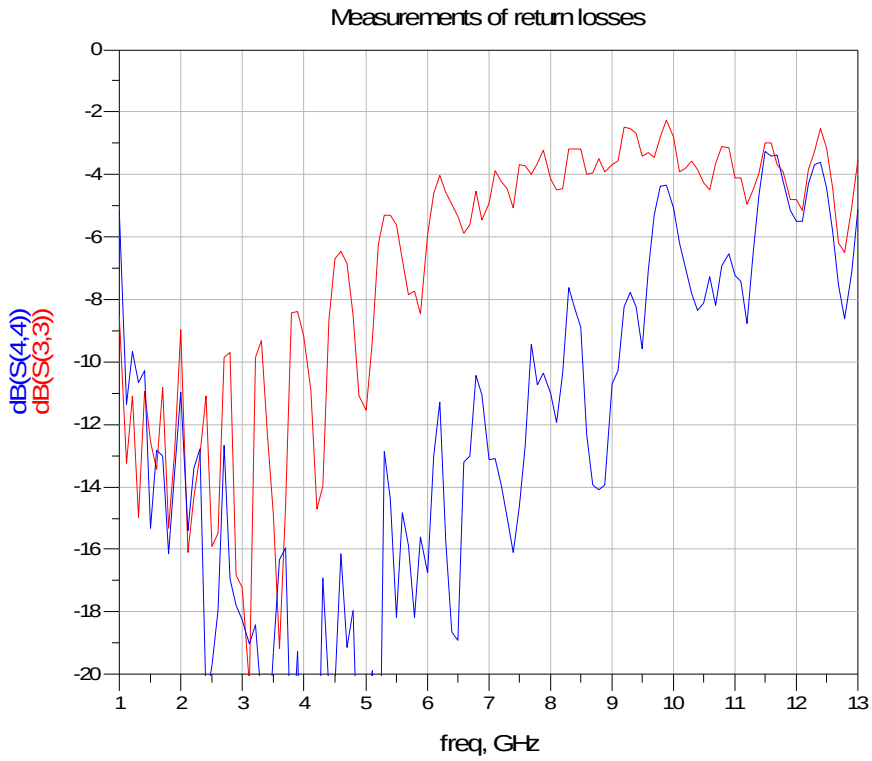

(b)

Figure 6.17: Comparisons of return losses of 2×1 (in blue) and 2×2 (in red) configurations: (a) simulated return losses; (b) measured return losses.

6.5 Measured Gain of the ELEVEN Antenna Made in 2007

The 2×2 configuration ELVEN antenna made in 2007 (as shown in Fig.6.14) suffers from serious cross coupling between two polarizations (mainly due to the strong coupling at the center puck), which degrades its return loss performance. By removing one pairs of striplines at the center puck, the ELVEN antenna becomes 2×1 configuration. Due to the poor performance of the 2×2 configuration, only the radiation characteristics of the 2×1 configuration ELEVEN antenna is presented here. Note that the antenna petals for the other polarization is kept, which may cause cross-polarization due to the even mode radiation of the operating polarization, which will be addressed later on in this section.

The radiation patterns and antenna gain are measured. And the radiation gain is shown in Fig.6.18, from which it is seen that the antenna gain is not desirable either. Ideally, the gain of the ELEVEN antenna should be around 11 dBi, and that the gain variation should not be so much.

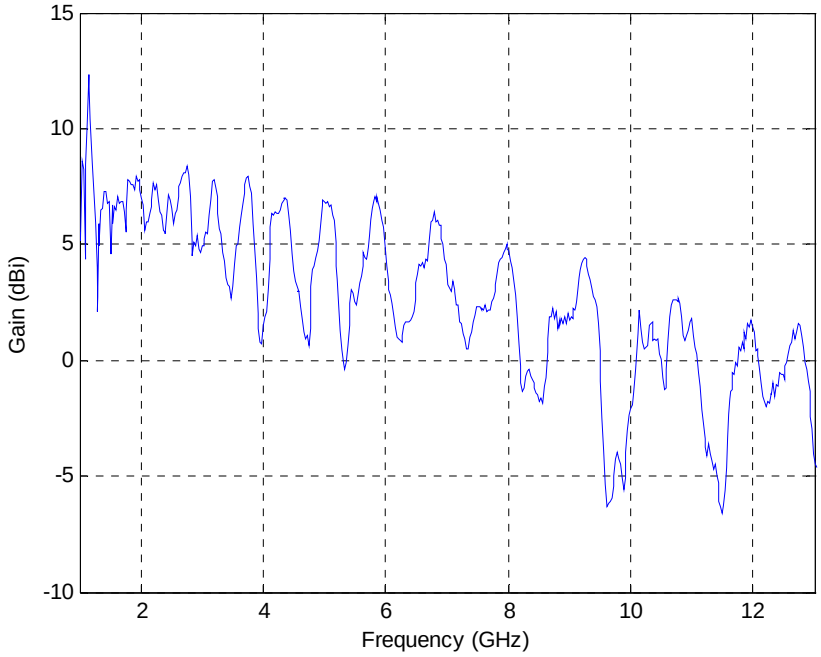

Figure 6.18: Measured gain of 2×1 configuration ELEVEN antenna.

From Fig.6.18, the gain drop at high frequencies; it is due to the RL degradation. At low frequencies, the maximum gain points are still below standard 11 dBi. This is probably because of the insertion loss introduced by the hybrid and cables connecting the hybrid and ELEVEN antenna. Fig.6.19 shows the measured S-parameters of the UWB hybrid used in ELEVEN antenna. Δ port, or differential port, of the hybrid is denoted as port 1; Σ port, or sum port, port 4. That is, in ideal case, when Σ port is terminated with 50 Ohms load, the power delivered to port 1 will be divided equally

in amplitude, but 180° out of phase, to port 2 and 3. (That's how the ELEVEN antenna is differentially excited.) Note that in order to measure the four ports of the hybrid simultaneously, a 4-port network analyzer, for which the highest measurable frequency is 8 GHz, is used.

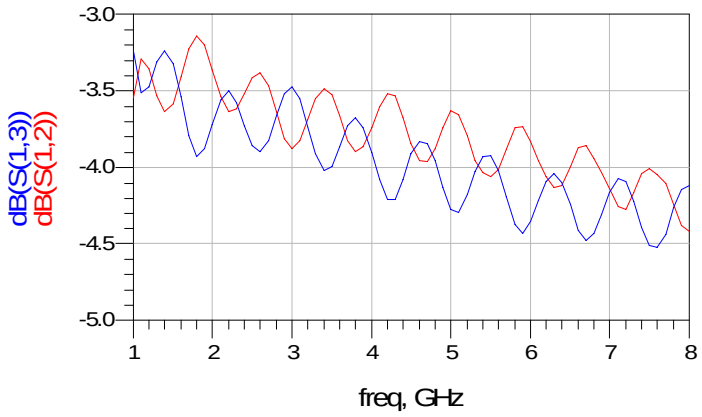

(a)

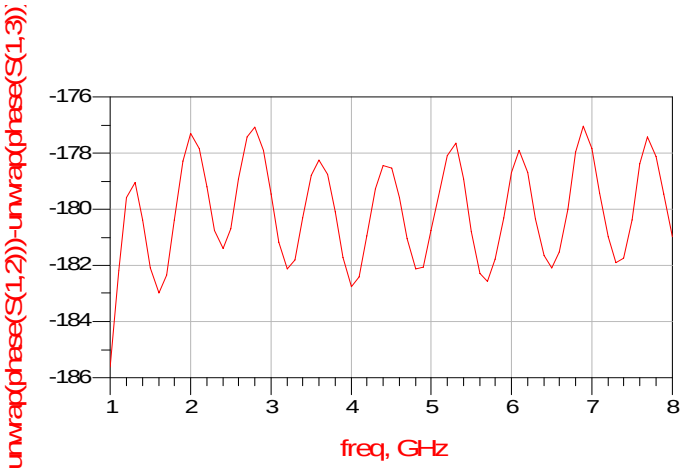

(b)

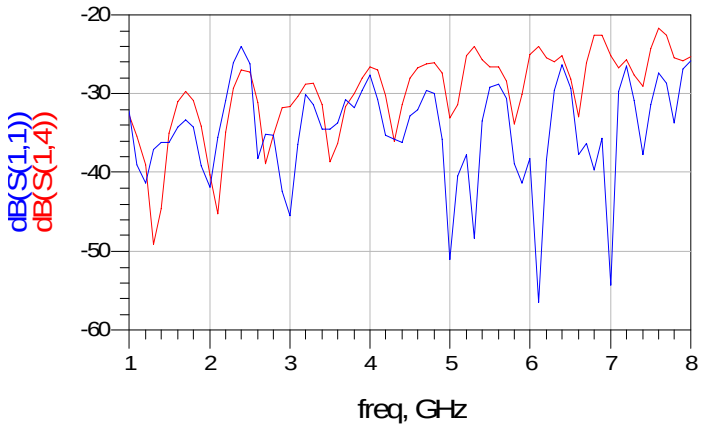

(c)

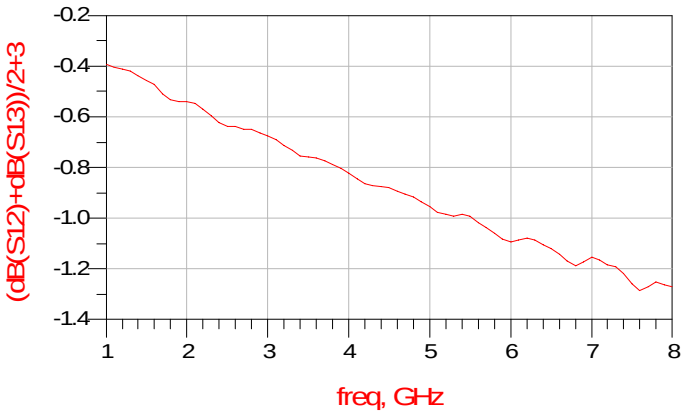

(d)

Figure 6.19: (a) Power split at port 2 and 3; (b) Phase difference at port 2 and 3; (c) return losses at port 1 and 4; (d) Average insertion loss.

From Fig.6.19 (a), it is seen that the amplitude unbalance is within 0.8 dB. Fig.6.19 (b) shows the phase unbalance is within $3°$. The return losses at Δ and Σ port are below -20 dB (see Fig.6.19 (c)). The average insertion loss of the hybrid is shown in Fig6.19 (d).

147 mm long cables (with 1.2 mm outer diameter, 0.3 mm inner diameter and 0.18 mm outer conductor thickness) are used in the ELEVEN antenna to facilitate measurement. At one end (defined as port 1) of the cable, the inner conductor is coming out, which is soldered to the center puck. The other end of the cable (defined as port 2) is soldered with a SMA connector. In order to measure the cable, we manually soldered port 1 with another SMA connector, and measure it with network analyzer.

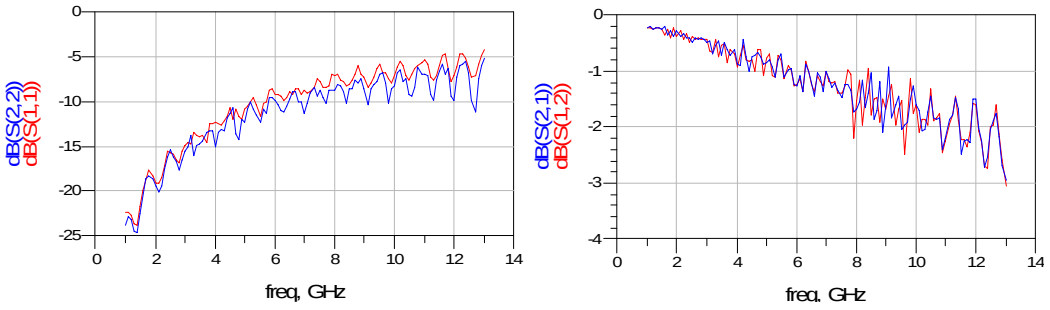

(a) (b)

Figure 6.20: Measured S-parameters of the cable: (a) return loss; (b) insertion loss.

Fig.6.20 shows the cable has poor performance, which may adversely affect the ELEVEN antenna characteristics. However, one thing should bear in mind is that one end (port 1) of the measured cable is poorly manually soldered. And poor soldering will introduce parasitic inductance and/or capacitance, which of course become

significant with increasing frequency. Therefore, the actual cable performance is probably not as bad as shown in Fig.6.20. Since the cable ended with SMA connector at two ends is not available, it is impossible to see the actual performance of the cables used in ELEVEN antenna. If we assume the actual insertion loss of the cable is as shown in Fig.6.20 (b), the total insertion loss before the ELEVEN antenna will be it together with that of the cable. After calibrate out the insertion loss before ELEVEN antenna, its gain is shown in Fig.6.21.

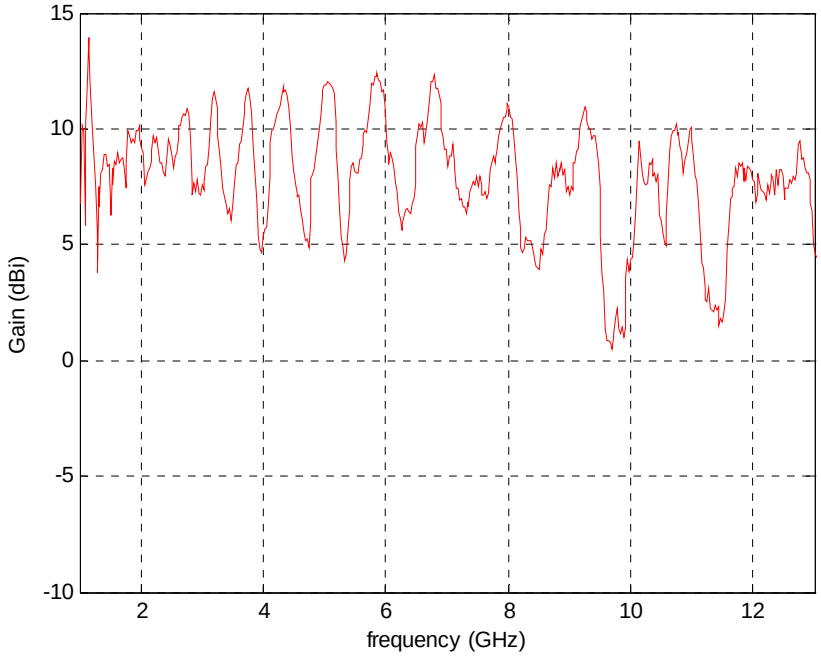

Figure 6.21: Calibrated 2×1 configuration ELEVEN antenna gain.

As we said before, due to the uncertainty of the actual cable, the gain is not valid at high frequencies. But at low frequencies, Fig.6.21 should be close to the actual gain of ELEVEN antenna. As can be seen from Fig.6.21, the maxima are close to 11 dBi, however, the gain variation is too large to be accepted. And unfortunately, there is no proper answer for the large gain variation yet. It is believed to be a complicated combination of many factors so far.

6.6 Imperfect Effects Hybrid and Cable

From Fig.6.19, it is seen that the commercial UWB hybrid used in ELEVEN antenna is not perfect. Its unbalance (both amplitude and phase) effects will be studied in this section. From Fig.6.20, the measured cable show rather poor performance. Effects of the cable will also be discussed in this section.

6.6.1 Unbalance Effects of the Hybrid

Fig.6.22 shows the unbalance effect of the hybrid on return loss. Return losses were measured with and without hybrid. To fairly compare the return loss with and without hybrid's (amplitude and phase) unbalance, the insertion loss of the hybrid is calibrated out. In Fig.6.22, lossless hybrid means the actual hybrid with insertion loss calibrated out. Fig.6.22 (a) is the return losses comparison of 2×2 configuration ELEVEN antenna; while Fig.6.22 (b) is that of 2×1 configuration ELEVEN antenna. It is concluded that the unbalance effect of the hybrid is almost negligible in terms of return loss.

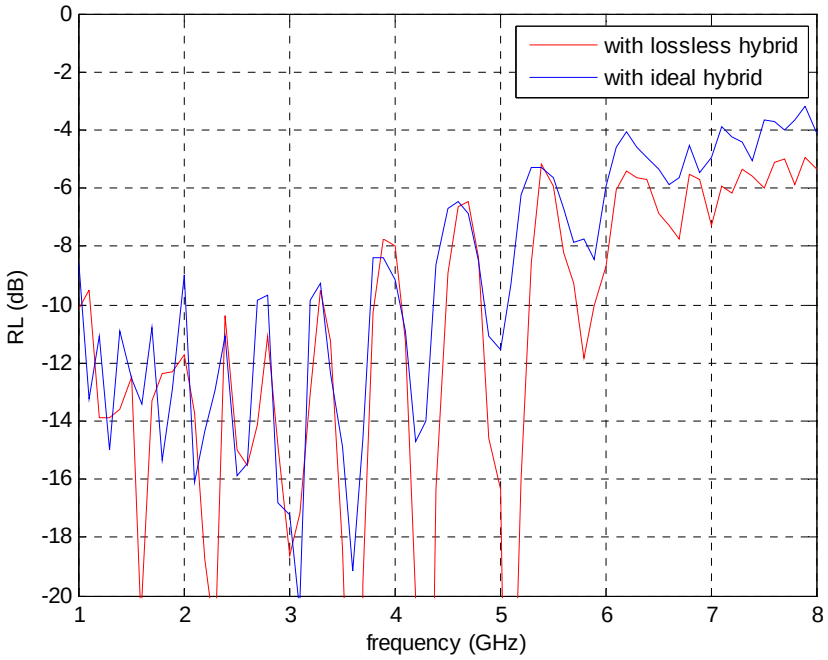

(a)

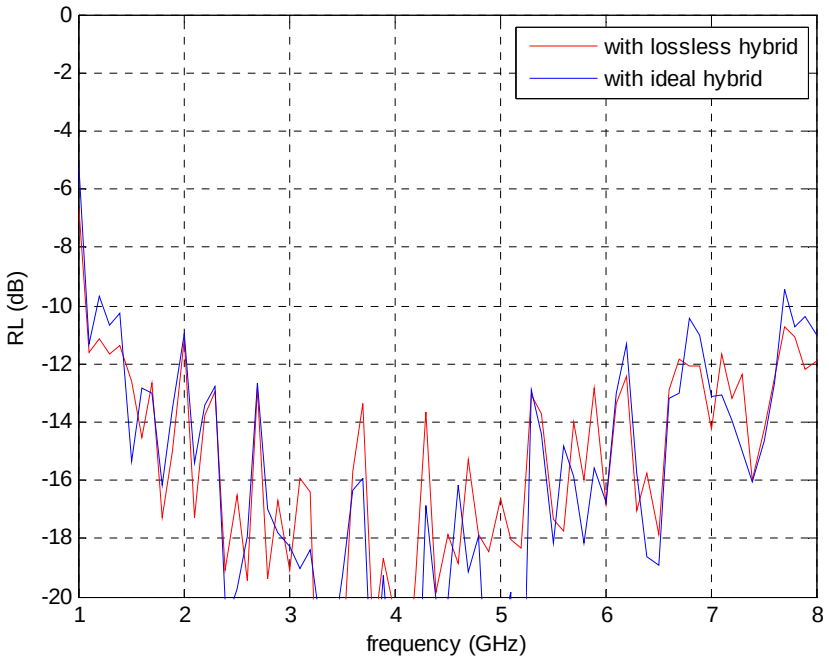

(b)

Figure 6.22: Comparison of return losses with and without hybrid unbalance: (a) 2×2 configuration; (b) 2×1 configuration.

To simplify the verification of the unbalance effect on the radiation pattern, a pair of parallel dipoles ($\lambda/2$ separated and $\lambda/10$ above infinite ground) is constructed and simulated in CST, as shown in Fig.6.23 (a).

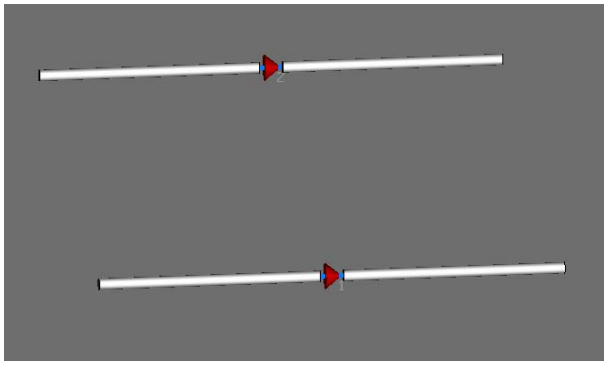

(a)

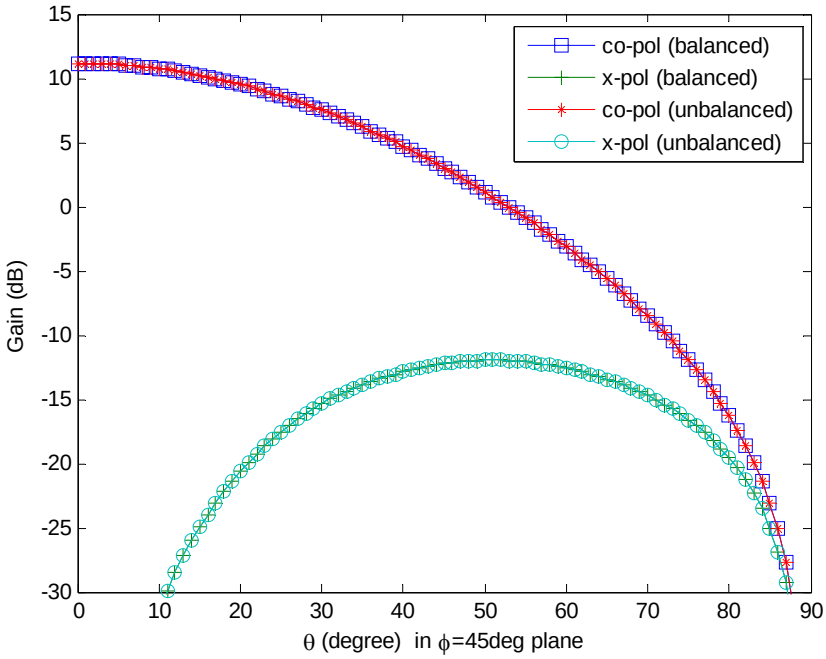

(b)

Figure 6.23: (a) A pair of parallel dipoles above infinite ground; (b) simulated co-polar and cross-polar patterns.

From Fig.6.19, it is seen that the maximum amplitude unbalance is 0.8 dB, and maximum phase unbalance is 3°. In the CST simulation, first, the parallel dipoles are excited with equal phase and 0° phase shift (balanced excitation); then, they are excited with 1.1 amplitude ratio, and 3° phase shift (unbalanced excitation). Fig.6.23 (b) shows the co-polar and cross-polar patterns for these two excitations, from which it is seen that the unbalance effect introduced by the actual hybrid is negligible in terms of radiation patterns of parallel dipoles.

6.6.2 Effects of the Coaxial Cables

As mentioned before, the poor performance of the measured cable is probably due to poor manual soldering at one end. To verify this, the measured cable is included in the "three-software-method" (see Fig.6.13), as shown in Fig.6.24 (a). Note that duo to similarity of the two polarizations measured cable dada is only used for one polarization. First, the poor soldering end of the cable is connected to the hybrid (assuming that the two cables are identical), and the return loss is shown in Fig.6.24 (b). The, the cables are reversed, that is, poor soldering end is connected to center puck, and the return loss in this case is shown in Fig.6.24 (c). As it is known that the reflection from the center puck is strong, if the poor soldering is connected to the hybrid, then the there is multi-reflection between them; that is the reason of the large

RL variations in Fig.6.24 (b). If the poor soldering is connected to the center puck, all the reflection from the hybrid is small enough that there is no significant multi-reflection between hybrid and center puck. Therefore, the measured cable data is not valid due to the poor soldering at one end of it.

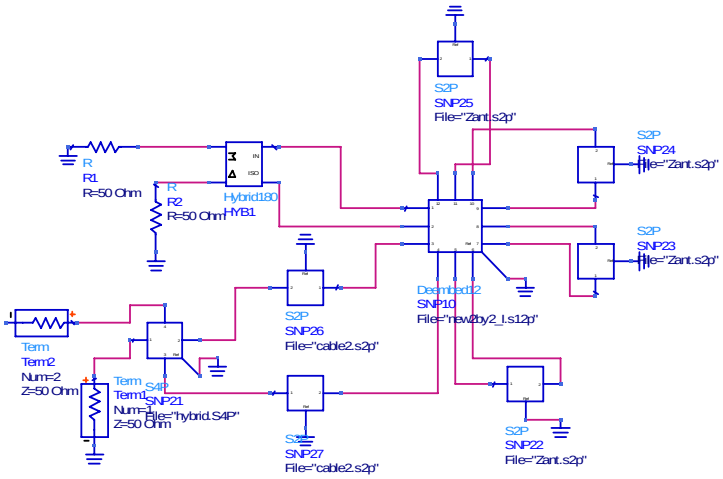

(a)

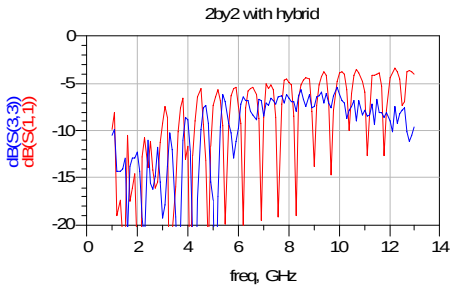

(b)

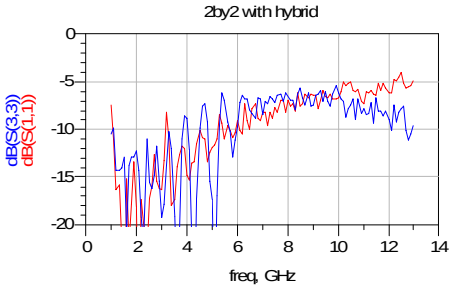

(c)

Figure 6.24: “three-software-method” with measure cable: (a) ADS model; (b) RL when poor soldering end of the cable is connected to hybrid; (c) RL when poor soldering end of the cable is connected to center puck. (S11: simulated RL; S33: measured RL.)

Since it is impossible to measure the actual performance of the cables used in the ELEVEN antenna, the coaxial cable model (with the same dimensions and insertion loss) in ADS is used, which is shown in Fig.6.25 (a). The RL comparison between simulation (S11) and measurement (S33) is shown in Fig.6.25 (b), from which it is seen that the simulation and measurement agreement is still good.

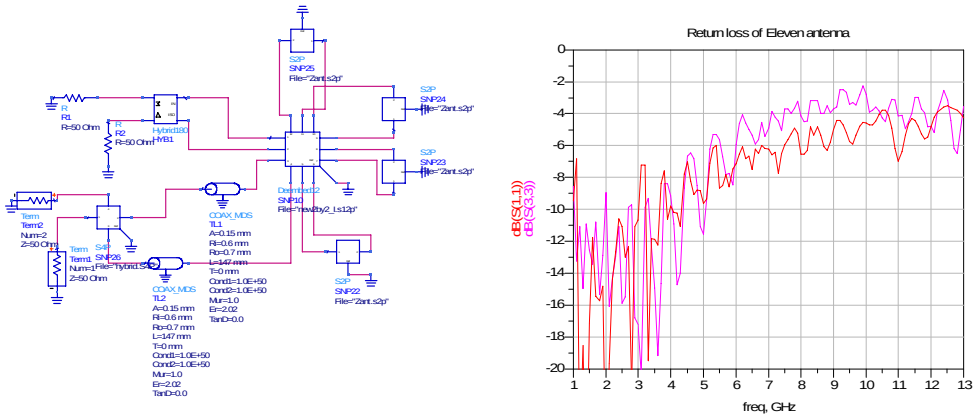

(a) (b)

Figure 6.25: (a) ADS model with cable model; (b) RL comparison of it (S11) with measurement (S33).

6.7 Efficiencies Measurement of 2×1 Configuration ELEVEN Antenna in Reverberation Chamber

The reverberation chamber ([43]-[46]) is not only an effective tool to measure mobile phone antenna, it can also be used to measure different efficiency of conventional antenna conveniently. The efficiencies of the 2×1 configuration ELEVEN antenna was measured in the reverberation chamber. Fig.6.26 shows the measured efficiencies (except the insertion loss efficiency) of it. Note that the ohmic loss efficiency is impossible to measure; here instead insertion loss efficiency is introduced taking into account the insertion loss of the hybrid and cable. Also note that the insertion loss of the cable is according to its datasheet, and that in reality it may be worse.

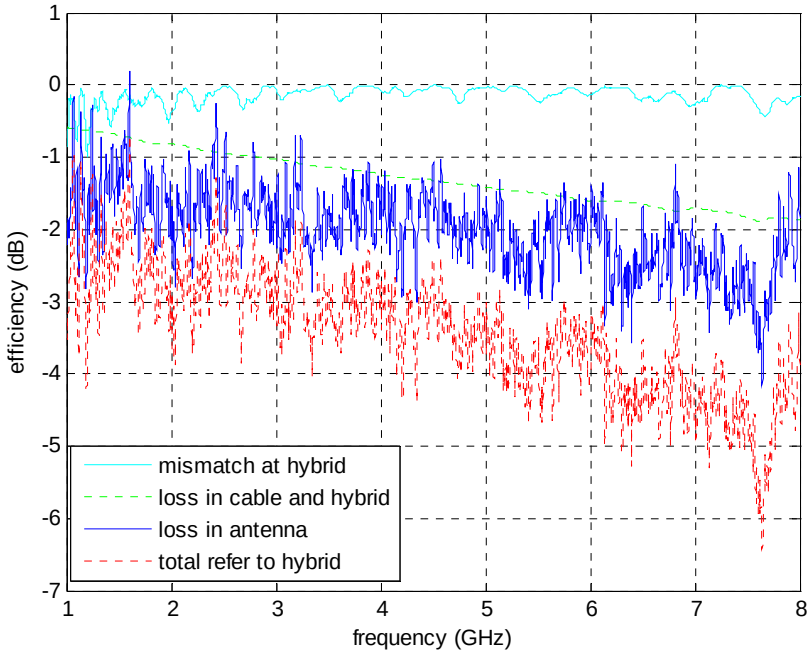

(a)

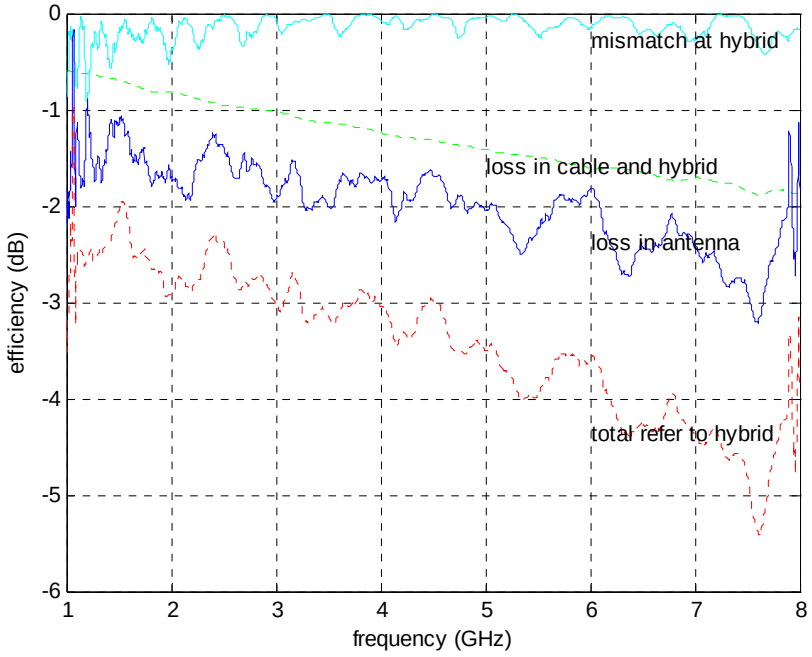

(b)

Figure 6.26: Different efficiencies of the 2×1 configuration ELEVEN antenna: (a) 10 MHz frequency stirring; (b) 100 MHz frequency stirring.

7. Future Work

Despite the current problems and difficulties of development, ELEVEN antenna is an excellent solution for UWB radio telescope applications. It has been shown in [2]-[7] that this novel UWB antenna, used as a feed for reflector antenna, can provide good radiation pattern, high radiation efficiency and reasonable input return loss over a decade frequency band.

The fundamental goal of integrating the ELEVEN antenna with UWB LNA is to reduce the overall system noise temperature, and to increase the figure of merit, G/T. To achieve this goal, the most important things are to reduce the return loss of the ELEVN antenna, and to match it to the LNA in a better approach. The concept of different antenna feeding part configurations has been introduced. The future work is to make a profound study of these configurations, and other possible ones, with the ultimate goal of reducing the return loss of the ELVEN antenna while keeping the other good antenna characteristics. And the different possibilities of measuring the system characteristics of the ELEVEN antenna with LNA will be studied. For now, it is believed that the reverberation chamber mentioned in [43]-[46] will be the most promising tool to do that measurement.

Reference

[1] G. Cortes, “Low frequency end performance of a symmetrical configuration antenna for the square kilometer array (SKA),” *Experimental Astronomy*, pp. 111-118, 2004.

[2] R. Olsson, P.-S. Kildal and S. Weinreb, “ The Eleven antenna: a compact low-profile decade bandwidth dual polarized feed for reflector antennas,” *IEEE Trans. Antennas Propag.*, vol. 54, No. 2, Feb. 2006

[3] R. Olsson, P.-S. Kildal and M. Shields, “ Measurements of a 150 to 1700 MHz low loss Eleven feed for the 42 m radio telescope at Green Bank,” *IEEE Antennas and Propagation Society International Symposium 2006*, 9-14, pp. 347 – 350, July 2006.

[4] R. Olsson, P.-S. Kildal and S. Weinreb, “Measurements of a 1 to 13 GHz model of a dual polarized low-profile log-periodic feed for US-SKA,” *IEEE Antennas and Propagation Society International Symposium 2005*, Volume 2B, 3-8, pp. 700 – 703, July 2005.

[5] R. Olsson, P.-S. Kildal and S. Weinreb, “A novel low-profile log-periodic ultra wideband feed for the dual-reflector antenna of US-SKA,” *IEEE Antennas and Propagation Society International Symposium 2004.* Volume 3, pp. 3035 – 3038, June 2004.

[6] P.-S. Kildal, R. Olsson and J. Yang, “Development of Three Models of the Eleven Antennas: A new Decade bandwidth High Performance Feed for Reflectors”, EuCap 2006, 6-10 November 2006.

[7] Rikard Olsson, “Development of the Eleven antenna – a decade bandwidth feed for reflector antenna,” Thesis for the degree of Licentiate of Engineering, October 2005.

[8] Aly Ismail and Asad A. Abidi, “A 3-10 GHz low noise amplifier with wideband LC-ladder matching network,” *IEEE Journal of solid-state circuits, vol.39, pp. 2269-2277, Dec. 2004*.

[9] A. Bevilacqua and Ali M. Niknejad, “An ultra-wideband CMOS low-noise amplifier for 3.1-10.6 GHz wireless receivers,” *IEEE Journal of solid-state circuits, vol. 39, pp. 2259-2268, Dec. 2004*.

[10] V. Rambeau, H. Brekelmans, M. Notten, K. Boyle and J. V. Sinderen, “ Antenna and input stages of a 470-710 MHz silicon TV tuner for portable applications,” *Proceedings of ESSCIRC*, pp. 239-242, 2005.

[11] S. W. Chung, S. Y. lee and K. H. Park, “Wideband impedance matching of integrated antennas and CMOS low noise amplifier for a multi-band UWB receiver,” *Proceedings of IEEE*, pp. 131-134, 2004.

[12] C. Y. Hang, Y. X. Qian and T. Itoh, “High-efficiency push-pull power amplifier integrated with quasi-yagi antenna,” *IEEE Transaction on microwave theory and techniques, vol. 49*, pp. 1155-1161, June 2001.

[13] F. S. Lee and A. P. Chandrakasan, “A BiCMOS ultra-wideband 3.1-10.6 GHz front-end,” *IEEE Journal of solid-state circuits, vol. 41*, pp. 1784-1791, 2006.

[14] Bevilacqua and A. M. Niknejad, “An ultrawideband CMOS Low-noise amplifier for 3.1-10.6 GHz wireless receivers,” *IEEE Journal of solid-state circuits, vol. 39*, pp. 2259-2268, 2004.

[15] J. Lerdworatawee and W. Namgoong, “Low-noise amplifier design for ultrawideband radio,” *IEEE Transaction on microwave theory and techniques, vol. 51*, pp. 1075-1087, 2004.

[16] John D. Kraus, “Radio astronomy,” *New York cop.* 1966.

[17] Jan Askne, “Remote Sensing Using Microwaves,” Chapter C. Passive technique-Microwave radiometry, *Chalmers University of Technology*.

[18] A. Stogryn, “A note on brightness temperature at millimeter wavelengths,” *IEEE Transactions on Geoscience Electronics*. Vol. GE-13, pp. 81-84. Apr. 1975.

[19] Yong Han and Ed R. Westwater, “Analysis and Improvement of Tipping Calibration for Ground-based Microwave Radiometers,” *IEEE transaction on Geoscience and Remote Sensing*. Vol. 38, No.3, May 2000.

[20] German Cortes Medellin, “Antenna Noise Temperature Calculation,” *US-SKA Technical Memo Series*, Memo 95.

[21] David M. Pozar, “Microwave Engineering, Second Edition,” *JOHN WILEY & SONS, INC.*, pp. 686-689.

[22] Asoka Dissanayake, Jeremy Allnutt and Fain Haidara, “A Prediction Model that Combines Rain Attenuation and Other Propagation Impairment Along Earth-Satellite Paths,” *IEEE TRANSACTION ON ANTENNA AND PROPAGATION*, VOL. 45, NO. 10, OCTOBER, 1997.

[23] MERRILL I. SKOLNIK, “Introduction to Radar Systems, McGRAW-HILL KOGAKUSHA,” *LTD*, pp. 366-370.

[24] Robert E. Collin, “Foundations for Microwave Engineering, Second Edition,” *JOHN WILEY & SONS, INC.*, pp. 49-53.

[25] Per-Simon Kildal, “Foundations of Antennas: A Unified Approach,” Studentlitteratur, Lund, 2000.

[26] L. C. Godara, “Handbook of Antennas in Wireless Communications,” *CRC Press*, 2002.

[27] C. C. Chiau, “Study of the Diversity Antenna Array for the MIMO Wireless Communication Systems,” *PhD thesis at Queen Mary, university of London*, April, 2006.

[28] R. S. Calvo, “Study of losses due to head and hand of mobile phones with external and built-in antennas in reverberation chamber,” *Master thesis at antenna group, Chalmers*, 2001.

[29] Om P. Gandhi, G. Lazzi and C. M. Furse, “Electromagnetic absorption in the human head and neck for mobile telephones at 835 and 1900 MHz,” *IEEE Trans. On microwave theory and tech.*, vol. 44, pp. 1884-1896, Oct. 1996.

[30] G. F. Pedersen, M. Tartiere and M. B. Knudsen, “Radiation efficiency of handheld phones,” *Proceedings of. IEEE Vehicular Technology Conference*, 2000.

[31] T. Zervos, A. A. Alexandridis, V. V. Pertrovic etc., “ Mobile phone antenna performance and power absorption in terms of hand size and distance from user’s head,” *Wireless personal communications*, pp. 109-120, Springer 2005.

[32] O. Kivekäs, J. Ollikainen, T. Lehtiniemi and P. Vainikainen, “Bandwidth, SAR, and effieciency of internal mobible phone antennas,” *IEEE Trans. on electromagnetic compatibility*, vol. 46, pp. 71-86, Feb. 2004.

[33] D. M. Pozar, “Microwave and RF Design of Wireless Systems,” *John Wiley & Sons, Inc*., 2001.

[34] R. Magoon, A. Molnar, J. Zachan, G. Hatcher and W. Rhee, “A single-chip quad-band (850/900/1800/1900 MHz) direct conversion GSM/GPRS RF transceiver with integrated VCOs and fractional-N synthesizer,” *IEEE Journal of solid-state circuits*, vol. 37, pp. 1710-1719, Dec. 2002.

[35] J. A. P. Azervedo and T. C. Pimenta, “Design of a low noise amplifier for CDMA transceivers at 900 MHz in CMOS 0.35μm,” *Proceedings of IEEE on integrated circuits and system design*, 2003.

[36] -----, “Triple/dual/single mode CDMA LNA/mixers receiver system requirements,” *MAMIM, Application note* 289, Sep. 2000.

[37] Z. Wang, D. Coveyou and R. Kincaid, "Designing low cost CDMA front-end receivers," *RF Micro Devices Inc.*

[38] Y. Li and D. Maksimovic, "High Efficiency Wide Bandwidth Power Supplies for GSM and EDGE RF Power Amplifiers," *Proceedings of IEEE*, 2005.

[39] D. Gesbert, M. shafi, D. Shiu, P. J. Smith and A. Naguib, "From Theory to Practice: An Overview of MIMO Space-time Coded Wireless Systems," *IEEE Journal on selected areas in Communications*, vol. 21, pp. 281-302, April 2003.

[40] D. M. Pozar, "Microwave and RF Design of Wireless Systems," *John Wiley & Sons, Inc.*, 2001, pp. 144-147.

[41] L. C. Godara, "Handbook of Antennas in Wireless Communications," *CRC Press*, 2002.

[42] John G. Proakis, "Digital Communications," *McGraw Hill*, 2000.

[43] P. S. Kildal and K. Rosengren, "Electromagnetic Analysis of effective and Apparent Diversity Gain of two Parallel Dipoles," *IEEE Antennas and Wireless Propagation Letters*, vol. 2, pp. 9-13, 2003.

[44] K. Rosengren and P. S. Kildal, " Radiation efficiency, correlation, diversity gain and capacity of a six-monopole antenna array for a MIMO system: theory, simulation and measurement in reverberation chamber," *IEE Proc. Microw. Antennas Progag.* Vol. 152, pp. 7-16, 2005.

[45] K. Rosengren, J. Carlsson and P. S. Kildal, "Maximizing the Effective Diversity Gain of Two Parallel Dipoles by Optimizing the Source Impedances," *Microwave & optical tech. letters*, vol. 48, pp. 532-535, March 2006.

[46] K. Rosengren and P. S. Kildal, "Diversity Performance of a Small Terminal Antenna for UMTS," *Nordic Antenna Symposium, Kalmar,* 2003.

[47] S. Dossche, J. Romeu and S. Blanch, "Matching network for a spatial diversity antenna system," *Proceeding of IEEE*, pp. 427-431, 2004.

[48] E. Biglieri, R. Calderbank, A. Constantinides A. Goldsmith, A. Paulraj and H. V. Poor, "MIMO wireless communications," Cambridge university press, 2007.

[49] M. Pauli, C. Waldschmidt, W. Sörgel and W. Wiesbeck, "Measurement results of compact MIMO terminal antennas," *unpublished paper*.

[50] C. Waldschmidt, T. Fugen and W. Wiesbeck, "Spiral and dipole antennas for indoor MIMO-systems," *IEEE antennas and wireless propagation letter*, vol.1, pp.176-178, 2002.

[51] C. Waldschmidt, S. Schulteis and W. Wiesbeck, "Complete RF system model for analysis of compact MIMO arrays," *IEEE transactions on vehicular technology*, vol. 53, pp.579-586, May 2004.

[52] J.-P. Kermoal, "Measurement, modeling and performance evaluation of MIMO radio channel," *PhD thesis* at Aalborg University, Denmark.

[53] Z. Zhang, P. K. Sorensen, Z. Yun, M. F. Iskander and J. F. Harvery, "A ray tracing approach for indoor/outdoor propagation through window structures," *IEEE Trans. antennas propagation*, vol. 50, pp. 742-748, May 2002.

[54] R. Bancroft, "Fundamental dimension limits of antennas," *unpublished paper, Westminster, Colorado*.

[55] H. Morishita, Y. Kim, Y. Koyanagi and K. Fujimoto, "A folded loop antenna system for handsets," *IEEE proceeding*, pp. 440-443, 2001.

[56] C. G. Buxton, W. L. Stutzman, R. R. Nealy and A. M. Orndorff, "The folded dipole: a self-balancing antenna," Microwave and optical technology letter, vol. 29, pp. 155-160, May 2001.

[57] S. Hayashida, H. Morishita and K. Fujimoto, “Self-balanced wideband folded loop antenna,” *IEE Proc. Microw. Antennas Propag*. vol. 153, pp. 7-12, Feb. 2006.

[58] H. Morishita, H. Furuuchi and K. Fujimoto, “Characteristics of a balanced-fed loop antenna system for handsets in the vicinity of human head or hand,” *IEEE Proc*., vol. 4, pp. 2254-2257, Jul. 2000.

[59] Jani Ollikainen, Outi Kivekäs, Anssi Toropainen, and Pertti Vainikainen, “Internal dual-band patch antenna for mobile phones,” *ESA* 2000.

[60] Jani Ollikainen and Pertti Vainikainen, “Radiation and bandwidth characteristics of two planar mutistrip antennas for mobile communication systems,” *Proceeding of IEEE vehicular technology conference*, pp. 1186-1190, 1998.

[61] R. Garg and I. J. Bahl, “Characteristics of Coupled Microstriplines,” *IEEE transaction on microwave theory and techniques*, vol. MTT-27, No. 7, pp. 700-705, July 1979.

[62] J. S. Wight, O. P. Jain, W. J. Chudobiak and V. Makios, “Equivalent circuits of microstrip impedance discontinuities and launchers,” *IEEE Transaction on microwave theory and techniques*, pp. 48-52, Jan. 1974.

[63] M. Hashemi-Nasab and A. Cheldavi, “Coupling model for the two orthogonal microstrip lines in two layer PCB board,” *Progress in electromagnetics, PIER 60*, pp. 153-163, 2006.

[64] A. Cheldavi and A. Arshadi, “A simple model for the orthogonal coupled strip lines in multilayer PCB: (quasi-TEM approach),” *PIER 60*, pp. 153-163, 2006.

[65] M.Morgan and S. Weinreb, “A millimeter-wave perpendicular coax-to-microstrip transition,” IEEE MTT-S Digest 2, pp. 817-820, 2002.

[66] J. E. Roh, J. W. Li, B. C. Ahn, C. S. Park and E. J. Cha, “Novel approach to optimizing a broadband right-angle coaxial-to-microstrip transition,” Microwave and optical technology letters, vol. 49, pp. 451-456, Feb. 2007.